UNIVERSITY OF SOUTHAMPTON

Multiple Model Control of Functional Electrical Stimulation Electrode Arrays

by

Junlin Zhou

Supervisor: Prof. Christopher Freeman, Prof. William Holderbaum, Dr Ann-Marie Hughes

ORCiD: https://orcid.org/0009-0003-9888-9759

A thesis submitted for the degree of Doctor of Philosophy

in the
Faculty of Engineering and Physical Science
School of Electronics and Computer Science

August 2025

University of Southampton

Abstract

Faculty of Engineering and Physical Science
School of Electronics and Computer Science

Doctor of Philosophy

Multiple Model Control of Functional Electrical Stimulation Electrode Arrays

by Junlin Zhou

Functional electrical stimulation (FES) is an upper limb stroke rehabilitation technology that can enable patients to recover their lost movement by assisting intensive and goal-oriented task training. Unfortunately, existing commercial FES devices using single-pad electrode cannot provide selective muscle activation, hence their tracking accuracy is limited. Electrode arrays combining multiple pads in a single structure have recently been developed, and can more accurately assist wrist and finger movements. However, the set-up procedures currently used to locate the best stimulation sites are very time-consuming, and not suitable for a home use scenario. Their accuracy is also limited as they are predominantly open-loop. To date, Iterative Learning Control (ILC) has achieved the best performance for FES array tracking control tasks. Unfortunately it requires a large number of model identification tests that slow down the training, and must be repeated for different desired trajectories. All these drawbacks lead to prohibitive inconvenience for users and prevent translation to clinical or home environments.

To address this, an estimation-based multiple model switched iterative learning control (EMMILC) framework is proposed. This combines the most successful adaptive and learning properties of existing FES controllers employed for single pad systems. A novel multiple-model design procedure guaranteeing robust performance is developed, and initial experimental results using single-pad electrode results are then presented to confirm efficacy of the approach. Experimental results show that EMMILC can reduce tracking error to 20% of its initial value within five trials, and maintain the same level of error in the presence of pronounced muscle fatigue. This architecture outperforms the standard ILC approach, and confirms the fundamental proof of concept. The EMMILC approach is then extended for application to electrode array technology, and simulations using a realistic model confirm significant improvement compared with existing controllers.

Contents

List of Figures

List of Tables

Declaration of Authorship

I declare that this thesis and the work presented in it is my own and has been generated by me as the result of my own original research.

I confirm that:

1. This work was done wholly or mainly while in candidature for a research degree at this University;
2. Where any part of this thesis has previously been submitted for a degree or any other qualification at this University or any other institution, this has been clearly stated;
3. Where I have consulted the published work of others, this is always clearly attributed;
4. Where I have quoted from the work of others, the source is always given. With the exception of such quotations, this thesis is entirely my own work;
5. I have acknowledged all main sources of help;
6. Where the thesis is based on work done by myself jointly with others, I have made clear exactly what was done by others and what I have contributed myself;
7. None of this work has been published before submission

Signed:..... Date:.....

Abbreviations and Nomenclature

ANN	Artificial Neural Network
ARX	Autoregressive exogenous model
EA	Electrode Array
ECR	Extensor Carpi Radialis
EMMILC	Estimation-based Multiple Model Switched Iterative Learning Control
EMMSAC	Estimation-based Multiple Model Switched Adaptive Control
ERGO	Ethics and Research Governance Online
FCR	Flexor Carpi Radialis
ILC	Iterative Learning Control
IRC	Isometric Recruitment Curve
LAD	Linear Active Dynamics
MIMO	Multiple Input Multiple Output
MMAC	Multiple-Model Adaptive Control
PID	Proportional Integral Derivative
PWM	Pulse Width Modulation
RBD	Rigid Body Dynamics
RCT	Randomised controlled Trial
SISO	Single Input Single Output
VE	Virtual Electrode

A, B, C, D	System state-space matrices
B_s	Damping
$\mathcal{C}$	Candidate Controller set
e	Tracking error
E/ER	Performance Index
F_p	Fitting accuracy
$G/P_{\hat{p}}$	Lifted plant
$H(s)$	Transfer function of the wrist model
h_{IRC}	IRC constant
$\mathcal{H}$	Initial plant set
I	Identity matrix with compatible size
I_s	Inertia

k	ILC trial
$K(.)$	Design procedure
K_s	Stiffness
K_e	Muscle force equalisation scaling factor
L	Learning operator
$\mathcal{M}$	Graph of system P_p
N_p	Number of candidate plant models
p/c	discrete-time state-space parameterisations
P_p	Unlifted discrete-time system
$\mathcal{P}$	Candidate plant set
$\hat{p}/\hat{c}$	lifted state-space parameterisations
Q/R	Weighted matrices
$Q_{\hat{c}}$	Robust filter
t	time samples
u	Control input signal
u_0/y_0	External input and output Signals
u_1/y_1	Internal input and output Signals
u_2/y_2	Observed input and output Signals
u_c	Co-activation levels
$\mathcal{U}$	Uncertainty space
V_p	Validating accuracy
x	State variable
y	Output response signal
y_{ref}	Reference trajectory signal
Z	Input and output data set
$\vec{\delta}$	Direct gap between two systems
δ	Gap between two systems
Π	Mapping between external signals and internal signals
γ	A positive tuning parameter
ω_n	Natural frequency

Chapter 1

Introduction

A stroke affects approximately 100,000 people in the UK every year, and is the leading cause of death and disability. Over 70% of unilateral stroke survivors have reported impaired contralateral upper-limb function, especially in their hands and wrists [Meyer et al., 2014]. Over four hundred stroke patients were interviewed in [Wyller et al., 1997], and reported that impaired upper-limb function was the main reason for their decrease in subjective well-being one year after stroke. Another survey of stroke survivors found that they were frustrated, angry and disappointed by rehabilitation often neglecting their upper-limb dysfunction [Sullivan et al., 2019].

These findings are reflected by evidence showing that intensive (i.e. lasting more than three hours per day) goal-oriented task practice is more effective in promoting recovery post stroke than less intensive rehabilitation [Ballester et al., 2022]. Unfortunately conventional therapy only consists of repeating simple movements assisted by a therapist. This is only effective for patients with less severe impairments who can finish at least a portion of the training on their own, but patients with more severe impairments require assistive technology to provide visual, auditory and tactile feedback during goal-oriented training [Lum et al., 2002].

Functional Electrical Stimulation (FES) is the most popular upper limb assistive technology [Hughes et al., 2014]. It has been shown to encourage voluntary effort and reduce dependence on personal carers, and hence can significantly improve quality of life [Anderson, 2004]. In a survey of over four hundred patients, carers and healthcare professionals, 84% stated that FES was more safe, evidence-based and suitable for home-use during upper-limb rehabilitation compared to other assistive technologies [Hughes et al., 2014]. However, it is clear that current FES devices are inadequate and cannot assist intensive goal orientated task practice. Existing FES devices typically use one or two pairs of large electrode pads above the target muscle to activate one or two muscle groups. These are simple to use, but at a cost of poor muscle selectivity when

assisting finger-level movements [Donovan-Hall et al., 2011]. Accurate electrode positioning is also crucial to performance, which many users cannot accomplish.

To address poor muscle selectivity, electrode arrays have been developed by several research groups, and combine multiple electrode pads grouped in a single structure. Although they have been applied to drop-foot, their primary application has been to achieve functional hand and wrist gestures. Typically a simple set-up procedure is used to locate the optimal pad(s) which induce the desired movements. However, the set-up takes too long (>30 minutes) and is not suited for a home-use scenario. This is a critical limitation to both user acceptance and high-intensity rehabilitation. The remarkable performance has been achieved using Iterative Learning Control (ILC), an approach which harnesses the repeated nature of FES rehabilitation training to improve accuracy. A data driven ILC approach has been demonstrated which can achieve an average joint error of less than five degrees during pointing, pinching and hand opening gestures [Freeman, 2014]. However, this requires a large number of identification tests and takes approximately 10 minutes to perform. When the desired gesture is modified, it must be repeated.

The aim of this thesis is to develop an FES array control approach that significantly reduces the time taken to deploy. This would enable FES arrays to be used in the home, potentially bringing intensive goal-orientated rehabilitation to millions of users. Ultimately the system should support the wide variability of daily hand activities used in every day life [Dollar, 2014].

The approach taken is inspired by a multiple model adaptive control (MMAC) framework that has been demonstrated with conventional single pad electrodes in a non-ILC setting [Brend et al., 2015]. This MMAC framework involves designing a set of underlying models that may represent the human arm dynamics, and then selecting the controller associated with the model that best fits the measured data. In this way MMAC adapts to effects like fatigue and spasticity, and can potentially negate the need for identification tests (if the set of models is sufficiently large). Tests with MMAC were promising, and it is the only FES controller to be tested with multiple healthy/impaired subjects in experiments that induce full fatigue.

1.1 Research Aim and Contributions

This thesis aims to address the above limitations by combining the accuracy of ILC with the robustness properties of MMAC and its ability to reduce or even eliminate identification tests. It builds on the estimation-based multiple model switched ILC (EMMILC) introduced in [Freeman and French, 2015] and constitutes the first implementation of multiple model adaptive ILC within FES based rehabilitation. It will be developed first

using single-pad electrodes, before being expanded for application to electrode array technology in the later chapters of this thesis.

The main contributions of research are as follows:

- This thesis performs the first comprehensive experimental verification of the EMMILC framework, where a novel multiple-model design procedure is developed that generates the minimum number of controllers needed to stabilise a given uncertainty space. This thesis also constructs an uncertainty space of dynamic models that realistically capture the true range of physiological dynamics encountered during FES based stimulation of the wrist. Both components are underpinned by a well established theoretical framework based on the gap metric.
- This research produces experimental results using EMMILC applied to a realistic upper-limb FES application that maintain high levels of tracking performance in the presence of model uncertainty, fatigue and electrode misalignment. For the first time, these findings have demonstrated a significant improvement over conventional ILC algorithms applied to upper-limb stroke rehabilitation, achieved without the need for extra identification tests. They show that EMMILC can deliver the robustness necessary to adapt to the variety of situations encountered in a home scenario.
- This research also develops spatial misalignment models for both single-pad electrodes and electrode arrays. This is the first application of EMMILC using electrode arrays. These spatial misalignment models are used to derive a realignment ILC strategy that can physically adjust stimulation sites. Numerical verification of the realignment EMMILC confirms its capability of significantly reducing spatial errors.
- To implement realignment EMMILC, this research also designs and manufactures the first camera-based low-footprint hardware array platform, which is suitable for home-use. Experimental results confirm its effectiveness to deliver selective stimulation and its compatibility with the realignment EMMILC approach. They also demonstrate the feasibility of EMMILC in addressing the primary challenges for upper-limb FES rehabilitation in practice.

This research has featured in the following publications:

- J. Zhou, C. T. Freeman and W. Holderbaum, "Multiple-model iterative learning control with application to stroke rehabilitation," *Control Engineering Practice*, 154, 106134, DOI: 10.1016/j.conengprac.2024.106134, 2025,
- J. Zhou, C. T. Freeman and W. Holderbaum, "Multiple Model Iterative Learning Control for FES-based Stroke Rehabilitation," *2023 American Control Conference (ACC)*, May 31 - June 2, 2023

- J. Zhou, C. T. Freeman and W. Holderbaum, "Multiple Model Iterative Learning Control with Application to Upper Limb Stroke Rehabilitation," *2023 International Interdisciplinary PhD Workshop (IIPHDW)*, May 3 - May 5, 2023

1.2 Thesis Structure

The organisation of this thesis is as follows:

Chapter 2 performs a comprehensive review of the literature and confirms that none of the existing FES studies based on a single-pad electrodes or electrode arrays can adapt effectively to fatigue and spasticity, which limits the feasibility of these upper-limb FES control solutions to achieve adequate robust performance. This subsequently justifies employing ILC approach.

Chapter 3 presents a comprehensive overview encompassing ILC methods utilised in FES-based rehabilitation, along with a summary of strategies for the robust analysis of ILC performance. A general ILC method and a robust filter used in this research are also defined.

Chapter 4 reviews the current multiple-model control approaches with an emphasis on their drawbacks, and motivates EMMILC which embeds a general form of uncertainty, and guarantees long-term robust stability. Theoretical properties are summarised and a practical multiple-model design procedure is developed.

Chapter 5 simulates the designed EMMILC framework on the key rehabilitation problem of wrist extension, and also compares its performance with conventional ILC design.

Chapter 6 confirms the proof of concept by applying EMMILC experimentally with unimpaired participants using single-pad electrodes. As in the previous simulations, experimental results are provided to compare EMMILC and conventional ILC in handling muscle fatigue and electrode misalignment.

Chapter 7 investigates the effect of single-pad electrode misalignment on conventional ILC and EMMILC approaches. It develops a systematic misalignment model and evaluates the performance degradation caused by spatial errors, highlighting the necessity of electrode array reconfiguration.

Chapter 8 extends the EMMILC framework to electrode arrays by proposing a rigorous MIMO modeling approach. It introduces a dynamic compensation strategy for array misalignment, and then embeds this strategy within EMMILC. Numerical evaluation is performed to compare the tracking performance of the realignment ILC and EMMILC approaches.

Lastly, Chapter 9 concludes the thesis and proposes the plan of future work.

Chapter 2

Literature Review

Stroke is a sudden and devastating cerebrovascular brain attack, which can be divided into two types. Firstly, cerebral ischemic stroke is caused by a blood clot that blocks blood from entering the brain. Secondly, hemorrhagic stroke is caused by bleeding in the brain due to a physical trauma, necrosis or rupture of the cerebral blood vessels. Both types of stroke can lead to permanent neurological damage or even death. In the UK, 100,000 people are affected by strokes each year, and there are 1.3 million survivors [State of Nation, 2020]. About 80% of survivors have impaired upper limb functional movement [Hayward et al., 2019]. Due to the serious implications of stroke, there has been a surge in research interest focused on stroke rehabilitation in recent years. The following section will present an overview of stroke rehabilitation, including its objectives, the fundamental mechanisms, and the treatment approaches.

2.1 Upper Limb Stroke Rehabilitation

Stroke rehabilitation is a systematic process aimed at enabling stroke survivors who have impaired functional movement to return to an optimal level of motor functions, improve independence, and enhance the quality of life [Brandstater and Shutter, 2002]. The effectiveness of stroke rehabilitation largely depends on neuroplasticity, which encourages brain to fuse new connections in the motor cortex that replace those lost by stroke. The establishment of these new connections allows the brain to 'relearn' lost motor functions, thus supporting functional recovery after stroke. Evidence from previous studies [Dromerick et al., 2015; Zeiler and Krakauer, 2013] has demonstrated that the first three months post-stroke exhibit enhanced neuroplasticity, allowing increased responsiveness to exogenous stimuli and experiences, resulting in improved recovery outcomes. It has been shown that the best recovery outcome is achieved by intensive practice of repetitive functional tasks [Dobkin, 2004; Kwakkel, 2006] which enable the brain to receive the necessary haptic, proprioceptive and visual feedback. Recovery of

upper-limb function is one of the primary goals of stroke rehabilitation. Because those daily living activities involving upper-limb function (e.g. grasping) are significant for personal care. The upper-limb dysfunction reduces the independence of stroke patients in performing personal care activities and adversely affects their quality of life [Maciejasz et al., 2014; Nichols-Larsen et al., 2005]. Effective upper-limb rehabilitation can be achieved through repetitive task training. French and Watkins [2016] investigated the effectiveness of repetitive practice after stroke by evaluating 33 trials with 1853 participants. The evidence demonstrated that intensive repetitive task training can effectively enhance upper-limb motor function, with benefits lasting up to six months post-therapy.

Conventional therapy consists of repeating movements assisted by a therapist and has been found to be ineffective, with only 32% of patients recovering upper limb function after three months and only 36% reporting a full recovery after twelve months [Sturm et al., 2002]. This is because conventional therapy tasks are not usually intensive or goal-orientated, and do not encourage voluntary effort which reduces the outcome of stroke rehabilitation [Burridge and Ladouceur, 2001; Sinkjaer and Popovic, 2003]. A key issue is that many patients are unable to perform upper limb movements without assistance, and therefore do not get feedback and therefore do not recover the function lost from stroke.

To address this issue, assistive technology directly assists upper-limb movements using electrical or mechanical devices. They facilitate intensive training by automating training execution, consequently minimising clinical contact time with therapists and encouraging voluntary effort [Hughes et al., 2014]. Most end users of assistive technology prefer to practice goal-oriented upper-limb tasks such as washing, dressing, cooking, and eating with knife and fork [Sivan et al., 2014; van Ommeren et al., 2018]. Assistive technology can achieve these goal-oriented task practice using real analog games [Hochstenbach-Waelen and Seelen, 2012]. These can be implemented using a variety of advanced technologies, including virtual reality [Saposnik and Levin, 2011], robotic therapy [Mehrholz et al., 2009], constraint induced movement therapy [Sirtori et al., 2010], and functional electrical stimulation (FES) [Langhorne et al., 2009]. They have the potential to be performed outside the hospital without therapist's support [Reinkensmeyer et al., 2012], thereby offering the possibility for home-based upper-limb stroke rehabilitation with enhanced cost efficiency [Hughes et al., 2014].

2.2 Functional Electrical Stimulation

Among these assistive technologies, Hughes et al. [2014] investigated 152 health care professionals, and 63% of them thought FES is more safe, evidence-based, suitable for home-use, durable and reliable than the other assistive technologies, which made FES

the most popular upper limb therapy. FES comprises a sequence of electrical pulses (see Figure 2.1) which are used to artificially activate muscle nerves. FES is usually applied using a pair of electrode pads placed on the skin above the target muscle. The application of FES was first introduced by Liberson et al. [1961] for lower limb rehabilitation to address drop-foot and was recommended by Teasell et al. [2003] several years later as an effective therapy for the hemiplegic upper limb. In recent year, the latest UK National Clinical Guidelines for stroke [London: Intercollegiate Stroke Working Party, 2023] strongly recommended using FES during daily practice of repeated upper-limb movements. This indicates that FES has gained widespread clinical acceptance, especially for upper limb treatment.

Many clinical studies have been carried out to investigate the effect of FES on stroke participants with impaired upper-limb function. These employed FES to assist exercise over a number of weeks, and used clinical and functional assessment measures to gauge its effect, typically the Fugl-Meyer Assessment (FMA) and Action Research Arm Test (ARAT). Veerbeek et al. [2014] performed a meta-analysis of randomised controlled trials (RCTs) which used FES to systematically examine its effectiveness. They found that 22 RCTs with 894 subjects demonstrated that neuromuscular stimulation of the wrist/finger flexors/extensors has a significant beneficial effect on impaired motor function of the paretic upper limb function and muscle strength. They also found that 25 RCTs with 492 subjects showed that electromyography-triggered neuromuscular stimulation of the wrist/finger extensors has a significant beneficial effect on measures of upper limb impairment including arm-hand activities. Howlett et al. [2015] performed a similar meta-analysis of 8 RCTs with 192 participants, and found that impaired upper limb activities are effectively improved by FES.

2.2.1 Commercial Systems

With the development of FES approach, a variety of commercial FES systems have been clinically trialed. These systems can be categorised into implanted, semi-implanted percutaneous, and transcutaneous electrode types. The implanted FES systems [Keith et al., 1989] such as *Freehand* [Triolo et al., 1996] and percutaneous FES systems [Handa et al., 1989] such as *NECFesmate* [Triolo et al., 1996] surgically implant the electrodes on the target muscle sites identified prior to surgery. However, the electrodes need invasive and costly surgery to implant and must be precisely replaced. Also, the skin interface of the external control unit requires periodical maintenance, which is inconvenient for users [Peckham and Creasey, 1992].

On the other hand, transcutaneous FES electrodes are placed on the surface of skin and are inexpensive and convenient, making them far more popular. Existing FES systems typically employ one or two pairs of large (generally $5cm \times 5cm$) electrical pads to activate one or two muscle groups [Keller and Kuhn, 2008; Popović et al., 2013].

However, they provide poor muscle selectivity when used to assist movements such as finger-level gestures [Ward et al., 2020]. The most advanced commercial system is the *NESS Handmaster* system [Snoek et al., 2000] and its improved version *Bioness-H200* [Micera et al., 2010], provides more muscle selectivity as it can activate and control five different muscles of the hand/wrist. This system requires precise placement of the electrodes within a set-up session, and this alignment is then maintained in future sessions as the system comprises a large plastic unit that encases the wrist. The FES is applied in open-loop and is preprogrammed by the therapist. However, besides the poor muscle selectivity, there is also evidence to show that the performance of the large single-pad systems above highly depends on the placement of the electrodes, and misalignment of pads could lead to discomfort [Micera et al., 2010] and degraded effectiveness [Crema et al., 2018].

2.2.2 Electrode Arrays

To target greater selectivity and reduce fatigue, academic research in recent years has developed transcutaneous electrode arrays comprising multiple electrode pads combined in a single structure. Electrodes are either arranged in a generic pattern or are placed specifically to target the underlying geometry of muscle groups. Systems using the former approach employ a large number of electrodes, but have few independent stimulation channels. Prominent examples are Shefstim [Gopura et al., 2010], SMARTmove [SMARTmove project, 2020] and INTFES [Velik et al., 2011] which support 64, 24 and 16 electrodes respectively, each with a single stimulation channel that can be demultiplexed to a set of desired electrode pads.

Systems which adopt the alternative approach of targeting specific muscle groups use fewer electrode elements, but typically use an independent channel for each muscle group. A leading example of this type is the *HandNMES* system [Snoek et al., 2000], in which 10 independent channels of stimulation are produced by a customised RehaStim stimulator with two DeltaStim demultiplexers (Hasomed GmbH, Magdeburg, Germany).

As FES systems continue to advance, the application of electrode arrays has been increasingly employed to assist upper limb movements. Bijelić et al. [2004] and Bijelić et al. [2005] positioned two 6×4 electrode arrays at the dorsal and volar sides of the forearm. Each electrode was triggered by switching each pad in turn, and the optimal pad was located by therapists. The functional grasp was generated without coupling from the wrist. A more advanced method is using a metric to find the optimal electrode location. Popović and Popović [2009] configured the same array and sequentially activated each pad, but recorded eight pads that resulted in a minimum error between measured and desired joint angles. The functional grasp was produced with sufficient small deviation of wrist and finger. O'Dwyer et al. [2006] placed a 2×2 array on the

patient's forearm. All of the pad configurations were tested, and sensory data were recorded. The optimal configuration was selected by following a metric, which had the hand extension angle between $15^\circ \pm 5^\circ$, and both of the finger flexion and hand adduction/abduction were less than the thresholds of 25% of their maximum angles. A more sophisticated approach selected a group of adjacent electrodes to form a virtual electrode (VE), Gopura et al. [2010] shifted a 2×2 VE to the next adjacent VE along the 8×8 Shefstim array so that each VE could be tested sequentially, in order to select the optimal VE, which is similar to the single-electrode identification procedure. However, it could take 12 to 37 minutes [Prenton et al., 2014] for each VE identification, which is time-consuming for users.

To address this problem, Malešević et al. [2010a] and Malešević et al. [2010b] positioned a 4×4 array at the dorsal side of forearm, and visually inspected and recorded the evoked flexion in a form to train an artificial neural network (ANN), in order to distinguish between the waveform shapes of different hand responses instead of continuous activation for identification of virtual electrodes. As a result, the ANN method achieved 100% accurate classification on the training set, and was validated on all data sets to yield 90% accuracy. Nevertheless, a bespoke ANN was required for different patients, which was inconvenient and hence the clinical feasibility was limited, but no such extra time was mentioned in this study. Imatz-Ojanguren et al. [2016] placed a 32 electrode matrix on the wrist posterior/anterior. A recurrent fuzzy ANN was trained with 3 fuzzy terms (Gaussian membership functions) and wrist and ring finger feedback, in order to model FES evoked wrist, thumb, and finger movements, hence reducing the set-up time. The mean accuracy of the neural network was in the range of 60% to 99%, which was deemed acceptable. However, the training protocol required 45 minutes for each of the 6 subjects, which is very time-consuming. Only one random electrode was activated at a time, which could be uncomfortable to patients and induce inaccurate movements and hence inaccurate training data.

Keller et al. [2006a] positioned a 10×6 array at the dorsal side of forearm. A model-based closed-loop real-time controller was used based on muscle model that incorporates linear activation dynamics and static nonlinearity [Le et al., 2010], in order to identify the VE with a higher accuracy compared to the previous approaches, and produced the strongest force for a specific finger but had the least coupling with other fingers. A recursive algorithm was employed to identify the linear part of wrist model and adjust parameters online to adapt to time-varying effects. However, it was illustrated that although the parameters changes were adapted, the tracking accuracy was not sufficiently good during the whole tracking task. Also, the model identification took time, which was not measured in this study, but it significantly increased the total set-up time. To enhance performance in upper-limb exercises, a variety of FES controllers have been developed for a general class of FES systems. These will be reviewed in the next section.

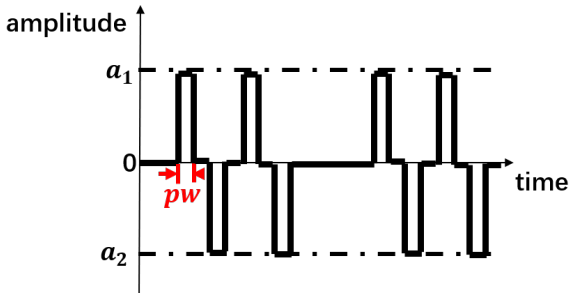

FIGURE 2.1: Symmetric FES impulses (two periods) with amplitudes equal to a_1 and a_2, and a pulsewidth of pw.

2.3 General FES controllers

Meta-analyses confirm that FES control approaches used in clinical upper-limb studies are still overwhelmingly open-loop or triggered by electromyography [Kristensen et al., 2022]. Open-loop FES controllers are typically feasible for clinical use due to their simple sensor-free implementation. Nevertheless, the absence of feedback corrections in these controllers often results in poor accuracy. A small number of clinical studies have employed simple closed-loop feedback systems [Hodkin et al., 2018; Pelton et al., 2012; Resquín et al., 2016a; leung Chan et al., 2009], which incorporate real-time feedback correction and can adapt to disturbances. However, their tracking accuracy is still relatively low, particularly due to the slow system response and onset of muscle fatigue. Controllers often require extensive tuning for each subject [Wiarta et al., 2020; Resquín et al., 2016b] which is impractical in clinical practice due to time constraints and lack of expertise. Higher accuracy tracking has been achieved using model-based FES upper-limb control strategies, including model predictive [Wolf and Schearer, 2022; Westerveld et al., 2014], optimal [Sa–e et al., 2020], active disturbance rejection [Liu et al., 2020], and sliding mode [Oliveira et al., 2017; Rouse et al., 2016; Wu et al., 2017] control. To avoid the need for time-consuming identification, [Tan et al., 2011; Razavian et al., 2018; Wolf and Schearer, 2019, 2018] used only partial model information, however this degraded tracking accuracy. Like all the above methods, a further drawback was their inability to adequately compensate for fatigue, spasticity and other physiological effects.

Adaptive FES model-based controllers have attempted to improve performance. A prominent example is multiple-model adaptive control (MMAC) [Brend et al., 2015] which defines a set of 'candidate' plant models, and a corresponding set of optimal controllers. A bank of Kalman filters are used to switch in the controller whose model best fits the observed plant data. An experimental evaluation with five subjects performing isometric elbow force tracking showed it improved accuracy by 22% compared with standard optimal control. Together with [Wolf et al., 2020], this is the only model-based upper-limb controller tested in experiments with multiple subjects that induced prolonged muscle fatigue. There have been other significant advancements

in robust upper-limb FES controllers, including switched designs to address electromechanical delays [Allen et al., 2022a; Sharma et al., 2011], varying geometry of the upper-limb muscles [Allen et al., 2022b], or co-activation of antagonistic muscles [Sun et al., 2023]. However, they cannot provide guaranteed high performance tracking in the presence of arbitrarily large, unstructured model uncertainty. These approaches have been tested with unimpaired subjects. With one exception [Alibeji et al., 2017], they have not progressed to tests with neurologically impaired participants.

2.4 Iterative learning control

Iterative learning control (ILC) is formulated for systems that repeat the same finite duration tracking task over and over again, and aims to capture the idiom that 'practice makes perfect'. ILC has demonstrated significant potential of being applied across diverse fields, supported by both theoretical frameworks and experimental validations. In manufacturing and robotics, ILC enhances precision in repetitive tasks such as pick-and-place operations [Uchiyama, 1978; Arimoto et al., 1984b; Gunnarsson and Norrlöf, 2001], and industrial printing [Blanken et al., 2020; Blanken and Oomen, 2019]. For energy physics, ILC optimises free-electron lasers [Rogers et al., 2010; Rezaeizadeh and Smith, 2017], and tokamak plasma control for nuclear fusion [Felici and Oomen, 2015]. Precision mechatronics leverage ILC for servo systems [Paszke et al., 2016, 2007] and additive manufacturing [Wang et al., 2018; Balta et al., 2024]. Other ILC applications include high-precision quantum control using data-driven gradient ILC [Wu et al., 2018], and optimisation of feed conversion rate in broiler production [Johansen et al., 2019]. Healthcare is one of the most popular ILC applications. Advanced researches include drop foot neuroprosthesis for gait [Seel et al., 2016; Nahrstaedt et al., 2008b], ventricular assist devices for avoiding the dilatation of the ventricle [Ketelhut et al., 2019], and also FES-based upper-limb stroke rehabilitation [Hughes et al., 2009; Freeman et al., 2012].

ILC is one of the few model-based control schemes that have been applied to FES-based upper-limb control with impaired patients. It has shown its success in five clinical trials [Freeman, 2016] with more than 30 patients with stroke [Kutlu et al., 2016a] or multiple sclerosis [Sampson et al., 2016]. The earlier section 2.1 highlighted that achieving effective rehabilitation outcomes depends on the intensive repetition of goal-oriented task training. This has been demonstrated to facilitate neuroplasticity and improve motor recovery of the upper limb. This repetitive nature of rehabilitation training inherently aligns with the operational principles of ILC. As a result, ILC stands out among all FES controllers as a principled method that is particularly well-suited to the clinical setting and repetitive nature of rehabilitation exercise.

Beyond post-stroke motor therapy, iterative-learning control (ILC) has been harnessed for a variety of biometric/biomedical tasks. In cardiovascular support, Ketelhut et al.

[2019] designed a norm-optimal ILC that varies the cycle length of a rotary left-ventricular-assist device so it can follow rapid changes in preload, afterload and heart-rate while avoiding ventricular dilatation or back-flow. Complementary work shows that a learning-based flow-profile regulator can even minimise the stroke-work imposed on the failing ventricle during continuous-flow assistance, highlighting the energy-saving potential of ILC in circulatory devices. In neuromotor restoration, Nahrstaedt et al. applied ILC to a gait neuro-prosthesis, updating stimulation from step to step so that users reproduced a near-physiological walking trajectory Freeman et al. [2012], while Seel et al. [2016] introduced a multivariable learning controller for an adaptive drop-foot stimulator that simultaneously corrected foot pitch and roll, yielding more natural ground-clearance and landing in paretic gait. Collectively, these studies illustrate how ILC's trial-by-trial refinement can extend well beyond stroke rehabilitation to optimise both implantable devices and functional-electrical-stimulation systems across the biometric spectrum.

2.5 Summary

A variety of control approaches for electrode arrays have been reviewed (Table 2.1). The initial approaches used a manual search with no performance metric and produced finger volar/dorsal flexion/extension with the wrist deviating by less than 15°. Subsequent studies used automatic searching employing various metrics, which produced a small deviation in the wrist, finger or the hand extension angle, and finger flexion and hand adduction/abduction were within the pre-defined ranges that correspond to their metrics. Following this, artificial neural network approaches were employed to speed up the identification, and the reviewed studies trained the ANN with an accuracy which varied from 60% to 100%. Model-based ILC approaches were also employed to achieve a higher tracking accuracy, and the reviewed studies showed that the tracking errors were reduced and typically less than 5 degrees after a few ILC trials. However, all the approaches must be repeated after any array movement or a change in desired gesture, and all of these approaches are very time-consuming due to the set-up process and model identification, which is inconvenient for practical use. Also, none of these studies can adapt to muscle fatigue/spasticity, which limits their feasibility to achieve satisfactory robust performance. These limitations fundamentally limit the ability of FES to deliver intensive, goal-orientated therapy in the homes of people with stroke. The next chapter will comprehensively review the general methods of ILC, including robustness analysis and implementing details in this research.

TABLE 2.1: Review of the existing EAs, VE identifications and corresponding configurations.

Source	Size of electrodes	cathode layout	Stimulator	Sensor used for data capture	VE identification	Criteria	no. of subjects
Bijelić et al. [2004]	single electrode $5cm \times 8cm$	6×4 array, $1cm^2$ pad	Actigrip CS, 4 channels	data glove, six joint angles were measured	**manual**	sufficient good finger flexion/extension tracking	3
Bijelić et al. [2005]	single electrode $5cm \times 8cm$	6×4 array	Actigrip CS, 4 channels	four goniometers, six joint angles were measured	**manual**	effective flexion for palmar grasp, but it was degraded by hand-forearm movement	3
O'Dwyer et al. [2006]	two multi-pad electrodes: bipolar setup	2×1 array and 2×2 array, $2.5cm$ diameter electrodes	Neurotech NT2000, 2 channels	glove with accelerometer-based goniometer and flex sensors, four angles were measured	automatic	The functional grasp can be evoked with small standard deviation (hand extension of $15° \pm 5°$, finger flexion $<$ threshold, hand adduction/abduction $<$ threshold)	10 (healthy) patients to capture healthy motion
Popović and Popović [2009]	single electrode $7cm \times 10cm$	6×4 array, $0.8cm^2$ circular pad	UNA-FET electronic stimulator, 4 channels	flexible goniometers, seven joint angles were measured	**automatic**, VE has the minimum aggregate error	functional grasping was evoked with small variabilities, however, the joint angles were small	6
Gopura et al. [2010]	single electrode, $7cm \times 7cm$	8×8 array	Stimulator designed by Sheffield Teaching Hospitals NHS Foundation Trust, 64 channels	5-camera Qualisys motion capture system (Proreflex, Qualisys AB, Sweden)	automatic, 2×2 VE	maximum value of dorsiflexion and inversion angles observed during the twitch response	10

TABLE 2.2: Review of the existing EAs, VE identifications and corresponding configurations (continued).

Source	Size of electrodes	cathode layout	Stimulator	Sensor used for data capture	VE identification	Criteria	no. of subjects
Malešević et al. [2010a]	**INTEFES** single electrode, unknown size	4 × 4 square array, unknown pad size	FES module (monophase), unknown channel	flexible goniometers, three joint angles and muscle twitch responses were measured	Could be switched between manual/automatic	**ANN** was trained to distinguish between different types of hand movements and define correlation of each pad and activated muscle beneath	6 (healthy) to distinguish hand movement
Malešević et al. [2010b]	**INTEFES** single electrode, unknown size	4 × 4 array, unknown pad size	FES module (monophase), unknown channel	ADXL 330 accelerometer to record hand movement	automatic	**ANN** was trained to distinguish between wrist or fingers flexion/extension detect correlation of each pad and activated muscle beneath	3 (healthy) to distinguish wrist or fingers flexion/extension
Imatz-Ojanguren et al. [2016]	single electrode, unknown size	32 pads array corresponds to muscle geometry	*FES: a stimulator* from *TECNALIA Research & Innovation*, unknown channel	a sensorized glove based on inertial and fiber-optic bend sensors	automatic	mean accuracy of the ANN was in the range of 60% to 99%	6
Velik et al. [2011]	**INTFES** single electrode, unknown size	4 × 4 array, unknown pad size	INTFES stimulator, 1 channel	goniometers	automatic (minimum aggregate error)	N/A	N/A

TABLE 2.3: Review of the existing EAs, VE identifications and corresponding configurations (continued).

Source	Size of electrodes	cathode layout	Stimulator	Sensor used for data capture	VE identification	Criteria	no. of subjects
Keller et al. [2006a]	single electrode $5cm \times 5cm$	10×6 array, $1cm^2$ pad	Compex Motion stimulator, 4 channels	four finger force sensors to measure force response	**automatic** (random order)	The measured force was shown to track estimated force during hand grasp with the presence of coupling, the muscle fatigue was adapted	8
Kutlu et al. [2016b]	single electrode	4×6 array	FES stimulator (Odstock Medical Ltd., Salisbury, UK), 4 channel	PrimeSense Carmine 1.09 (Apple Inc., California) depth camera to measure hand and wrist joint angles	automatic	**Newton method iterative learning control** (section 3.1.7) to adjust FES	4 (stroke), 2 (healthy)
Excell et al. [2013], Freeman [2014]	single electrode	5×8 array	modified commercial stimulator (Odstock, UK), 4 channel	data glove (5DT 14 Ultra, 5DT, USA) to measure 14 angles of flexion/extension and radial/ulnar deviation	automatic	**Newton method iterative learning control** to adjust FES by minimizing an objective function in terms of the difference between desired movement and measured response	N/A

Chapter 3

General Methods

The previous chapter showed that iterative learning control (ILC) is one of the most successful control methods to adjust FES within stroke rehabilitation both using individual pads and via electrode arrays. Therefore, this chapter provides an overview of ILC, focusing on general ILC methods that have been used in FES based rehabilitation. It also summarises the analysis and design approaches used in this thesis that have scope to improve current ILC performance in this field.

3.1 Control Objectives

Fundamentally, ILC is formulated for systems that repeat the same finite duration tracking task over and over again, and aims to capture the idiom that 'practice makes perfect'. It does this by updating the control input for the current trial at the task using information from previous trials. The basic ILC update law studied in [Arimoto et al., 1984a] has the form

$$\begin{aligned} u_{k+1} &= u_k + f(e_k), \\ e_k &= y_{\text{ref}} - y_k. \end{aligned} \tag{3.1}$$

Here u_{k+1} is the control signal for the $(k+1)^{th}$ trial (sometimes termed 'iteration') and $f(\cdot)$ is some function of the tracking error signal e_k, which is the difference between the desired reference trajectory y_{ref} and the measured system plant output y_k. The general framework of ILC is illustrated by Figure 3.1.

ILC aims to force tracking error e_k to be bounded or ideally converge to zero after a finite number of trials. In addition, the control input signal u_k is also required to converge to a fixed control signal u_d. Mathematically, the control objective can be expressed as

$$\lim_{k\to\infty} \|e_k\| = 0, \qquad \lim_{k\to\infty} u_k = u_d. \tag{3.2}$$

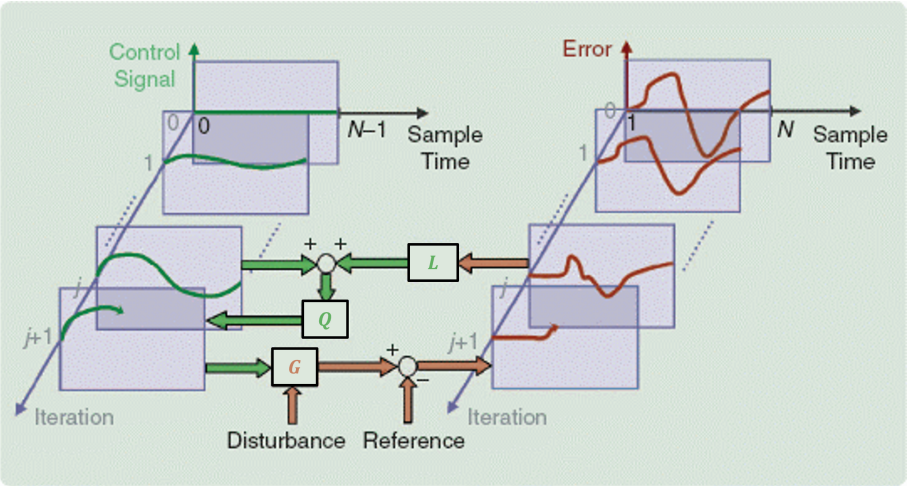

FIGURE 3.1: General ILC update framework in two dimensions (time and trials) described by (3.1) with a filter Q applied. The learning operator is denoted L, the lifted plant is denoted G, and j is the trial number. Figure from [Bristow et al., 2006].

where $\|\cdot\|$ is a suitable norm.

ILC is a two dimensional process, since it operates along-the-trial and from trial to trial. Typically the system is described in discrete-time and the former dimension is therefore captured using the sample number $t = 0, 2, 3, ..., N-1$ where N is the number of samples in one trial [Bristow et al., 2006]. To aid analysis, ILC can then be 'lifted' from the time dimension by stacking the input and output signals into vectors of length N, and writing the system dynamics and ILC update equations as static mappings between these vectors. This then embeds the along-the-trial dynamics into a simple form.

For example, consider the linear time-invariant (LTI) discrete-time single input single output (SISO) system with state-space dynamics given by

$$\begin{aligned} x_k(t+1) &= Ax_k(t) + Bu_k(t), \quad x_k(0) = x_0 \\ y_k(t) &= Cx_k(t) + Du_k(t), \quad t = 0, 1, ..., N-1 \end{aligned} \tag{3.3}$$

where A is an $n \times n$ matrix, B is an $n \times 1$ vector, C is a $1 \times n$ vector and D is a scalar. The initial state is reset to x_0 at the start of the next trial. The lifted input and output signals on the k^{th} trial are respectively

$$u_k = [u_k(0), u_k(1), u_k(2), ..., u_k(N-1)]^T \in \mathbb{R}^N, \tag{3.4}$$

$$y_k = [y_k(0), y_k(1), y_k(2), ..., y_k(N-1)]^T \in \mathbb{R}^N \tag{3.5}$$

The lifted system dynamics for system (3.3) over the k^{th} trial are then

$$y_k = Gu_k, \tag{3.6}$$

where the 'lifted' plant G is the Toeplitz matrix

$$\begin{bmatrix} D & 0 & \cdots & 0 & 0 & 0 \\ CB & D & \cdots & 0 & 0 & 0 \\ CAB & CB & \cdots & 0 & 0 & 0 \\ \vdots & \vdots & \ddots & \vdots & \vdots & \vdots \\ CA^{N-2}B & CA^{N-3}B & \cdots & CB & D & 0 \\ CA^{N-1}B & CA^{N-2}B & \cdots & CAB & CB & D \end{bmatrix} \in \mathbb{R}^{N\times N}. \tag{3.7}$$

The reference trajectory signal y_{ref} is

$$y_{\text{ref}} = [y_{\text{ref}}(0), y_{\text{ref}}(1), y_{\text{ref}}(2), ..., y_{\text{ref}}(N-1)]^T \in \mathbb{R}^N \tag{3.8}$$

and the tracking error e_k over the k^{th} trial is computed as

$$e_k = y_{\text{ref}} - y_k. \tag{3.9}$$

The most common class of ILC update selects update (3.1) to take the form

$$u_{k+1} = u_k + Le_k \tag{3.10}$$

where L is an $N \times N$ matrix [Bristow et al., 2006]. The lifted form then enables ILC convergence conditions to be easily computed. From (3.6), (3.9) and (3.10) it is easy to show that

$$e_{k+1} = (I - LG)e_k \tag{3.11}$$

where I denotes the $N \times N$ identity matrix. It follows that the error norm $\|e_k\|$ will **asymptotically** converge to zero as k tends to infinity if

$$\max_i |\lambda_i(I - LG)| < 1. \tag{3.12}$$

where $\lambda_i(A)$ denotes the i^{th} eigenvalue of any $N \times N$ matrix A. Asymptotic convergence may still generate large errors, so many researchers employ the stricter notion of **monotonic** convergence. This requires that

$$\|I - LG\| < 1 \tag{3.13}$$

which follows by applying norms to (3.11) to obtain $\|e_{k+1}\| \leq \|I - LG\|\|e_k\|$. Here the l_2-norm of bounded signals is assumed, and will be in the remainder of the report unless otherwise stated.

Compared with open-loop and simple closed-loop FES controllers reviewed in earlier section, ILC bridges their gap by using offline feedback across repeated trials. ILC achieves this by using information from previous executions (like closed-loop systems),

but without needing real-time feedback (like open-loop systems). This makes ILC particularly suitable for structured, repetitive tasks like those in stroke rehabilitation, where long-term accuracy and convergence are critical. Different structures of ILC updates are now reviewed in the next section. Early ILC algorithms do not use model information [Arimoto et al., 1984a; Nahrstaedt et al., 2008a; Freeman et al., 2005], thereby maintaining their widespread popularity due to simplicity. This has meant they have also been applied to FES based stroke rehabilitation and are now reviewed.

3.1.1 P-type ILC

Proportional 'P-type' ILC was proposed by Arimoto et al. [1985] and is given by

$$u_{k+1}(t) = u_k(t) + \beta e_k(t) \tag{3.14}$$

where β is a positive scalar selected by the designer. Comparing with the general form (3.10), this corresponds to $L = \beta I$, so that the error evolution (3.11) for P-type ILC is

$$e_{k+1} = (I - \beta G)e_k \tag{3.15}$$

Hence asymptotic convergence condition (3.12) becomes

$$\max_i |\lambda_i(I - \beta G)| < 1, \tag{3.16}$$

which simplifies to $|1 - \beta D| < 1$ given the form of G of (3.7). As shown in [Arimoto et al., 1985], this means P-type ILC is only suitable for systems with $D \neq 0$ (i.e. systems with relative degree 0). Therefore, this is a serious limitation for P-type ILC. According to (3.13), P-type ILC monotonically converges if

$$\|I - \beta G\| < 1 \tag{3.17}$$

which is clearly even more restrictive than the previous condition. This means P-type usually has large error norms before finally converging. The P-type ILC approach has been used to control a single-pad electrode in drop foot rehabilitation [Nahrstaedt et al., 2008a; Müller et al., 2017] and in upper limb stimulation [Dou et al., 1999].

3.1.2 D-type ILC

To expand the class of systems on which ILC can be applied, a derivative 'D-type' update form was proposed in [Arimoto et al., 1985] and discretised in [Saab, 1995] to give

$$u_{k+1}(t) = u_k(t) + \beta[e_k(t+1) - e_k(t)]. \tag{3.18}$$

in which $e_k(t+1) - e_k(t)$ denotes the error difference with respect to successive time samples, and β is still a positive gain. It was shown in [Arimoto et al., 1985] that D-type ILC expands the class of admissible systems compared to P-type ILC. In particular, it guarantees asymptotic convergence with systems whose state-space D term equals zero, provided

$$|I - \beta CB| < 1 \tag{3.19}$$

holds. This follows directly by applying the update form (3.18) within condition (3.12). Therefore D-type ILC expands the class of admissible systems to include those with relative degree 1.

However, a new limitation arises from D-type ILC since its use of the error derivative makes the algorithm vulnerable to noise and disturbances. Thus, D-type ILC is rarely used in practical control problems and has not been applied within rehabilitation.

3.1.3 Phase-lead ILC

The constraint was further released by the 'phase-lead' ILC algorithm, which was originally proposed by [Park et al., 1998] and expanded in [Freeman et al., 2005] and [Cai et al., 2008]. This has form

$$u_{k+1}(t) = u_k(t) + \beta e_k(t + \lambda). \tag{3.20}$$

Phase-lead ILC shifts the error signal forwards in time by an estimated system time delay λ, in order to compensate for the time delay. The phase-lead ILC has been shown to outperform P-type and D-type ILC in [Freeman et al., 2005].

Comparing with general form (3.10), this corresponds to

$$L = \begin{bmatrix} 0 & \cdots & 0 & \beta & 0 & \cdots & 0 \\ 0 & \cdots & 0 & 0 & \beta & & \vdots \\ \vdots & & \vdots & \vdots & \vdots & \ddots & \vdots \\ 0 & \cdots & 0 & 0 & 0 & \cdots & \beta \\ 0 & \cdots & 0 & 0 & 0 & \cdots & 0 \\ \vdots & \cdots & \vdots & \vdots & \vdots & \cdots & \vdots \\ 0 & \cdots & 0 & 0 & 0 & \cdots & 0 \end{bmatrix} \in \mathbb{R}^{N \times N}. \tag{3.21}$$

It is shown in [Freeman et al., 2005] that Phase-lead ILC only converges to, and maintains, zero error for systems that are pure time delays. However, this can be partially rectified by adding a suitable low-pass filter to the update. Phase-lead ILC has proven successful in FES based stroke rehabilitation since it can provide reasonable tracking

accuracy without requiring a system model. It is applied to the triceps for upper limb reaching tasks and used in a clinical trial [Freeman et al., 2009b].

3.1.4 Gradient descent ILC

To address the limitations of simple ILC structures, the field rapidly expanded to leverage model-based updates in order to provide greater accuracy and convergence properties for wider system classes. Examples of the broad range of model-based ILC approaches are contained in [Bristow et al., 2006; Owens, 2016; Rogers et al., 2023] and the references therein. These ILC schemes have also been applied to FES based upper limb rehabilitation, with standard model-based updates proving most accurate. Tests with stroke participants showed they outperforming conventional model-based strategies by an order of magnitude [Freeman, 2016]. The leading examples are based on optimising a suitably chosen objective function that involves the tracking error. Advantages of these optimisation-based ILC approaches often include accurate performance and satisfactory robustness, together with control over the trial-to-trial convergence properties. This has led to their success in a wide variety of practical applications.

Perhaps the first optimisation-based ILC approach is gradient-descent ILC, proposed in [Furuta and Yamakita, 1987] and later developed in [Owens et al., 2009]. The approach considers the optimisation problem

$$\min_{u_{k+1}} \|e_{k+1}\|^2 \tag{3.22}$$

and applies the gradient descent minimisation approach to solve it. The iterative solution corresponds to the ILC update

$$u_{k+1} = u_k + \beta G^\top e_k \tag{3.23}$$

where the transpose term $G^\top$ is the lifted realisation of the plant adjoint operator. Comparing with general form (3.10), this corresponds to $L = \beta G^\top$ and substituting this learning operator into (3.12) means asymptotic convergence can be achieved if

$$\max_i |\lambda_i(I - \beta G^\top G)| < 1. \tag{3.24}$$

Similarly, substituting $L = \beta G^\top$ into (3.13) means that monotonic convergence can be achieved if

$$\|I - \beta G^* G\| < 1. \tag{3.25}$$

and it follows that scalar gain β must satisfy

$$0 < \beta < \frac{2}{\|GG^\top\|} = \frac{2}{\|G\|^2}. \tag{3.26}$$

However, [Owens et al., 2009] showed that the convergence rate of gradient-descent ILC is often very slow due to the small value of learning gain β needed to satisfy (3.26). This has been confirmed in practical evaluation on electro-mechanical systems [Freeman et al., 2005] and in several applications to FES based stroke rehabilitation such as triceps [Freeman et al., 2009b], only simulation [Soska et al., 2013] and entire forearm [Huo et al., 2020]. Another limitation is the need for a system model to be identified.

3.1.5 Inverse ILC

The inverse ILC approach was proposed by [Harte et al., 2005] and aims to maximise the convergence rate using the update law

$$u_{k+1} = u_k + \beta G^{-1} e_k \tag{3.27}$$

where scalar β denotes the chosen learning rate or step size. The matrix G^{-1} is the inverse of the system dynamics (3.7), and can only be computed if $D \neq 0$ (i.e. the system has relative degree 0). Comparing with general form (3.10), the learning operator corresponds to $L = \beta G^{-1}$. It follows from (3.12) that inverse ILC will asymptotically converge if

$$\max_i |\lambda_i(I - \beta G^{-1} G)| < 1 \quad \Rightarrow \quad |1 - \beta| < 1 \quad \Rightarrow \quad 0 < \beta < 2. \tag{3.28}$$

Similarly, inverse ILC monotonically converges if

$$\|I - \beta G^{-1} G\| < 1 \quad \Rightarrow \quad \|I - \beta I\| < 1 \quad \Rightarrow \quad 0 < \beta < 2, \tag{3.29}$$

and so the available range for learning gain β are the same (and convergence will always be monotonic). Inverse model-based ILC can converge rapidly because if $\beta = 1$, then the error evolution (3.11) becomes

$$e_{k+1} = (I - LG)e_k = (I - \beta G^{-1} G)e_k = (I - G^{-1} G)e_k = 0. \tag{3.30}$$

In other words, the tracking error converges to zero in one trial.

As well as only being applicable to relative degree zero systems, inverse ILC also encounters problems with non-minimum phase plants (having zeros outside the unit circle) since this produces an unstable inverse [Owens and Chu, 2014]. In addition, [Harte et al., 2005] also stated that the algorithm amplifies uncertainties and disturbances, which could lead to degraded tracking performance and even potential in stability issues. Practical studies in robotics confirmed both rapid convergence and poor robustness properties [Ratcliffe et al., 2004], however lack of robustness has meant it has not been applied in rehabilitation.

3.1.6 Norm Optimal ILC

Norm optimal iterative learning control (NOILC) was first proposed by [Amann et al., 1996] and provides an elegant approach to balance convergence speed and robustness properties. For dynamic system (3.6), the control input for the next trial u_{k+1} is computed by solving the optimisation problem

$$u_{k+1} = \arg\min_{u_{k+1}}(||r - Gu_{k+1}||_Q^2 + ||u_{k+1} - u_k||_R^2). \tag{3.31}$$

where Q and R are symmetric positive definite and positive semi-definite weighting matrices respectively. These act as weights to emphasise the reference signal tracking and the change of control signal between adjacent trials, respectively. Here the norm is defined as $\|x\|_W = x^\top W x$ for vector x and compatible symmetric weight W.

It is straightforward to show that minimisation (3.31) is solved using the update

$$u_{k+1} = u_k + R^{-1}G^\top Q e_{k+1}. \tag{3.32}$$

However, the error for the next trial e_{k+1} cannot be directly acquired due to the need for causality. Further manipulation leads to a causal solution using the feedforward ILC update

$$u_{k+1} = u_k + (I + GR^{-1}G^\top Q)^{-1}R^{-1}G^\top Q e_k. \tag{3.33}$$

which was proposed in [Barton and Alleyne, 2009]. Comparing with general form (3.10), the learning operator corresponds to $L = (I + GR^{-1}G^\top Q)^{-1}R^{-1}G^\top Q$. Substituting this into (3.12) means that the tracking error of NOILC asymptotically converges if

$$\max_i |\lambda_i(I - (I + GR^{-1}G^\top Q)^{-1}R^{-1}G^\top QG)| < 1 \tag{3.34}$$

which was shown in [Amann et al., 1996] to be satisfied for all choices of Q and R. The monotonic condition (3.13) is

$$\|I - (I + GR^{-1}G^\top Q)^{-1}R^{-1}G^\top QG)|\| < 1 \tag{3.35}$$

and it was shown in [Amann et al., 1996] that this is equivalent to

$$\frac{1}{1+\sigma^2} < 1. \tag{3.36}$$

where the scalar $\sigma > 0$ denotes the smallest singular value of the lifted plant matrix G. Hence as long as G is full rank (has $D \neq 0$) it will converge monotonically.

Moreover, [Amann et al., 1996] also proposed an alternative implementation comprising a feedforward update combined with state feedback. This differs from the standard ILC structure, and was motivated by improving the robustness of algorithm against

disturbances. This feedback and feedforward NOILC update law is given by

$$u_{k+1}(t) = u_k(t) - (B^T K(t) B + R(t))^{-1} B^T K(t) A[x_{k+1}(t) - x_k(t)] + R^{-1} B^T \xi_{k+1}(t) \quad (3.37)$$

over $t = 1, 2, 3, ..., N$ samples. Here $K(t)$ and $\xi_{k+1}(t)$ denote the state feedback matrix (independent of ILC trial number) and the feedforward term (for the trial $k+1$), respectively. Therefore, $K(t)$ and $\xi_{k+1}(t)$ can be computed offline iteratively by solving the discrete-time Riccati equation [Amann et al., 1996]

$$\begin{aligned} K(t) = A^T K(t+1) A + C^T Q(t+1) C \\ - A^T K(t+1) B (B^T K(t+1) B + R(t+1))^{-1} B^T K(t+1) A, \end{aligned} \quad (3.38)$$

$$\xi_{k+1}(t) = (I + K(t) B R^{-1} B^T)^{-1} (A^T \xi_{k+1}(t+1) + C^T Q(t) e_k(t)); \quad \xi_{k+1}(N) = 0 \quad (3.39)$$

Equations (3.38) and (3.39) are solved recursively in a "reverse" time sequence ($t = N, ..., 3, 2, 1$) with the initial conditions given by $K(N) = 0$ and $\xi_{k+1}(N) = 0$. Additionally, the matrix $x_{k+1}(t)$ in (3.37) denotes the state variable for the $(k+1)^{th}$ trial at time instant t. It can be estimated by $\widehat{x}_{k+1}(t)$ provided by a suitable observer of the form

$$\widehat{x}_{k+1}(t) = A x_{k+1}(t-1) + B u_{k+1}(t-1) + L_e (y_{k+1}(t-1) - C x_{k+1}(t-1)) \quad (3.40)$$

where L_e is the observer gain vector. NOILC has been applied in robotic studies [Ratcliffe et al., 2006a] and in FES based rehabilitation [Freeman et al., 2009b]. In all cases it provided accurate tracking, however it is computationally expensive to implement and requires an accurate model. Furthermore, a predictive NOILC extension [Amann et al., 1998] computes the current control signal in terms of the present and future predicted errors, allowing further adjustment of the convergence rate.

3.1.7 Newton method based ILC

Newton method based ILC was proposed in [Lin et al., 2006] and aims to solve nonlinear ILC problems by applying the Newton method within the ILC framework. It assumes a general form of nonlinear system with the dynamics given in lifted form by the vector mapping

$$y_k = g(u_k). \quad (3.41)$$

The Newton method based ILC update is then given by

$$u_{k+1} = u_k + g'(u_k)^{-1} e_k \quad (3.42)$$

where $N \times N$ matrix $g'(u_k)$ denotes the derivative of the vector function $g(u_k)$ which corresponds to the linearised lifted system dynamics about operating point u_k. Since

the inverse system $g'(u_k)^{-1}$ is difficult to compute in some cases, [Lin et al., 2006] decomposed the update into two separate ILC problems. First (3.42) is rewritten as

$$u_{k+1} = u_k + f_{k+1} \quad \text{with} \quad f_{k+1} = g'(u_k)^{-1} e_k. \tag{3.43}$$

The inverse term $f_{k+1} = g'(u_k)^{-1} e_k$ can then be solved by calculating f_{k+1} such that

$$e_k = g'(u_k) f_{k+1} \tag{3.44}$$

which corresponds to a standard ILC problem with e_k acting as the reference. This is solved in simulation using any suitable ILC method (e.g. NOILC) and avoids computing the inverse directly.

If Newton-based ILC is applied to the linear case, it simplifies to the inverse ILC law (3.27). Convergence conditions and rates were analysed in [Lin et al., 2006] for the nonlinear case. Newton-based ILC has been applied to FES-based rehabilitation. For example, [Freeman, 2014], [Kutlu et al., 2016b] were introduced in the previous chapter, and most notably applied to the FES electrode array problem in [Ward et al., 2020].

3.2 ILC based on 2D systems theory

Previous ILC approaches used information measured on the current trial to update the next control signal and reduce the tracking error in the subsequent trial. However, dynamic changes along the trial may lead to instantaneous degradation of performance or even instability that cannot easily be addressed by trial-to-trial ILC. Therefore, 2D system analysis has been extensively applied to ILC, e.g. in [Ayatinia et al., 2022; Hladowski et al., 2010; Mandra et al., 2019; Rogers et al., 2007]. For analysis purposes, a discrete-time state space uncertain model is often formulated as

$$\begin{aligned} x_{k+1}(t+1) &= A(\alpha)x_{k+1}(t) + Bu_{k+1}(t), \quad x_{k+1}(0) = x_0 \\ y_{k+1}(t) &= Cx_{k+1}(t), \quad t = 0, 1, ..., N-1, \end{aligned} \tag{3.45}$$

where $A(\alpha)$ belongs to a bounded convex set which is defined as

$$\left\{ A(\alpha) : A(\alpha) = \sum_{i=1}^{N} \alpha_i A_i, \quad \sum_{i=1}^{N} \alpha_i = 1, \quad \alpha_i \geq 0 \right\}. \tag{3.46}$$

A general form of ILC update for this repetitive process is given by

$$u_{k+1}(t) = u_k(t) + L_1[x_{k+1}(t) - x_k(t)] + L_2 e_k(t+1), \tag{3.47}$$

where L_1 and L_2 are learning gains that enforce both along the trial and trial-to-trial convergence, respectively. They can be obtained by solving Linear Matrix Inequalities (LMIs) that have been analysed in [Rogers et al., 2007].

3.3 ILC robustness analysis

An essential aspect of ILC that has been widely studied is long-term robust stability [Bradley, 2010; Meng and Moore, 2017; Freeman et al., 2005], which refers to the system's ability to maintain stability after initial convergence, even in the presence of modelling errors. For example, Ratcliffe et al. [2005] showed that a common ILC update will diverge if a multiplicative model uncertainty has a phase angle greater than 90° in magnitude. Addressing long-term stability is especially crucial in a rehabilitation setting to ensure that the intensive FES training remains effective, comfortable and safe over extended periods of use.

To address this, previous robust analysis has focused on parametric uncertainties, which were considered in Ahn et al. [2005]. Here bounds on the Schur stability radius for robust ILC design were produced by considering parametric uncertainties existing in the system's Markov parameters. A learning gain matrix was designed to satisfy this robustness bound. Xu and Xu [2013] dealt with the output-constrained problems with parametric system uncertainties. A new ILC scheme was derived from a novel barrier Lyapunov function to satisfy the constraints. More studies relate to the unstructured uncertainties which do not impose an explicit form of uncertainty. Here P is denoted as the nominal model, and Δ is an arbitrary system operator representing the uncertainty. The additive uncertainty $P + \Delta$ was studied in Donkers et al. [2008], taking a linear uncertainty operator Δ and a linear model that was controlled using norm optimal ILC. Owens et al. [2014] employed the same ILC update under multivariable conditions, but analysed multiplicative uncertainty applied to the linear model. Hätönen et al. [2006] and Freeman et al. [2009c] considered uncertainty in the frequency domain by employing the Fourier transform of the system's impulse response. They found that if the phase margin of the uncertain plant lies within the $\pm 90°$ tube around the nominal plant, then the gradient ILC and inverse ILC updates will have a bounded error norm that monotonically converges to zero. Any delay will violate the convergence condition, but in practice the update is still reasonably robust to a delay. However, these studies still require some highly structured form (e.g. additive or multiplicative) to describe uncertainties, and in practice uncertainties do not fit these forms. Hence the results obtained above are very conservative.

The limitations of the above uncertainty forms were addressed by work in Bradley [2010], which did not assume restrictive forms of uncertainties (e.g. additive, multiplicative or linear operators). It applied a general framework to a class of ILC schemes

and produced bounds for robust stability. It was hence less conservative in practical cases. The stability results in Bradley [2010] were derived by applying the gap metric to the ILC framework, which will be introduced next.

3.3.1 Gap metric

The gap metric was introduced in [Zames and El-sakkary, 1980], and characterises the distance between two dynamic systems in terms of the difference between their graphs. This assumes a standard (non-ILC) setting, with the system running over an infinite time duration. To avoid confusion P will be used to represent an unlifted system operator in the remainder of this thesis, and a subscript will be used to denote its underlying parametrisation. For example, let $p = (A_p, B_p, C_p, D_p)$ be a set of discrete-time state-space matrices, then plant P_p is the system

$$P_p : u_1 \mapsto y_1 : \quad \begin{cases} x(t+1) = A_p x(t) + B_p u_1(t), & x(0) = x_0 \\ y_1(t) = C_p x(t) + D_p u_1(t), & t = 0, 1, \cdots \end{cases} \tag{3.48}$$

Defining the gap first requires the notion of the graph of the system P_p. This is denoted $\mathcal{M}_\mathbf{p}$ and comprises the set of all bounded input and output signals compatible with P_p, e.g. for a SISO plant, the graph is

$$\mathcal{M}_p := \{\omega \in l^2 \times l^2 \quad | \quad \omega = (u_1, P_p u_1)\}. \tag{3.49}$$

Now suppose there is another system, P_{p^*}, with graph $\mathcal{M}^*_\mathbf{p}$. Then the directed gap, introduced in [Georgiou and Smith, 1989], is defined as

$$\vec{\delta}(\mathcal{M}_p, \mathcal{M}_{p^*}) := \sup_{\omega \in \mathcal{M}_p, \omega \neq 0} \inf_{v \in \mathcal{M}_{p^*}} \frac{\|\omega - v\|}{\|\omega\|}. \tag{3.50}$$

This is interpreted as: for every signal pair in $\mathcal{M}_\mathbf{p}$, find the distance to the nearest signal pair in $\mathcal{M}^*_\mathbf{p}$. Then take the largest of these distances. A metric must be symmetrical in P_p and P_{p^*}, and therefore the gap is taken as the largest directed gap between the two systems, i.e.

$$\delta(P_p, P_{p^*}) := \max\{\vec{\delta}(\mathcal{M}_{p^*}, \mathcal{M}_p), \vec{\delta}(\mathcal{M}_p, \mathcal{M}_{p^*})\}. \tag{3.51}$$

3.3.2 Robust Stability

The gap metric was used to characterise the robust stability of a closed-loop system in [Georgiou and Smith, 1989]. This considered the general closed-loop system shown in Figure 3.2, where again P_p is assumed to be an unlifted plant operator.

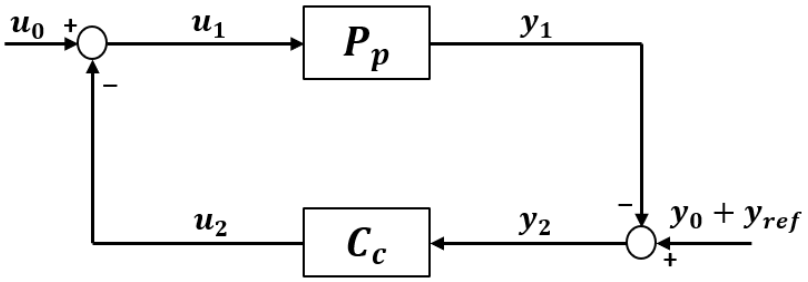

FIGURE 3.2: Closed-loop system structure for ILC robustness analysis.

The system input and output signals are u_1, y_1 respectively. Similarly, C_c is an unlifted control operator with input signal y_2 and output signal u_2. Signal y_{ref} is again the reference trajectory, and u_0, y_0 are disturbance signals. The feedback connection shown in Figure 3.2 is written as $[P_p, C_c]$ with the associated signals

$$u_1 = u_0 - u_2, \quad y_1 = P_p u_1, \quad u_2 = C_c y_2, \quad y_2 = y_0 + y_{\text{ref}} - y_1. \tag{3.52}$$

Stability of the closed-loop system was defined by introducing the mapping between external disturbance and internal signals as

$$\Pi_{P_p//C_c} : \begin{pmatrix} u_0 \\ y_0 \end{pmatrix} \mapsto \begin{pmatrix} u_1 \\ y_1 \end{pmatrix} \tag{3.53}$$

so for the linear case

$$\Pi_{P_p//C_c} = \begin{pmatrix} (I - C_c P_p)^{-1} & -(I - C_c P_p)^{-1} C_c \\ P_p (I - C_c P_p)^{-1} & -P_p (I - C_c P_p)^{-1} C_c \end{pmatrix}. \tag{3.54}$$

The closed-loop system is then said to be gain stable if $\|\Pi_{P_p//C_c}\| < \infty$. Now suppose that controller C_c is designed so that $[P_p, C_c]$ is a stable system, however P_p is then exchanged with a different system P_{p^*}. It was shown in [Georgiou and Smith, 1989] that the gap metric provides a simple condition to establish if the new closed-loop system $[P_{p^*}, C_c]$ is stable. The theorem is stated as follows:

Theorem 3.1. *Given plant P_p and ILC design C_c designed for P_p and let the closed-loop system $[P_p, C_c]$ be stable such that condition 3.61 holds. Assume another system is denoted as P_{p^*}, the system $[P_{p^*}, C_c]$ is also gain stable if*

$$\delta(P_p, P_{p^*}) < \|\Pi_{P_p//C_c}\|^{-1}. \tag{3.55}$$

This analysis was applied to ILC by Bradley [2010], and the key results are summarised in the next section.

3.3.3 Robust Stability of ILC

The ILC plant dynamics (3.6) and update (3.10) do not fit into the structure of Figure 3.2 since they operate in a batch-wise manner. Therefore, Theorem 3.1 cannot be applied. Bradley [2010] overcome this problem simply by redefining the signals and systems in an equivalent form. First the unlifted plant P_p, with $p = (A_p, B_p, C_p, D_p)$ is lifted to produce the matrix

$$P_{\hat{p}} = \begin{bmatrix} D_p & 0 & \cdots & 0 & 0 & 0 \\ C_pB_p & D_p & \cdots & 0 & 0 & 0 \\ C_pA_pB_p & C_pB_p & \cdots & 0 & 0 & 0 \\ \vdots & \vdots & \ddots & \vdots & \vdots & \vdots \\ C_pA_p^{N-2}B_p & C_pA_p^{N-3}B_p & \cdots & C_pB_p & D_p & 0 \\ C_pA_p^{N-1}B_p & C_pA_p^{N-2}B_p & \cdots & C_pA_PB_p & C_pB_p & D_p \end{bmatrix}. \tag{3.56}$$

Then, the ILC plant dynamics (3.6) are written as

$$y_1(k) = P_{\hat{p}}u_1(k). \tag{3.57}$$

This is equivalent to $y_k = P_{\hat{p}}u_k$ where the i^{th} element of vector $u_1(k)$ equals $u_k(i)$. Similarly, ILC update (3.10) is written as

$$u_2(k+1) = u_2(k) - Ly_2(k), \tag{3.58}$$

which enables ILC to be expressed as a conventional discrete-time system, in which each 'sample' is a whole ILC trial. The ILC update can hence be denoted by the lifted operator $u_2 = C_{\hat{c}}y_2$, and likewise matrix $P_{\hat{p}}$ can also be expressed in the operator form $y_1 = P_{\hat{p}}u_1$. It follows that both systems can be written as lifted state-space systems, with respective state-space parameterisations, $\hat{p} = (0, 0, 0, P_{\hat{p}})$ and $\hat{c} = (I, -L, I, 0)$. With definitions (3.57) and (3.58), ILC then fits into the structure of Figure 3.2. Using these operators, ILC is bounded as

$$||\Pi_{P_{\hat{p}}//C_{\hat{c}}}|| \leq \|(P_{\hat{p}}, I)\|\left(\frac{||(I, P_{\hat{p}})^\top\|\|Q_{\hat{c}}L\|}{1-\sigma} + 1\right), \tag{3.59}$$

where $Q_{\hat{c}} \in \mathbb{R}^{N\times N}$ is a robust filter that is applied to the right hand side of (3.58), and the positive scalar

$$\sigma := \|Q_{\hat{c}}(I - L_{\hat{c}}P_{\hat{p}})\|. \tag{3.60}$$

The 1-norm and ∞-norm cases of the bound (3.59) were derived in [Bradley, 2010], and the proof was extended to the 2-norm case in our initial research [Zhou et al., 2025]. The full extended result is given in Appendix A. This bound $||\Pi_{P_{\hat{p}}//C_{\hat{c}}}||$ can then be used in Theorem 3.1 to yield a transparent robust stability condition for ILC. Note that for a

non-zero robust stability margin, it follows from (3.59) and (3.60) that

$$\|Q_{\hat{c}}(I - L_{\hat{c}}P_{\hat{p}})\| < 1, \tag{3.61}$$

which agrees with the standard convergence condition (3.13).

3.4 Research Problems

Over the course of fifteen years, ILC has progressed from purely elbow extension to full arm reaching tasks including hand and wrist motion via a 24 channel FES electrode array [Excell et al., 2013]. Specifically, this control approach identified a static linear mapping between each electrode pad in the array and the resulting motion. It then used this mapping to update the stimulation in order to get closer to the desired gesture. This was repeated until a sufficiently small tracking error between measured and desired gestures was achieved. [Freeman, 2014] placed a 5×8 array on the subject's forearm, a subset of array elements that covered the target muscle was selected in terms of the previous experimental input and output data, and the structure information of the prior system. A class of ILC algorithm was tested on 2 unimpaired subjects to produce pointing, pinching and open-hand gestures. Experimental results demonstrated that each ILC trial reduced the tracking error to approximately 30%, and eventually the error was less than 5 degrees after 3 trials. This approach was used clinically by [Kutlu et al., 2016b; Excell et al., 2013]. The former study placed a 4×6 array on the dorsal side of forearm, and the tracking error was reduced by an average of 50.3% after 6 trials. The latter study placed a 5×8 array on the same position, and the ILC approach reduced the mean percentage error by approximately 30% for each trial, and was less than 5 degrees after 3 trials. However, when the authors later applied the method in clinical sessions with stroke participants, time constraints meant the model was not identified accurately. This produced a much worse performance than in their earlier tests. Also, an extra model identification step was usually required after each trial to ensure the precision of the model, which took extra time, and it was not considered in these studies. Recent trials which avoided extra identification after each trial by reusing previous models yielded significantly degraded tracking accuracy [Kutlu et al., 2016a].

To solve the above deficiencies, a new control approach is needed that requires little or no model identification tests, but is capable of accurate tracking in the presence of substantial model uncertainty (e.g. fatigue, spasticity and electrode movement). ILC is an obvious starting point given its pedigree in rehabilitation, and there already exist a range of robust ILC algorithms that may be suitable for application in rehabilitation. However, closer inspection reveals these have focused on highly structured parametric [Ahn et al., 2005; Xu and Xu, 2013] or multiplicative/additive [Donkers et al., 2008; Owens et al., 2014; Freeman et al., 2009c] forms. Model predictive and simple

adaptive strategies have also been embedded into the ILC framework to address time-iteration-dependent uncertainties. Unfortunately, their accuracy is subject to modelling error [Ma et al., 2021] and relies on restrictive assumptions on the form of uncertainties [Zhang et al., 2023]. Methods that can be applied to more general uncertainties typically require substantial identification/training time, excessive tuning, or place additional structural assumptions [Lee et al., 2000; Meng and Moore, 2017; Meng, 2019]. A promising avenue are ILC approaches that update the model in order to better capture the plant dynamics. Li and Zhang [2010]; Li et al. [2014] used fuzzy neural networks to approximate multiple underlying nonlinear models and select the best one for ILC at every time sample. [Longman et al., 2011] updated the model in between ILC trials using a standard model identification approach. This focused on linear systems, and only considered inverse ILC. It also did not provide any stability or robust performance guarantees. Instead of switching between different ILC updates, [Zhu et al., 2015] specified multiple linear models to capture unknown iteration-varying parameters, and designed a single ILC update using H_∞ tools which can stabilise all specified models. Similarly, [Padmanabhan et al., 2021] captured parametric uncertainty by producing multiple linear models, and designed ILC using a convex combination of all plants. Unfortunately, there is currently no switched multiple model framework that derives robust performance bounds for the most common ILC update structure when the plant model is subject to a general class of modelling uncertainty specified by the designer. Additionally, there is no principled multiple-model guidelines allowing the designer to systematically and efficiently generate the required plant models and associated ILC updates. In terms of application, none of the above approaches has been used in FES upper limb rehabilitation.

3.5 General ILC Implementation

To address these challenges, this thesis aims to present and validate a multiple-model ILC framework, which can guarantee long-term performance during practical upper-limb FES rehabilitation tasks. To achieve this, the first step is to define a general ILC method used in this research. Taking example from [Bristow et al., 2006], the common ILC update applied with the system defined in section 3.3.3 is

$$u_2(k+1) = Q[u_2(k) - Ly_2(k)], \tag{3.62}$$

where $Q \in \mathbb{R}^{mN\times mN}$ is a robustness filter and $L \in \mathbb{R}^{mN\times nN}$ is a learning operator in terms of the lifted plant model $P_{\hat{p}}$. From section 3.3.3, signal y_2 is the measured tracking error, which, in the absence of disturbance, is $y_{ref} - y_1$.

The monotonic ILC convergence condition is

$$\sigma := \|Q(I - LP_{\hat{p}})\| < 1 \tag{3.63}$$

where $P_{\hat{p}}$ is the lifted plant defined by (3.56). If there are no disturbances, i.e. $(u_0, y_0)^\top = 0$, guarantees

$$y_1(k) \to (I - Q(I - LP_{\hat{p}}))^{-1} QLP_{\hat{p}} y_{ref} \text{ as } k \to \infty.$$

In particular, if $Q = I$, then tracking objective (3.2) holds. Note that $\|\cdot\|$ denotes the 2-norm throughout this paper.

However, the ILC update (3.62) in practical implementation may amplify errors at high frequencies due to phase lags [Elci et al., 2002], causing oscillatory or divergent behavior during convergence. Additionally, unmodeled high-frequency dynamics further destabilise the learning process, degrading performance for practical ILC implementation [Huang et al., 2014]. To address this, the Q-filter in (3.62) employs low-pass filtering strategy. However, low-pass filter causes a phase shift in the filtered signal, leading to decreased tracking performance. To address this, a zero-phase filtering strategy [Elci et al., 2002; Rotariu et al., 2008] is applied to the low-pass filter, where the signal is initially filtered in the standard forward time direction and then the same filter is applied in reverse order to restore its phase.

In implementation, a standard low-pass filter is first designed, with its order and cut-off frequency appropriately selected to reject high frequency components. This thesis utilises a 5^{th}-order 3Hz low-pass Butterworth filter, denoted by Q_f. The effectiveness of this filter Q_f for robotic upper-limb systems controlled by ILC was proved by [Elci et al., 2002], where the tracking error was reduced by a factor of 100 over 6 ILC trials in the presence of high-frequency vibration disturbances. The Q_f filter can be established in MATLAB scripts using Signal Processing Toolbox ('butter' function), and it is represented in state-space form as $f = (A_f, B_f, C_f, D_f)$. This then yields the lifted low-pass filter $Q_{\hat{f}}$ by applying the lifted transformation (3.56). Consequently, a zero-phase low-pass filter expressed as $Q = Q_{\hat{f}}^\top Q_{\hat{f}}$ can be fitted into the general ILC update (3.62), and this will be used in the subsequent section within a multiple model framework.

3.6 Summary

A variety of ILC updates have been reviewed, including the simple structure forms P-type, D-type and phase-lead ILC. These algorithms do not involve any explicit plant models in their ILC updates, and usually do not provide a satisfactory performance. More advanced methods are model based, including gradient descent, inverse, norm

optimal and Newton method based ILC. These algorithms give the best performance, however, they are not robust to model uncertainties and it usually takes a long time to identify a model, which poses a particular problem in stroke rehabilitation.

Existing ILC robustness analysis to incorporate the different types of uncertainties has been reviewed, but these approaches have focused on the specific forms of uncertainties, which limits their practical utility. A more comprehensive approach based on the gap metric has therefore been summarised. This approach will form the basis of more advanced ILC approaches in the next chapter.

Chapter 4

Multiple Model Framework of ILC

Previous practical application of ILC typically leads to long-term instabilities, caused by high frequency components building up over time. This is caused by disturbance and model uncertainty, as discussed in the previous chapter. An obvious way to address this is to update the plant models between ILC trials in order to better capture the model dynamics. This approach is a special case of multiple model adaptive control, which has been used for many years in the standard (non ILC) setting as summarised next.

Many multiple model control approaches have been proposed, including multiple model adaptive estimation [Lainiotis, 1976a] and multiple model adaptive control [Lainiotis, 1976b; Saridis and Dao, 1972] which 'blend' together state control signals from various models to form a resultant control signal. Robust multiple model adaptive control [Fekri et al., 2004a,b] is similar but uses output feedback controllers instead of state controllers. A later variation of this idea is multiple model switched adaptive control [Morse, 1996, 1997], which switches between control signals instead of blending them, and uses the observed error as the performance criterion that determines when a switch occurs. More recently, estimation based multiple model switched adaptive control (EMMSAC) was proposed [Buchstaller and French, 2016a,b], which uses optimal disturbance estimation to measure the performance of each model. It then switches in the controller corresponding to the model that best matches the measured data. Unlike previous approaches, EMMSAC has the advantage of robust stability bounds that do not scale with the number of plant models.

Multiple model frameworks have also been applied to ILC. Li and Zhang [2010] and Li et al. [2014] considered a nonlinear system with unknown time-varying parametric uncertainty that satisfied uniformly global Lipschitz conditions. Then, fuzzy neural networks were employed to approximate these unknown models and select the best one at every time sample. Strict constraints were also required on the iteration-varying

learning gain for asymptotic convergence. It was illustrated by an example that long-term instability could still occur within only a few trials. Longman et al. [2011] also applied a model update procedure using inverse ILC for linear systems, and employed identification procedures to determine the plant models used by ILC. No uncertainty constraint form was stipulated, and there was also no theoretical evidence to guarantee either robust stability or tracking performance. Unlike the previous methods, Zhu et al. [2015] specified multiple linear models with relative degree one or greater than one, in order to capture the true plant from some possible plants having unknown iteration-varying parameters that must satisfy strict restrictions. Instead of switching between different ILC updates, they designed a single ILC update using H_∞ methods which could adapt to those uncertainties. However, if the initial state varies randomly along the ILC trials, i.e. white noise, the robust convergence cannot be guaranteed. More recently, Padmanabhan et al. [2021] considered a linear time-invariant system with relative degree one and uncertainties on its system's Markov parameters. The bounds of Markov parameters were specified by the designer and hence produced multiple underlying plant models, each of these models were recursively updated at every time sample and approach to the true parameters. The ILC update was designed using a convex combination of all these underlying models at each time sample, but there was lack of theoretical evidence to show stability of the overall controller.

In summary, a variety of multiple model frameworks have been applied, but most of them only considered a restricted form of uncertainty, i.e. parametric or other structural uncertainties. There is currently no switched multiple model framework that derives robust performance bounds for the most common ILC update structure when the plant model is subject to a general class of modelling uncertainty specified by the designer. Additionally, there is no principled multiple-model guidelines allowing the designer to systematically and efficiently generate the required plant models and associated ILC updates. In terms of application, none of the above approaches has been used in FES upper limb rehabilitation.

4.1 Estimation-based Multiple Model Switched ILC

In Freeman and French [2015], EMMSAC was first applied to the ILC framework. Like its non-ILC counterpart, this produced performance bounds that did not degrade as models were added. The framework was called Estimation-based Multiple Model Switched Iterative Learning Control (EMMILC) and is now described.

The basic idea is to design a set of candidate plant models $\{P_{p_1}, P_{p_2}, P_{p_3}, ..., P_{p_{N_p}}\}$ that may represent the uncertain true plant. These are each then lifted using (3.7) to produce

the lifted candidate plant set

$$\mathcal{P} = \{P_{\hat{p}_1}, P_{\hat{p}_2}, P_{\hat{p}_3}, ..., P_{\hat{p}_{N_p}}\}.$$

An ILC design procedure $K : \mathcal{P} \rightarrow \mathcal{C}$ is then applied to each model to result in a corresponding set of ILC controllers

$$\mathcal{C} = \{C_{\hat{c}_1}, C_{\hat{c}_2}, C_{\hat{c}_3}, ..., C_{\hat{c}_{N_c}}\}.$$

As in the last chapter, $P_{\hat{p}_i}$ and $C_{\hat{c}_j}$ can be referred to simply by their state-space parameterisations $\hat{p}_i = (0, 0, 0, P_{\hat{p}_i})$ and $\hat{c}_j = (I, -L_j, I, 0)$ respectively, hence $\hat{c}_j = K(\hat{p}_i)$ denotes the controller designed for the plant $\hat{p}_i$. Note that N_c is smaller than N_p if more than one plant is associated with the same controller.

The objective of EMMILC is to ensure bounded-input bounded-output stability for any true plant $P_{p^*} \in \mathcal{U}$ by appropriately switching between controllers $C_{\hat{c}} \in \mathcal{C}$. For each trial, the selection of the appropriate ILC update is determined through a bank of Kalman estimators, which aim to establish how well each plant model fits the measured data (u_2, y_2) shown in Figure 3.2. Every estimator $E(\hat{p})$ computes a residual, denoted as $r_{\hat{p}}$, corresponding to the magnitude of the minimal external signal (u_0, y_0) depicted in Figure 3.2 that is needed to explain the observed data (u_2, y_2). Specifically, suppose $\mathcal{N}_{\hat{p}}^{[0,k]}(u_2, y_2)$ is the set of all disturbances (u_0, y_0) compatible with plant $P_{\hat{p}}$, the measured signals (u_2, y_2) and the signal connections in Figure 3.2 over ILC trials $[0, k]$. The residual on trial k is then defined as

$$r_{\hat{p}}[k] = \inf\{r \geq 0 | r = \|v_0\|, v_0 \in \mathcal{N}_{\hat{p}}^{[0,k]}(u_2, y_2)\}. \tag{4.1}$$

Since ILC trials are independent, this can be calculated recursively as

$$r_{\hat{p}}[k] = \sqrt{(r_{\hat{p}}[k-1])^2 + (r_p^k[N-1])^2}, \quad r_{\hat{p}}[0] = 0 \tag{4.2}$$

where the unlifted residual over interval $[0, t]$ on trial k is

$$r_p^k[t] = \inf\{r \geq 0 | r = \|v_0\|, v_0 \in \mathcal{N}_p^{[0,t]}(\tilde{u}_2(k, \cdot), \tilde{y}_2(k, \cdot))\}. \tag{4.3}$$

Here $\mathcal{N}_p^{[0,t]}(\tilde{u}_2(k, \cdot), \tilde{y}_2(k, \cdot))$ is the unlifted equivalent of $\mathcal{N}_{\hat{p}}^{[0,k]}(u_2, y_2)$ on trial k. It is

shown in [Willems, 2004] that (4.3) can be computed by the standard discrete-time unlifted Kalman filter using the unlifted 'along-the-trial' update

$$\begin{aligned}\tilde{x}_p(t+1/2) &= \tilde{x}_p(t) - \Sigma_p(t)C_p^\top[C_p\Sigma_p(t)C_p^\top + I]^{-1} \\ &\quad \cdot [\tilde{y}_2(k,t) + C_p\tilde{x}_p(t)] \qquad (4.4)\\ \Sigma_p(t+1/2) &= \Sigma_p(t) - \Sigma_p(t)C_p^\top[C_p\Sigma_p(t)C_p^\top + I]^{-1} \\ &\quad \cdot C_p\Sigma_p(t) \qquad (4.5)\\ \tilde{x}_p(t+1) &= A_p\tilde{x}_p(t+1/2) + B_p(\tilde{u}_2(k,t)) \qquad (4.6)\\ \Sigma_p(t+1) &= A_p\Sigma_p(t+1/2)A_p^\top + B_pB_p^\top \qquad (4.7)\end{aligned}$$

with initial conditions $\Sigma_p(0)$, $\tilde{x}_p(0)$ and sample number $t \in [0, N-1]$. The required $r_p^k[N-1]$ is then given by the weighted norm

$$r_p^k[N-1] = \left[\sum_{t=0}^{N-1} \|\tilde{y}_2(k,t) + C_p\tilde{x}_p(t)\|^2_{[C_p\Sigma_p(t)C_p^\top+I]^{-1}}\right]^{\frac{1}{2}}. \qquad (4.8)$$

Computations (4.2), (4.4)-(4.8) require significantly less computational effort compared to solving (4.1) because they do not involve large matrices. The ILC update corresponding to the candidate plant with the smallest residual is then used to compute the next trial's control input. The switching signal is therefore defined by

$$q(k) := \arg\min_{p\in\mathcal{P}} r_{\hat{p}}[k] \quad \forall k \in \mathbb{N} \qquad (4.9)$$

with corresponding ILC operator $C_{K(q(k))}$. The overall EMMILC framework is illustrated by Figure 4.1.

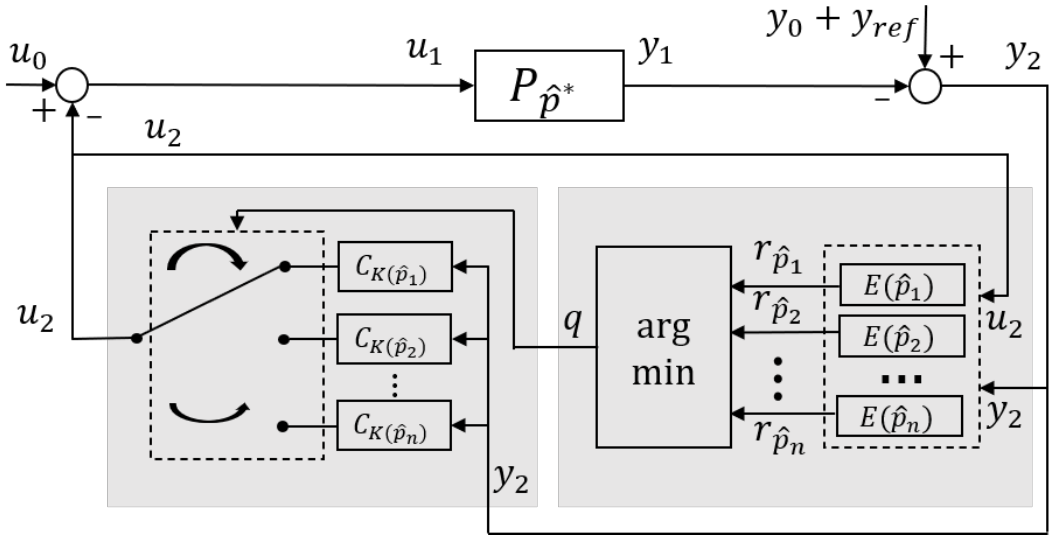

FIGURE 4.1: EMMILC framework: the bank of estimators $E(\cdot)$ defined by (4.2), (4.4)-(4.8) outputs the residuals $r_{\hat{p}_1}$ to $r_{\hat{p}_n}$, the minimum residual is used to produce the switching signal q, which then selects the next ILC update to apply to true plant P_{p^*}.

The conditions for stability when EMMILC is applied to an unknown true plant $P_{\hat{p}^*}$ belonging to an uncertainty space $\mathcal{U}$ were derived in Freeman and French [2015] and consist of two criteria and bounds on the internal signals. These are now outlined in a simple manner, facilitating the following development of an effective design framework.

Consider that the true plant $P_{p^*} \in \mathcal{U}$. Let $\mathcal{P}$ denote a set of candidate plant models taking the state space form (3.3), and let $\mathcal{C}$ represent a set of corresponding ILC controllers constructed using (3.58) such that the condition in (3.61) is satisfied. The EMMILC approach defined by (4.2), (4.4)-(4.9) ensures the stabilisation of the true plant P_{p^*} on the condition that the following two requirements are fulfilled:

$$1) \qquad \exists \hat{p} \in \mathcal{P}, \quad s.t. \quad \delta(\hat{p}, \hat{p}_*) < \rho(\mathcal{P}, \mathcal{C}, \mathcal{U}), \tag{4.10}$$

where δ is the gap metric and ρ is a function involving controller set $\mathcal{C}$, plant set $\mathcal{P}$ and uncertainty space $\mathcal{U}$. Since the true plant $\hat{p}^*$ is unknown, this criterion specifies a minimum gap distance between models covering the uncertainty space. The second criterion is

$$2) \qquad \exists \hat{c} \in \mathcal{C}, \quad s.t. \quad \|\Pi_{\hat{p}//\hat{c}}\| < \infty \quad \forall \hat{p} \in \mathcal{U}, \tag{4.11}$$

which means there must exist a stabilising controller for every plant in the uncertainty space. Criteria (4.10) and (4.11) are illustrated by Figures 4.2a and 4.2b, respectively.

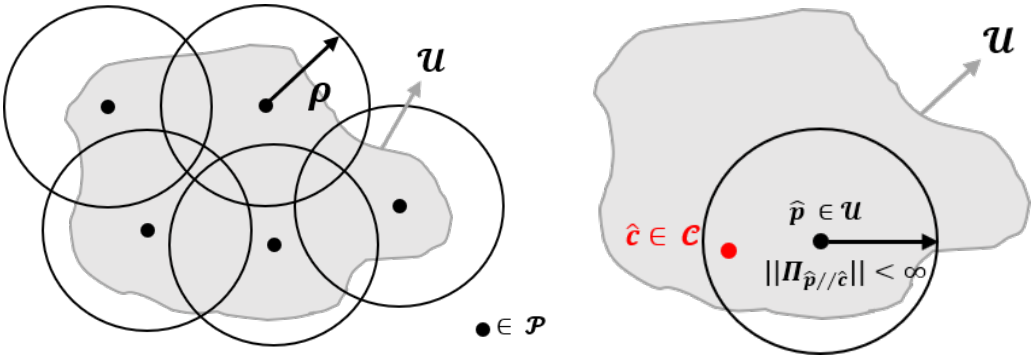

(A) Criterion (4.10): uncertainty set $\mathcal{U}$ is covered by balls with radius ρ.

(B) Criterion (4.11): circle is set of $\hat{p} \in U$ such that $\|\Pi_{\hat{p}//\hat{c}}\| < \infty$.

FIGURE 4.2: Illustration of criteria (4.10) and (4.11).

If the above conditions are satisfied, the controller signals of the switched closed-loop system $[P_{\hat{p}^*}, C_{K(q)}]$ are guaranteed to be bounded with respect to their ideal values as

$$\|(u_2, y_2)^\top\|_{(-P_{\hat{p}^*}^{-1}, 0)^\top} < \eta(\mathcal{P}, \mathcal{C}, \mathcal{U}) \|(u_0, y_0)^\top\|, \tag{4.12}$$

where observed signal (u_2, y_2), external disturbances (u_0, y_0) are defined in Figure 3.2, and η is a positive scalar function defined in [Freeman and French, 2015]. This is a

simplified restatement of [Freeman and French, 2015] which contains the full computation of functions ρ and η. Note that EMMILC is an extension of the MMAC framework developed in [Buchstaller and French, 2016a] for feedback stabilisation.

Unfortunately, $\rho(\mathcal{P},\mathcal{C},\mathcal{U})$ has a large computational burden, and the results are also conservative (i.e. more candidate plants are specified than required). To address this, the next section proposes a simplified approach that could be used for practical design.

4.2 Multiple Model Design Procedure

This section presents a novel design procedure, marking a significant contribution of this research. Firstly it does not require calculating $\rho(\mathcal{P},\mathcal{C},\mathcal{U})$, which greatly simplifies the approach. Secondly, it minimises the number of candidate models, and therefore the computational burden and memory resources. This is critical in practice since EMMILC will be implemented on a microcontroller, which has limited computational resources. In rehabilitation the eventual goal is to embed the controller within a highly portable, or even wearable, system. Therefore memory and computation reduction is even more pressing.

Firstly, criterion (4.11) requires all plants in the uncertainty set $\mathcal{U}$ to be stabilised. The obvious approach to satisfy this is using Theorem 3.1 and selecting a **minimal** candidate plant set $\mathcal{P}$ such that the union of 'gap balls' (see Figure 4.2a) includes the set $\mathcal{U}$. This is expressed by first defining a gap ball centred on $\hat{p} \in \mathcal{P}$ as

$$B(\hat{p},K,\gamma) := \{\hat{p}\} \cup \{\hat{p}_1 \in \mathcal{P}_{LTI} \mid \delta(\hat{p},\hat{p}_1) < \gamma||\Pi_{\hat{p}//K(\hat{p})}||^{-1}\} \cap \mathcal{U}, \quad \hat{p} \in \mathcal{P}, \tag{4.13}$$

and then requiring

$$\mathcal{U} \subset \mathcal{R}, \quad \textit{where} \quad \mathcal{R} := \cup_{\hat{p}\in\mathcal{U}} B(\hat{p},K,\gamma), \tag{4.14}$$

where γ can be taken as 1, and $\mathcal{P}_{LTI}$ is the set of all LTI SISO plants.

However, criterion (4.10) may not be satisfied. Therefore, the tuning parameter $0 < \gamma \leq 1$ is employed within (4.13) to reduce the radius of the gap balls. As $\gamma \to 0$, (4.10) will always be satisfied for any ρ, avoiding the need to explicitly calculate it.

To compute the minimal candidate plant set $\mathcal{P}$ that satisfies (4.13) and (4.14), the approach is to define a set of many (more than needed) plant models, $\mathcal{H} = \{P_{\hat{p}_1}, P_{\hat{p}_2}, ..., P_{\hat{p}_{N_m}}\}$, that are uniformly distributed in the uncertainty space $\mathcal{U}$, then remove those plants that are not needed since they lie within an existing gap ball. When all unnecessary models are removed, we hence obtain the minimum set $\mathcal{P}$. The overall approach to achieve this is stated in Algorithm 1.

Algorithm 1 Procedure to generate the minimal candidate plant set $\mathcal{P}$

Input: ILC design procedure K, and $0 < \gamma \leq 1$

Output: Minimal candidate plant set $\mathcal{P}$

```
Define H = {P_{p̂_1}, P_{p̂_2}, ..., P_{p̂_{N_m}}} as the finest grid that computational resources allow;
Set S = {0, 0, ..., 0} with N_m elements, S_j denoting the j^th element;
for each i ∈ {1, 2, 3, ..., N_m} do
  for each j ∈ {1, 2, 3, ..., N_m} do
    if ∃a ∈ {1, 2, 3, ..., N_m}, s.t. S_a = 0 then
      Design Q_{ĉ_i}, L_{ĉ_i} for ĉ_i = K(p_i) to reach a compromise between minimising (3.59)
      and (3.61).
      if δ(p̂_i, p̂_j) < γ||Π_{p̂_i//K(p̂_i)}||^{-1} then
        S_j = i;
      end if
    else
      Delete repetitions from S, set N_p = |S|;
      P = {P_{p̂_{S_1}}, P_{p̂_{S_2}}, P_{p̂_{S_3}}, ..., P_{p̂_{S_{N_p}}}}; Exit loops;
    end if
  end for
end for
Return P.
```

The resulting ILC controller set is then $\mathcal{C} = \{C_{K(\hat{p}_1)}, C_{K(\hat{p}_2)}, C_{K(\hat{p}_3)}, ..., C_{K(\hat{p}_{S_{N_p}})}\}$. This is illustrated in Figure 4.3.

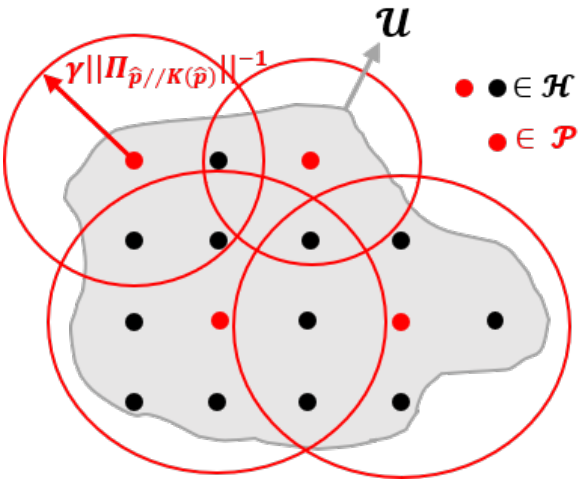

FIGURE 4.3: Illustration of Algorithm 1, the 'black' plant models are not needed and removed from the initial plant set $\mathcal{H}$. The left 'red' plants form the minimal candidate plant set $\mathcal{P}$, which still covers the uncertainty space $\mathcal{U}$.

4.3 Summary

This chapter has reviewed existing multiple model control frameworks, which address stability and performance issues caused by model uncertainties within the standard ILC framework. However, most lack theoretical robust performance guarantees, or a principled design procedure. An exception is the EMMILC approach introduced in Freeman and French [2015] which applies EMMSAC to the ILC framework. A promising design procedure has been developed to design the candidate plant set in order to satisfy the stability conditions of EMMILC. This procedure requires the designer to choose only one variable (γ) that transparently trades computational load with performance whilst satisfying criteria (4.10) and (4.11). It is then implemented in an algorithmic form (Algorithm 1). This design procedure will be tested using a realistic rehabilitation case study in the next chapter.

Chapter 5

Numerical Evaluation on Wrist Model

Chapter 2 highlighted the limitations of current ILC applications to FES-based stroke rehabilitation. To address these, EMMILC with the design procedure developed in Chapter 4 will be implemented on the key problem of wrist extension, and the resulting performance will be compared with conventional ILC design.

5.1 Wrist model

Wrist dynamics are a critical component of functional movement, and are incorporated in most advanced FES rehabilitation systems. They take the form of FES activated muscle actuating the rigid body dynamics (RBD) of the wrist and hand. The former is most commonly represented by a Hammerstein structure, comprising an isometric recruitment curve (IRC) and linear activation dynamics (LAD) [Le et al., 2010; Peaden and Charles, 2014]. The overall model is shown in Figure 5.1.

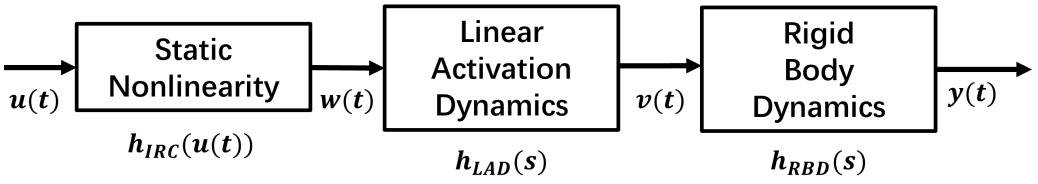

FIGURE 5.1: Hammerstein structure $H(s)$ with $u(t)$ equal to the stimulation level, $v(t)$ the muscle output torque and the wrist angle $y(t)$.

The isometric recruitment curve is often approximated by a static gain, h_{IRC}, in which case the overall model adopts the general form

$$H(s) = h_{IRC} \cdot \frac{\omega_n^2}{s^2 + 2\omega_n s + \omega_n^2} \cdot \frac{1}{I_s s^2 + B_s s + K_s}. \tag{5.1}$$

This plant (5.1) can readily be placed in the state-space form (3.48), and thereby expressed as the unlifted plant P_p, with $p = (A_p, B_p, C_p, D_p)$. It can then be transformed into its equivalent lifted form

$$P_{\hat{p}} = \begin{bmatrix} D_p & 0 & \cdots & 0 & 0 & 0 \\ C_pB_p & D_p & \cdots & 0 & 0 & 0 \\ C_pA_pB_p & C_pB_p & \cdots & 0 & 0 & 0 \\ \vdots & \vdots & \ddots & \vdots & \vdots & \vdots \\ C_pA_p^{N-2}B_p & C_pA_p^{N-3}B_p & \cdots & C_pB_p & D_p & 0 \\ C_pA_p^{N-1}B_p & C_pA_p^{N-2}B_p & \cdots & C_pA_PB_p & C_pB_p & D_p \end{bmatrix}. \tag{5.2}$$

This lifted plant $P_{\hat{p}}$ then embeds the ILC plant dynamics

$$y_1(k) = P_{\hat{p}}u_1(k), \tag{5.3}$$

which fits into the closed-loop structure of Figure 3.2, and can be applied within Theorem 3.1 to yield robust performance bounds.

In practice, parameters within the model (5.1) are often subject to uncertainties, which result from individual difference, or physiological variations (e.g.,muscle fatigue/spasticity). To evaluate the system, practical parameter values are summarised from the tests performed by previous studies. Nominal parameter values from Charles and Hogan [2012], Charles and Hogan [2011], Peaden and Charles [2014] and Park et al. [2017] are listed in Table 5.1. Stiffness and inertia typically vary most between individuals, and their ranges are also given.

TABLE 5.1: Values of wrist parameters.

Parameter	Symbol	Nominal value	Uncertainty range	Unit
IRC constant	h_{IRC}	0.0117	N/A	N/A
Natural frequency	ω_n	9.4248	N/A	rads/s
Stiffness	K_s	1.62	$0.62 \sim 3.24$	Nm/rad
Damping	B_s	0.128	N/A	Nms/rad
Inertia	I_s	0.0045	$0.0007 \sim 0.00612$	Nms^2/rad

The aim is to control the FES applied to wrist system (5.1) such that the output tracks a desired movement profile as accurately as possible. However, its dynamics will be subject to the variation in parameters defined in Table 5.1.

5.2 Numerical Settings and Controller Design

The controller design in this section is implemented using MATLAB R2023a scripts, specifically employing the control system toolbox and the signal processing toolbox.

The system operates in discrete-time with a sampling frequency of 40 Hz. A fixed-step solver with automatic selection is employed, with the fixed-step size set to the system sampling period $T_s = 0.025$ seconds, consistent with existing clinical implementations. The control objective is to achieve accurate tracking of a predefined wrist flexion-extension trajectory, which simulates tasks involving functional grasp and release, with a total length of $T = 6$ seconds. This reference trajectory is illustrated by Figure 5.2. The model uncertainty set $\mathcal{U}$ comprises the parametric uncertainty ranges defined in Table 5.1.

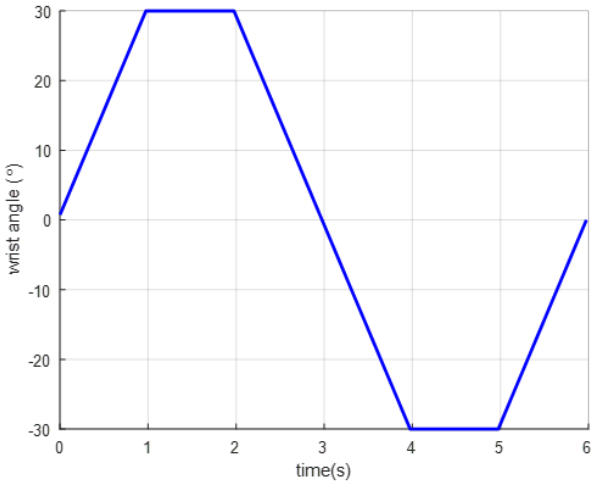

FIGURE 5.2: The reference trajectory that simulates the wrist flexion (positive half) and the extension (negative half) movements.

The inverse ILC update (3.27) with step size $\beta = 1$ is employed due to its rapid convergence. A 10^{th} order zero-phase low-pass filter Q with cut-off frequency $5Hz$ is selected to provide robustness against high frequency noise and disturbances. The control design procedure $C_{\hat{c}}$, $\hat{c} = K(\hat{p})$ is hence given by

$$u_2(k+1) = Q[u_2(k) - P_{\hat{p}}^{-1} y_2(k)], \quad \forall P_{\hat{p}} \in \mathcal{H}. \tag{5.4}$$

To design the candidate model set, Algorithm 1 is now implemented using tuning parameter $\gamma = 1$. This is chosen to establish whether a minimum plant model set can provide satisfactory performance. Within Algorithm 1, $N_m = 100$ is selected as the size of the initial plant set since it takes about one hour to compute the minimum plant set, which is deemed acceptable for each implementation.

The output of Algorithm 1 is a minimal candidate plant set $\mathcal{P} = \{P_{\hat{p}_1}, P_{\hat{p}_2}, ..., P_{\hat{p}_{N_p}}\}$ comprising $N_p = 34$ plants (66 having been removed). The corresponding candidate controller set $\mathcal{C} = \{C_{\hat{c}_1}, C_{\hat{c}_2}, C_{\hat{c}_3}, ..., C_{\hat{c}_{N_p}}\}$ also contains 34 ILC controllers.

5.3 Evaluation of Tracking Performance

Having controller set designed, EMMILC will be compared to standard ILC, with the latter designed using the nominal model. This will be implemented using Simulink script also in MATLAB R2023a. The configuration of the solver is consistent with the setup described in the previous section. According to Table 5.1, the nominal plant $P_{\hat{p}^f}$ has parameters $K_s = 1.62$, $I_s = 0.0045$, $B_s = 0.1280$, $h_{IRC} = 0.0117$ and $\omega_n = 9.4248$. In contrast, the true plant $P_{\hat{p}^*}$ has an identical set of parameters, with the exception that $K_s = 3.24$. The true values of K_s are chosen from the uncertainty range in Table 5.1, in order to approximately model a fatigued wrist (double the nominal stiffness). This aims to simulate and evaluate the control algorithms on a realistic case. This true plant is not one of those in the set $\mathcal{P}$, which means the perfect estimation of the true plant is impossible. To replicate experimental conditions, the external disturbances (u_0, y_0) in Figure 3.2 are chosen as white noise with a signal-to-noise ratio of 10% (one tenth of the reference signal).

First the nominal model $P_{\hat{p}^f}$ is applied with white noise (u_0, y_0), and a fixed controller $C_{K(\hat{p}^f)}$ designed using the nominal model $P_{\hat{p}^f}$. After 20 ILC trials, the baseline tracking performance is shown in Figure 5.3 a). As a comparison, the standard ILC controller $C_{K(\hat{p}^f)}$ is then applied with the fatigued true plant $P_{\hat{p}^*}$. After 20 ILC trials, the true performance is shown in Figure 5.3 b).

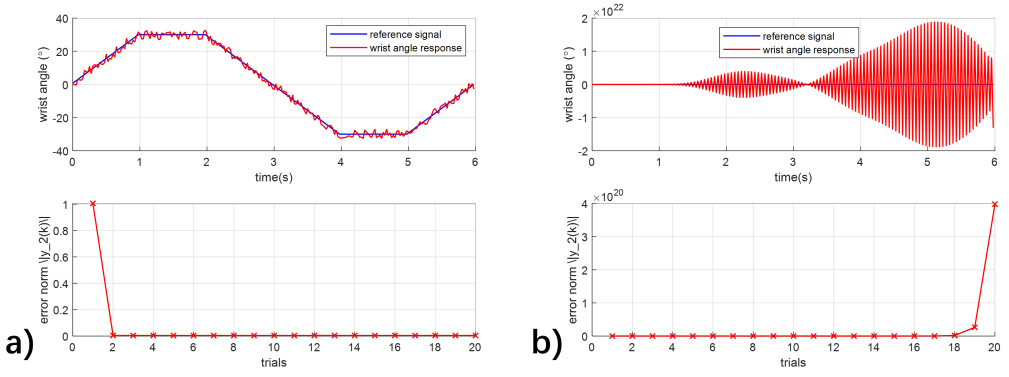

FIGURE 5.3: The tracking plots of the standard ILC over 20 trials with closed-loop systems a): $[P_{\hat{p}^f}, C_{K(\hat{p}^f)}]$ showing baseline performance and b): $[P_{\hat{p}^*}, C_{K(\hat{p}^f)}]$ showing reduced performance.

Compared to the baseline performance shown in Figure 5.3 a), Figure 5.3 b) shows error norm rapidly diverges, and inspection of closed-loop poles confirms that convergence conditions (3.12) and (3.13) are not satisfied, so that the tracking error does not properly converge with the fatigued true model $P_{\hat{p}^*}$. Due to the limitation of control signals, this diverging result is unachievable in practice. This motivates the application of EMMILC also with the white noise (u_0, y_0) added. The final tracking performance of EMMILC is shown by Figure 5.4.

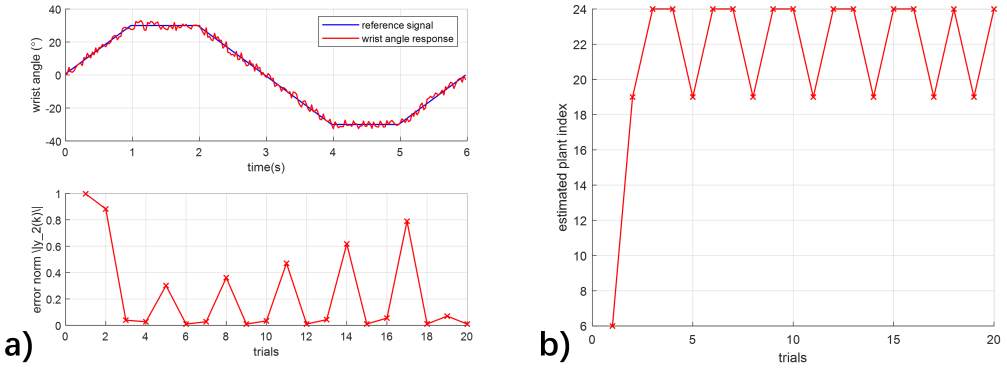

FIGURE 5.4: Tracking plots of EMMILC including a): tracking performance at trial 20 with $\gamma = 1$, and error norm $\|y_2(k)\|$ convergence for each ILC trial. b): EMMILC switching signal for each ILC trial.

Figure 5.4 a) shows the error norm slowly diverges also for EMMILC with $\gamma = 1$, and inspection of closed-loop poles confirms that convergence conditions (3.12) and (3.13) are not satisfied, so that the system is also unstable. This is because the switching signal (see Figure 5.4 b)) estimates the true plant $P_{\hat{p}^*}$ as either $P_{\hat{p}_{19}}$ or $P_{\hat{p}_{24}}$ and cannot make a decision for the remainder of the trials, but inspection of parameter values shows that both $P_{\hat{p}_{19}}$ and $P_{\hat{p}_{24}}$ are different from the true plant $P_{\hat{p}^*}$, hence the switched controller leads to another instability issue. This means the criterion (4.10) is not satisfied, and the minimum plant model set produced with $\gamma = 1$ cannot provide satisfactory performance.

To achieve satisfactory performance, the solution is to reduce the value of γ which hence increases the number of candidate plants N_p. There will always exist a value of γ that provides a stable closed loop system, as explained in Section 4.2. To measure the improvement in performance, an index E is introduced by accumulating the magnitude of tracking errors for all 20 trials. This is given by

$$E = \sum_{k=1}^{20} \|y_2(k)\|. \tag{5.5}$$

Different values of γ were tested, with corresponding performances measured using (5.5). The results are shown in Table 5.2. Similar to the result with $\gamma = 1$ shown in Figure 5.4, the tracking plots and switching signals for $\gamma = 0.5$, $\gamma = 0.25$, and $\gamma = 0.125$ are shown in Figure 5.5, 5.6, and 5.7 respectively.

As shown in Figure 5.5 a), the system designed using $\gamma = 0.5$ is stable but the performance is still poor due to multiple error spikes. The switching signal shown in Figure 5.5 b) indicates that the estimated true plant is most probably $P_{\hat{p}_{40}}$, although there remains a minor likelihood of it being $P_{\hat{p}_{33}}$. With $\gamma = 0.5$, the candidate plant set with $N_p = 64$ still yields suboptimal performance due to the restricted number of candidate

TABLE 5.2: Results comparing performance of EMMILC for different γ values.

γ in equ. (4.13)	Value of E	N_p	Convergence?
$\gamma = 1$	4.7743	36	No
$\gamma = 0.5$	4.4495	64	Yes
$\gamma = 0.25$	3.4927	81	Yes
$\gamma = 0.125$	2.4309	100	Yes

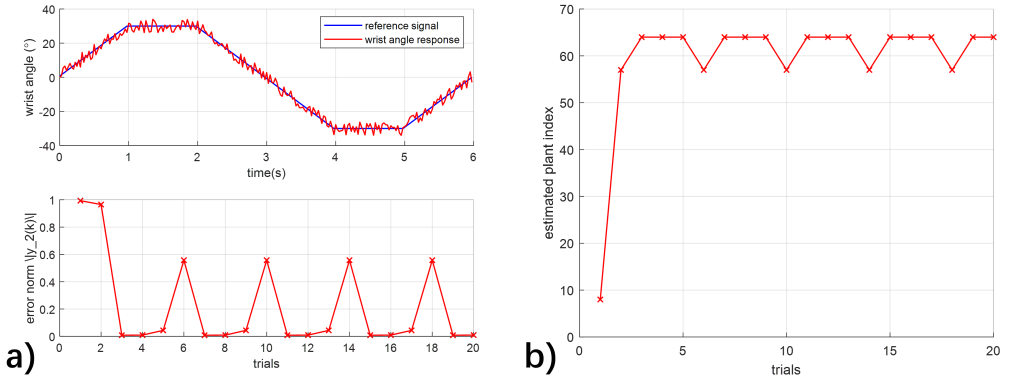

FIGURE 5.5: Tracking plots of EMMILC including a): tracking performance at trial 20 with $\gamma = 0.5$, and error norm $\|y_2(k)\|$ convergence for each ILC trial. b): EMMILC switching signal for each ILC trial.

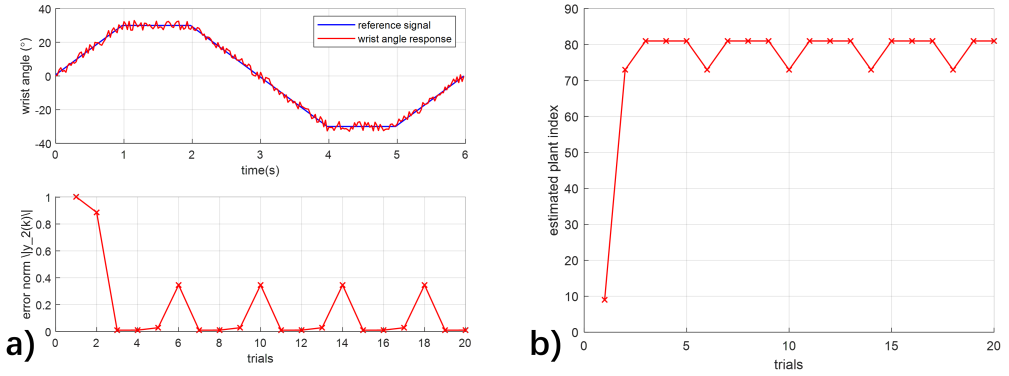

FIGURE 5.6: Tracking plots of EMMILC including a): tracking performance at trial 20 with $\gamma = 0.25$, and error norm $\|y_2(k)\|$ convergence for each ILC trial. b): EMMILC switching signal for each ILC trial.

plant models, none of which can accurately represent the true plant. Then, when γ is reduced to 0.25, the estimated plant is most likely to be $P_{\hat{p}_{80}}$, but it still has a chance to be $P_{\hat{p}_{73}}$. Inspection of parameters shows the plant $P_{\hat{p}_{80}}$ is very close to the nominal model. Hence the criterion (4.10) is satisfied by implementing the candidate plant set with $N_p = 81$, which effectively improves the tracking performance. Then further increasing the number of plants until $N_p = 100$ does not improve the performance E significantly compared with $N_p = 81$. This is because the estimated plant is $P_{\hat{p}_{100}}$, whose parameters are very close to $P_{\hat{p}_{80}}$. Although the true estimated plant models

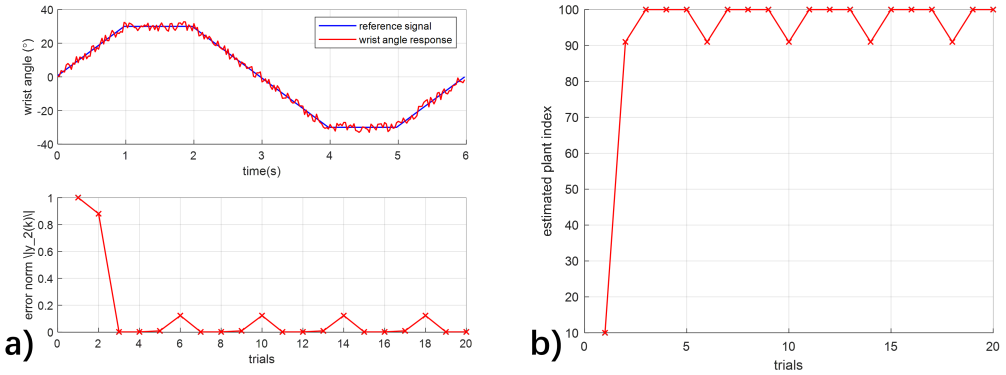

FIGURE 5.7: Tracking plots of EMMILC including a): tracking performance at trial 20 with $\gamma = 0.125$, and error norm $\|y_2(k)\|$ convergence for each ILC trial. b): EMMILC switching signal for each ILC trial.

are very similar, the measured performance E provided in Table 5.2 demonstrates an improvement when incorporating more candidate plant models.

5.4 Summary

This chapter has implemented the EMMILC approach on a realistic wrist model and uncertainty set. A comparison between conventional ILC and EMMILC illustrated the robustness of the latter. Different values of γ have been tested, and it has been demonstrated that including more controllers provides greater robust performance. However, the uncertainty was limited to two wrist parameters. In practice the performance could also be affected by other parameters, i.e. misalignment of electrodes and muscle fatigue/spasticity, hence practical experiments are needed to further evaluate the approach. In this case the plant model set should be expanded to capture more possible uncertainties that will occur during experiments.

Chapter 6

Experimental Evaluation

The previous simulations have demonstrated the effectiveness of EMMILC when applied to a simple linear wrist model. Evaluation will be further extended in this chapter by applying EMMILC experimentally to the human wrist using FES applied using single-pad electrodes. This functional movement task has been selected as it is a fundamental component of FES-based upper limb stroke rehabilitation. As in Chapter 5, conventional ILC will also be compared with EMMILC to evaluate the effectiveness of the multiple-model framework.

6.1 System Description

In order to evaluate EMMILC, tests will be conducted using a validated instrumented wrist rig which has been used in clinical trials to assess impairment in stroke. This is described in Turk et al. [2008] and is shown in Figure 6.1. The wrist rig supports the arm and restricts movement to only the horizontal plane.

FIGURE 6.1: Experimental set-up (permission received from Turk et al. [2008]).

6.1.1 Hardware Components

A potentiometer at the hinge joint under the wrist stand measures the wrist angle with a maximum range from -90° to 90°. The potentiometer can be calibrated prior to each test session by setting the extended wrist stand at specified angles marked on the rig [Turk et al., 2008]. This involves setting the extended lever to user-specified angles θ_1 and θ_2, and recording the corresponding analog voltages V_1 and V_2, respectively. The variation in angle with respect to each volt can be calculated as

$$\Delta_\theta = \frac{\theta_2 - \theta_1}{V_2 - V_1}, \tag{6.1}$$

which then gives the wrist angle $\theta(t)$ by recording the voltage $V(t)$ at any time t

$$\theta(t) = \Delta_\theta V(t), \tag{6.2}$$

with validation confirmed that the systematic error the potentiometer amounts to $\pm 2^\circ$.

The software is first programmed using Simulink toolbox and subsequently deployed onto a Raspberry Pi 4B board (Raspberry Pi Foundation, UK). This low-cost portable hardware is aligned with the intention that the ultimate system be deployable in the user's own home. The Raspberry Pi board reads the real-time wrist angles $\theta(t)$ in Simulink from the rig seat via a SPI master transfer block contained in the Simulink Support Package for Raspberry Pi Hardware, enabling precise data timing through a dedicated clock input. This is critical for accurately measuring wrist angles in real-time, ensuring a high level of data integrity. However, the Raspberry Pi board only has digital I/O ports, which cannot directly read the analog data produced by the rig seat. To tackle this issue, an analogue-to-digital converter (ADC) is required, facilitating efficient data transmission between the rig seat and the Raspberry Pi board. The 'mcp3008' ADC module (Microchip) is selected for its SPI communication compatibility and operational voltage range between $2.7V$ and $5.5V$, allowing it to be powered directly by the Raspberry Pi board [MathWorks, 2023].

The Raspberry Pi board then generates two $40Hz$ pulse-width modulated (PWM) square wave signals. Signals u_{fcr} and u_{ecr} denote the pulsewidth of these pulse trains, which both have a maximum value of 300μs. These are sent to a commercial stimulator unit (Odstock Medical Limited, Salisbury, UK) which amplifies them to generate the FES pulses, with stimulation currents ranging from 0 to $115mA$. The sampling frequency in all tests is $40Hz$. The control system was also programmed using the Matlab/Simulink toolbox for Raspberry Pi and deployed onto the Raspberry Pi hardware using external mode. The system components are shown in Figure 6.2.

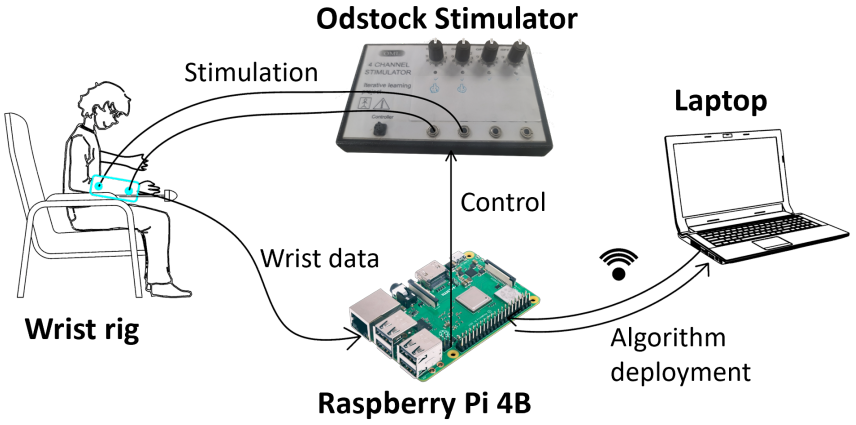

FIGURE 6.2: Upper-limb FES system components

6.1.2 Model Structure

The objective is to stimulate wrist flexion and extension so that the wrist angle follows a desired trajectory. Bi-directional wrist movement is achieved via stimulation of the Flexor Carpi Radialis (FCR) and Extensor Carpi Radialis (ECR) muscles. Each muscle can be modelled as a Hammerstein structure, comprising a static non-linearity in series with linear activation dynamics, as was shown in Figure 5.1. However, unlike in the previous chapter, here the static non-linearity will not be approximated by a scalar gain as was done to produce linear model (5.1). Instead, the nonlinear functions are included to produce the structure shown in Figure 6.3, in which $h_{IRC,fcr}(\cdot)$ and $h_{IRC,ecr}(\cdot)$ are the IRC components for the FCR and ECR muscles respectively. In addition, $h_{LAD,fcr}(s)$ and $h_{LAD,ecr}(s)$ denote the LAD components for the FCR and ECR muscles respectively.

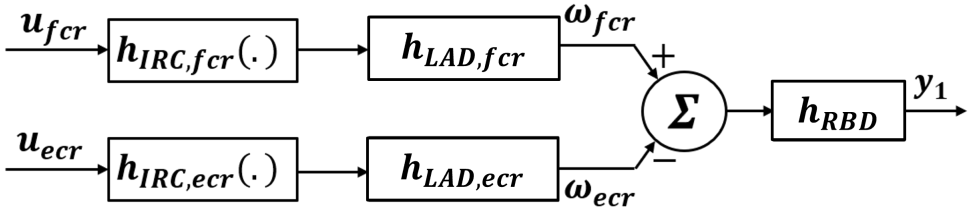

FIGURE 6.3: Wrist model excited by stimulation inputs u_{fcr} and u_{ecr} to wrist flexor and extensor muscles respectively, with output torques ω_{fcr} and ω_{ecr}. Signal y_1 is the angular response.

To produce a single input system, a static function is added to split the control signal $u_1(t)$ between the two muscles. This strategy is known as co-activation, and is widely used in FES-based upper-limb studies [Copur et al., 2016; Bó et al., 2016; Klauer et al., 2019]. The signal computed for the FCR muscle is denoted u_{fcr} and the signal for the ECR muscle is denoted u_{ecr}. Each has a maximum value of $300\mu s$. The co-activation

function takes the following form

$$u_{fcr}(t) = \begin{cases} u_1(t) + u_{c,fcr}, & 0 \leq u_1(t) \leq 300 - u_{c,fcr} \\ u_{c,fcr}, & u_{c,ecr} - 300 \leq u_1(t) < 0 \end{cases} \tag{6.3}$$

$$u_{ecr}(t) = \begin{cases} u_{c,ecr}, & 0 \leq u_1(t) \leq 300 - u_{c,fcr} \\ u_{c,ecr} - K_e u_1(t), & u_{c,ecr} - 300 \leq u_1(t) < 0 \end{cases} \tag{6.4}$$

where $u_{c,fcr}, u_{c,ecr} \geq 0$ are the co-activation levels selected during calibration. In general, the co-activation level should be minimised to avoid impeding movements and expediting the occurrence of fatigue [Zhang et al., 2020]. In addition, it reduces the operational range of $u_1(t)$ and the range of the angular response. The co-activation function is illustrated by Figure 6.4 a).

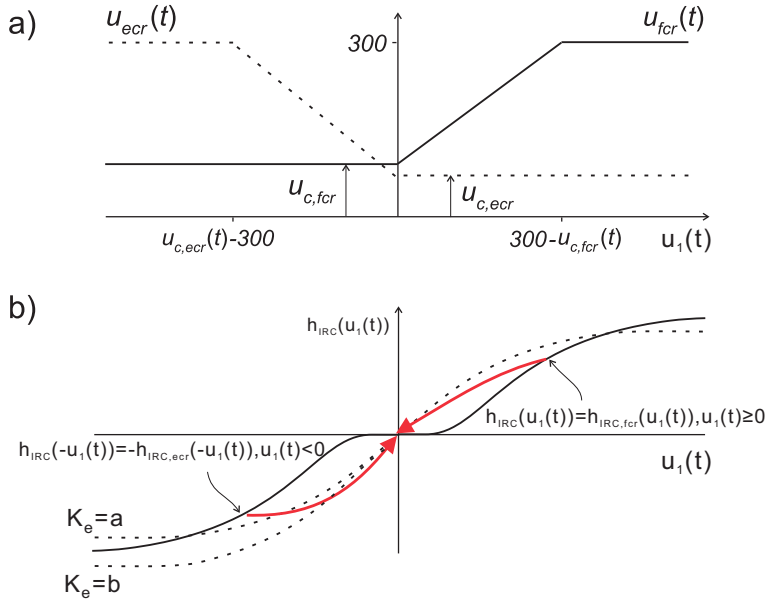

FIGURE 6.4: Linearisation of dynamics h_{IRC} shown by a): Co-activation levels $u_{c,fcr}, u_{c,ecr}$ that are properly selected to remove dead-zone in each IRC. b): $h_{IRC,fcr}$ and $h_{IRC,ecr}$ without co-activation [solid line] and with co-activation [dashed line].

Scalar $K_e > 0$ is used to scale the input applied to one of the muscles for the purpose of equalising their response. The co-activation function enables the two IRC functions to be combined into a single composite function given by

$$h_{IRC}(u_1(t)) : \begin{cases} h_{IRC,fcr}(u_1(t) + u_{c,fcr}) - h_{IRC,ecr}(u_{c,ecr}), & 0 \leq u_1 < 300 - u_{c,fcr} \\ h_{IRC,fcr}(u_{c,fcr}) - h_{IRC,ecr}(u_{c,ecr} - K_e u_1(t)), & u_{c,ecr} - 300 \leq u_1 < 0 \end{cases} \tag{6.5}$$

For $h_{IRC}(u_1(t))$ to produce zero output when $u_1(t) = 0$, it is clearly necessary to choose $u_{c,fcr}$, $u_{c,ecr}$ such that $h_{IRC,fcr}(u_{c,fcr}) = h_{IRC,ecr}(u_{c,ecr})$. The response is shown in Figure 6.4 b), where the solid line represents the case of zero co-activation ($u_{c,fcr} = u_{c,ecr} = 0$), and therefore corresponds to the two original IRC functions ($h_{IRC,fcr}$ and $h_{IRC,ecr}$). The dotted line shows the responses after co-activation ($u_{c,fcr} > 0$, $u_{c,ecr} > 0$) is applied. It is

clear that the original functions are translated so that the points $(u_{c,fcr}, h_{IRC,fcr}(u_{c,fcr}))$ and $(u_{c,ecr}, h_{IRC,ecr}(u_{e,fcr}))$ now lie at the origin. This translation is illustrated by the red arrows in Figure 6.4 b). The overall effect is to remove the dead-zone in the IRC forms.

If co-activation is applied such that the slopes of the two functions are similar, then the overall response $h_{IRC}(u_1(t))$ can be approximated by a straight line in a region about the origin. Therefore, the static nonlinearity $h_{IRC}(u_1(t))$ can be approximated by a static gain h_{IRC} in the Hammerstein structure (5.1), which significantly simplifies the model representation. This approximation is valid within the linearised region introduced by proper co-activation, as shown by the dashed line before saturation in Figure 6.4 b). This scaling can be accomplished by selecting a set-point $u_1(t) = \bar{u}_1$ and setting K_e to satisfy

$$h_{IRC,fcr}(\bar{u}_1 + u_{c,fcr}) = h_{IRC,ecr}(K_e\bar{u}_1 + u_{c,ecr}) \tag{6.6}$$

Two values of K_e are illustrated in Figure 6.4(b) to show how this scales the ECR component of $h_{IRC}(u_1(t))$.

In Copur et al. [2016]; Freeman et al. [2015] it was assumed that the LAD dynamics are identical, $h_{LAD,fcr}(s) = h_{LAD,ecr}(s) = h_{LAD}(s)$, in which case the system can be expressed in the Hammerstein form shown in Figure 6.5. If the co-activation and scal-

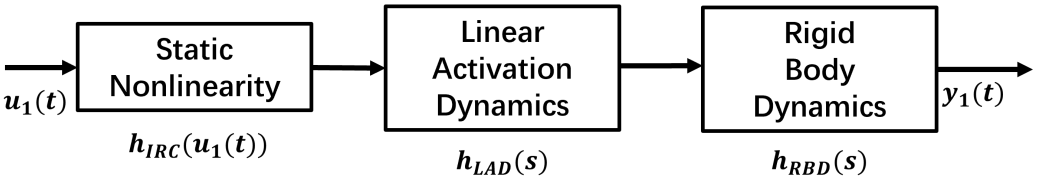

FIGURE 6.5: Hammerstein structure with isometric recruitment curve $h_{IRC}(u_1(t))$, linear active dynamics $h_{LAD}(s)$ and rigid body dynamics $h_{RBD}(s)$.

ing approaches described above are applied, $h_{IRC}(u_1(t))$ can then be approximated by a scalar gain, h_{IRC}. The overall model form can be represented by the operator $P_p : u_1 \mapsto y_1$, where

$$Y_1(s) = h_{IRC} \underbrace{\frac{1}{I_s s^2 + B_s s + K_s}}_{h_{RBD}(s)} \underbrace{\frac{\omega_n^2}{s^2 + 2\omega_n s + \omega_n^2}}_{h_{LAD}(s)} U_1(s), \tag{6.7}$$

where $Y_1(s)$, $U_1(s)$ are the respective Laplace transforms of the signals y_1 and u_1. This matches the model form (5.1).

6.2 Test Procedure

Ethics approval was granted by the University of Southampton Ethics and Research Governance Online (ERGO), ID 57751. Participants are required to be healthy and

unimpaired to avoid adding confounding factors to the experiment. To avoid interference from stimulation, they must not be attached to any electronic equipment such as a pacemaker. The tracking tasks also require participants to not have any cognitive or visual disorders. Results will be presented from a single participant (25 years old, male). Note that testing is extended to more participants in Section 6.5.

The subjects sat upright and placed their right forearm on the support as shown in Figure 6.1. Using standard guidelines [Freriks et al., 1999], two Pals PLUS ($5 \times 5cm$) surface electrodes were placed on the forearm to stimulate the FCR and ECR muscles. The amplitude of the FES stimulation was first set by applying stimulation with a pulsewidth of 300μs to each muscle in turn, and then increasing the amplitude to the maximum comfortable value. Each co-activation threshold was chosen by gradually increasing the stimulation level from 0 until the subject's wrist moves. This yielded $u_{c,fcr} = u_{c,ecr} = 110\mu s$. Inevitably one muscle would generate a greater force than the other for a fixed pulsewidth. To equalise the muscle strengths, the gain K_e value was used to scale the ECR input, as shown in Figure 6.3. To achieve this, a slow sine-wave input signal u_1 was applied to move the wrist, and the gain was then selected as $K_e = 0.9$ to produce a symmetrical angular response.

6.3 System Identification

The first step in the EMMILC design process is to define the plant uncertainty set $\mathcal{U}$. In Chapter 5 this was achieved using data extracted from the literature, however in practice this is likely to produce a conservatively large set. Therefore identification tests were conducted in order to reduce the degree of conservatism.

The idea is to collect several sets of input-output data that represent varied muscle conditions (e.g. fatigued, non-fatigued) and environments (e.g. electrodes positioned differently). The FES input sequence used in each data set must be sufficient to excite the arm dynamics. This will be achieved by applying a frequency-varying stimulation input u_2. The resulting wrist movement is recorded to produce the data set (u_1, y_2). A parameterised models of the form (6.7) is then identified from this data set. When this is repeated for every data set, to produce a range of values for each of the parameters in (6.7). This then defines the uncertainty space $\mathcal{U}$.

The next controller design steps then follow those of Chapter 5. Set $\mathcal{U}$ is sampled with a fine resolution to form the initial plant set $\mathcal{H}$ which is used as an input to Algorithm 1. This produces a minimal candidate plant set $\mathcal{P}$ to be used in the EMMILC design procedure.

The rest of this section demonstrates the identification procedure, including data collection, model identification/validation, and construction of the candidate set.

6.3.1 Identification and Evaluation

As stated, the input sequence must sufficiently excite the subject's wrist. It was shown in [Mann et al., 1989] that the average frequency of 24 wrist activities of daily living is approximately $1Hz$, with a $0 \sim 5Hz$ frequency bandwidth. To substantially capture the frequency components of wrist activities, the input for identification has therefore been chosen to comprise a sequence of sine-wave signals with frequencies equal to $0.6Hz$, $0.9Hz$, $1.2Hz$, $1.5Hz$ and $1.8Hz$, as shown in Figure 6.6. This input signal is

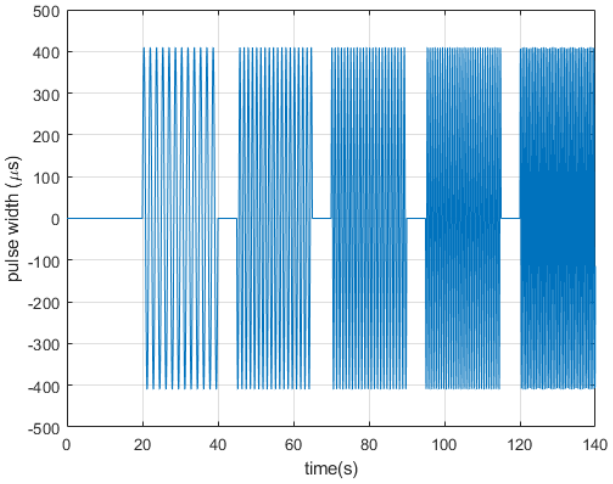

FIGURE 6.6: Input chirp signal (frequency-varying sine-wave). This will be implemented twice, and the gap will not be recorded as a part of the input signal.

applied twice for an overall duration of 280 seconds in order to collect sufficient data points, of which the first half of the data points are used to fit a wrist model of the form (6.7), and the second half is used to validate the accuracy of the identified model. This experiment is conducted 7 times per day with no rest time in between in order to capture muscle fatigue dynamics. This is repeated on 3 separate days to capture the variation due to electrode positioning. As a result, the overall input/output data set used for identification is defined as

$$Z_{i,j}^{N} = \{u_{i,j}(1), y_{i,j}(1), u_{i,j}(2), y_{i,j}(2), ..., u_{i,j}(N), y_{i,j}(N)\}, \tag{6.8}$$

where $i = 1, 2, 3$ and $j = 1, 2, ..., 7$ denote the indices of the day and trial, respectively, with data length N.

The effect of fatigue elicited by these tests is illustrated in Figure 6.7, which compares the output response data across all 7 trials conducted within a single day. It shows that the magnitude of the response decreases to approximately 61% of its initial value due to muscle fatigue. This shows the underlying wrist dynamics have been appropriately captured by the set $Z_{i,j}^{N}$.

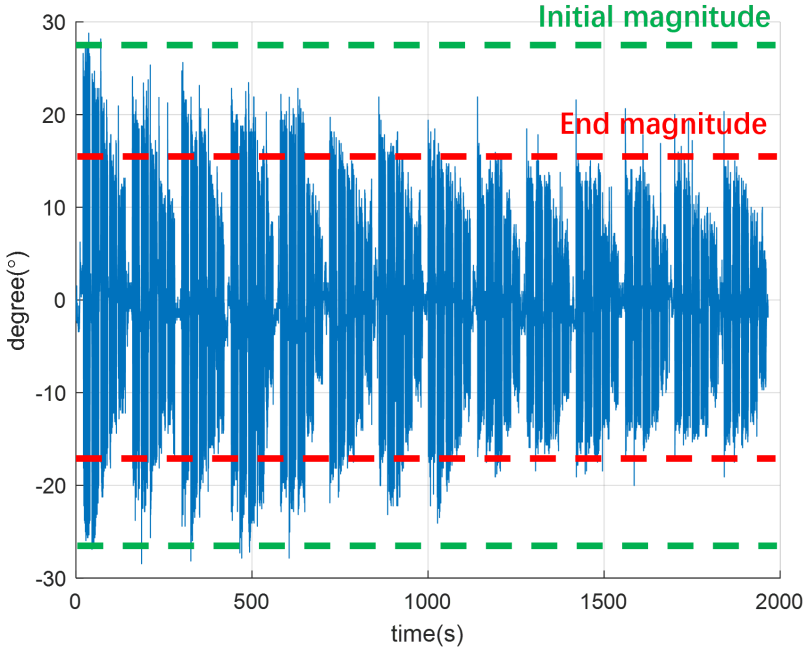

FIGURE 6.7: The effect of fatigue shown by the decrease in output magnitude across all 7 trials, which are conducted within a single day.

The plant identified using the input/output data from the set $Z_{i,j}^N$ will be denoted $p_{i,j}$. To identify $p_{i,j}$, the first step is to define the possible range of variation for each parameter in (6.7). These ranges are denoted $[K_s^{min}, K_s^{max}]$, $[I_s^{min}, I_s^{max}]$, $[B_s^{min}, B_s^{max}]$, $[\omega_n^{min}, \omega_n^{max}]$, and $[h_{IRC}^{min}, h_{IRC}^{max}]$. Their values can be chosen to directly match the ranges in Table 5.1. Then the identification can be formulated as the optimisation problem

$$p_{i,j} := \min_{\substack{K_s \in [K_s^{min}, K_s^{max}], \\ I_s \in [I_s^{min}, I_s^{max}], \\ B_s \in [B_s^{min}, B_s^{max}], \\ \omega_n \in [\omega_n^{min}, \omega_n^{max}], \\ h_{IRC} \in [h_{IRC}^{min}, h_{IRC}^{max}]}} \left(\sum_{k=1}^{N/2} y_{i,j}(k) - \hat{y}_{i,j}(k) \right)^2, \quad (u_{i,j}, y_{i,j}) \in Z_{i,j}^N, \tag{6.9}$$

where $\hat{y}_{i,j}$ is the result of applying input $u_{i,j}$ to the discrete form of system (6.7). This can be computing using

$$\begin{aligned} x(k+1) &= A_d x(k) + B_d u_{i,j}(k) \\ \hat{y}_{i,j}(k) &= C_d x(k), \qquad x(0) = 0 \end{aligned} \tag{6.10}$$

where $k = 0, 1, 2...$ denotes the sample index. System (6.10) is the discrete representation of system (6.7), and has matrices

$$A_d = e^{A_c T_s}, \quad B_d = (e^{A_c T_s} - I) A_c^{-1} B_c, \quad C_d = C_c, \quad D_d = D_c. \tag{6.11}$$

where (A_c, B_c, C_c, D_c) correspond to the state-space realisation of system (6.7) with sampling time T_s, and are given by

$$A_c = \begin{bmatrix} 0 & 1 & 0 & 0 \\ 0 & 0 & 1 & 0 \\ 0 & 0 & 0 & 1 \\ -a_0 & -a_1 & -a_2 & -a_3 \end{bmatrix}, B_c = \begin{bmatrix} 0 \\ 0 \\ 0 \\ 1 \end{bmatrix}, C_c = \begin{bmatrix} b_0 & 0 & 0 & 0 \end{bmatrix}, D_c = \begin{bmatrix} 0 \end{bmatrix} \tag{6.12}$$

where $b_0 = h_{IRC}\omega_n^2 / I_s$, $a_0 = (\omega_n^2 K_s)/I_s$, $a_1 = (2\omega_n K_s + \omega_n^2 B_s)/I_s$, $a_2 = (K_s + 2\omega_n B_s + \omega_n^2 I_s)/I_s$, $a_3 = (B_s + 2I_s\omega_n)/I_s$. The objective is to solve the constrained optimisation problem (6.9) for each data set $Z_{i,j}^N$, and obtain an optimal parameterised model with the best fit parameters $(K_s, I_s, B_s, \omega_n, h_{IRC})$. This is implemented in MATLAB scripts using Optimisation Toolbox ('fmincon' function).

Having found the optimal parameterised model $p_{i,j}$, the next step is to evaluate how well the I/O data $(u_{i,j}, y_{i,j}) \in Z_{i,j}^N$ fits the plant $p_{i,j}$. To do this, the fitting and validating accuracy denoted as $F_{p_{i,j}}$ and $V_{p_{i,j}}$ respectively, are defined as

$$F_{p_{i,j}} = \left(1 - \sqrt{\frac{\sum_{k=1}^{\frac{N}{2}} [y_{i,j}(k) - \hat{y}_{i,j}(k)]^2}{\sum_{k=1}^{N} [y_{i,j}(k)]^2}}\right) \times 100, \tag{6.13}$$

$$V_{p_{i,j}} = \left(1 - \sqrt{\frac{\sum_{k=\frac{N}{2}+1}^{N} [y_{i,j}(k) - \hat{y}_{i,j}(k)]^2}{\sum_{k=1}^{N} [y_{i,j}(k)]^2}}\right) \times 100, \tag{6.14}$$

where $\hat{y}_{i,j}$ is the simulated output for model $p_{i,j}$ defined above. The resulting accuracy is shown by Figure 6.8 and is similar to previous studies [Copur et al., 2016].

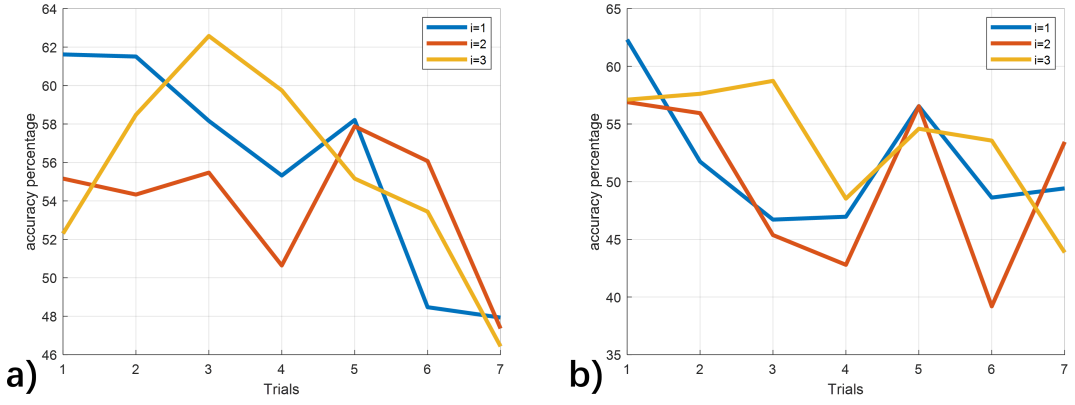

FIGURE 6.8: Identification accuracy of a): fitting $F_{p_{i,j}}$ and b): validating $V_{p_{i,j}}$ computed directly by following the identification approach (6.9)-(6.10) for $i = 1, 2, 3$ and $j = 1, 2, ..., 7$.

To validate the identification approach (6.9)-(6.10), it was compared against a number of leading approaches [Simpkins, 2012] that are implemented within the MATLAB Identification Toolbox. These include parametric identification methods for state-space models, transfer functions (both continuous and discrete time), an autoregressive exogenous (ARX) model, and nonparametric identification of an impulse response model. These methods were all implemented using the same I/O data set $Z_{i,j}^N$. The fitting of each form has been evaluated using (6.13) and (6.14). Results are shown in Figure 6.9, Figure 6.10 and Figure 6.11, and all show a very similar level of accuracy.

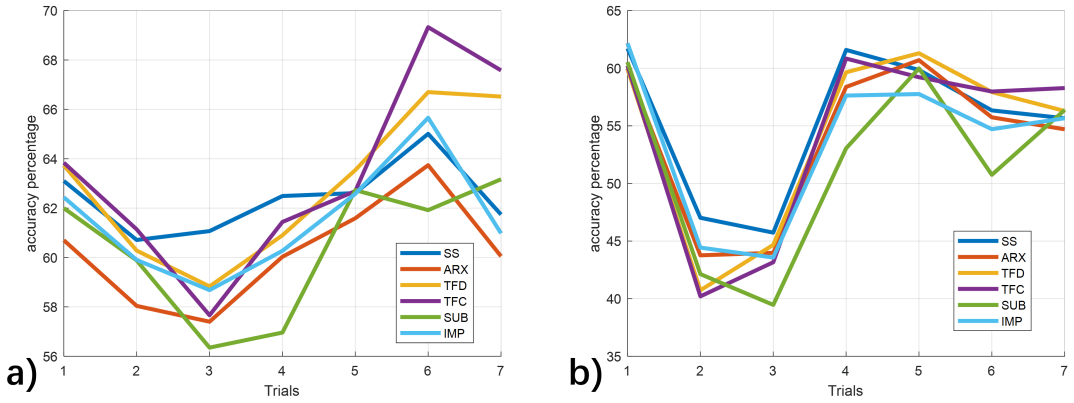

FIGURE 6.9: Identification accuracy of a): fitting $F_{p_{1,j}}$ and b): validating $V_{p_{1,j}}$ for $j = 1, 2, ..., 7$. SS: state-space model. ARX: ARX model. TFD: discrete transfer function. TFC: continuous transfer function. SUB: state-space model (subspace method). IMP: impulse response model.

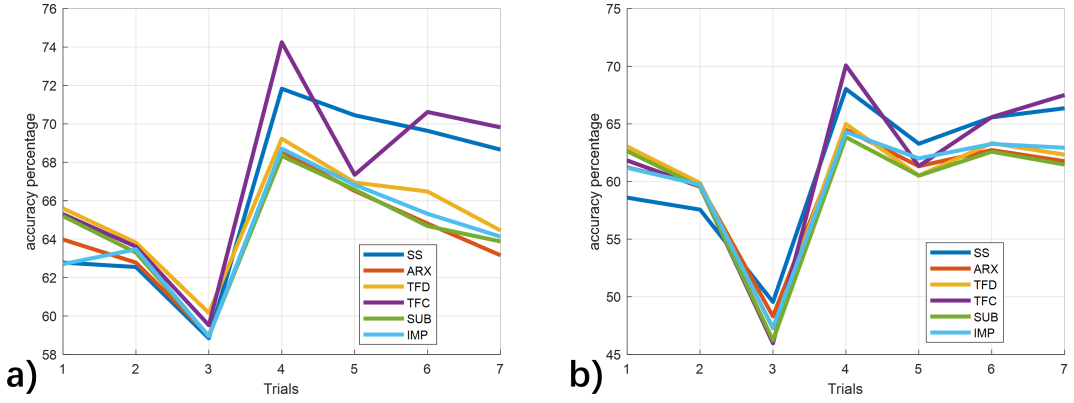

FIGURE 6.10: Identification accuracy of a): fitting $F_{p_{2,j}}$ and b): validating $V_{p_{2,j}}$ for $j = 1, 2, ..., 7$. SS: state-space model. ARX: ARX model. TFD: discrete transfer function. TFC: continuous transfer function. SUB: state-space model (subspace method). IMP: impulse response model.

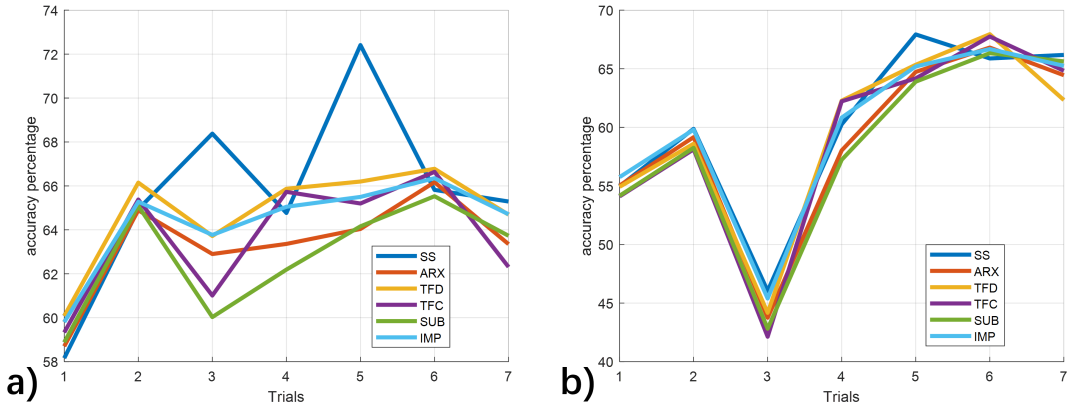

FIGURE 6.11: Identification accuracy of a): fitting $F_{p_{3,j}}$ and b): validating $V_{p_{3,j}}$ for $j = 1, 2, ..., 7$. SS: state-space model. ARX: ARX model. TFD: discrete transfer function. TFC: continuous transfer function. SUB: state-space model (subspace method). IMP: impulse response model.

6.3.2 Candidate Plant Set

The previous identification generated 21 plant models, $p_{i,j}$, with the variation in each parameter shown Figure 6.12. The next step is to finely sample each parameter across its range of variation. Then every combination of parameters is taken and inserted into the form (6.7) to create the plant model set $\mathcal{H}$. This set will be used as the input to Algorithm 1, which produces a minimal candidate plant set $\mathcal{P}$ that will be used in the EMMILC design procedure.

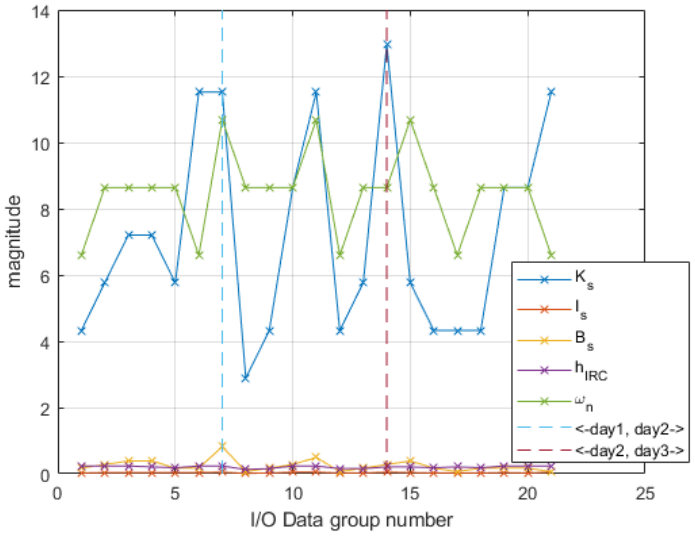

FIGURE 6.12: The variation of parameters in wrist model (6.7) for data set $Z^N_{i,j}$.

According to Figure 6.12, the parameters K_s, B_s and ω_n vary most in physiological changes. The other two parameters I_s and h_{IRC} remain almost unchanged across all

trials. As was done in Section 5.1, a minimum set will be formed by only sampling from the range of parameters K_s, B_s and ω_n that vary most, and fixing the parameters I_s and h_{IRC} at their average values. Following this approach, Table 6.1 gives the sample values of each wrist parameter. Among these parameters, the stiffness K_s demonstrates a considerably higher value compared to the one given in Table 5.1. The reason for this is that the wrist data was solely collected from a young subject with a robust forearm, typically exhibiting enhanced muscle power. The study conducted by Ikezoe et al. [2012] analysed the Pearson correlation coefficient and found that enhanced muscle power often results in a larger variation in muscle stiffness when transitioning from rest to contraction, particularly in young individuals.

TABLE 6.1: Values of wrist parameters.

Parameter	Symbol	Sample Values	Unit
IRC constant	h_{IRC}	0.206	N/A
Natural frequency	ω_n	6.597, 7.278, 7.959, 8.639, 9.320, 10.001, 10.681	rads/s
Stiffness	K_s	2.886, 4.565, 6.244, 7.923, 9.602, 11.281, 12.960	Nm/rad
Damping	B_s	0.064, 0.189, 0.315, 0.440, 0.566, 0.691, 0.817	Nms/rad
Inertia	I_s	0.033	Nms^2/rad

As shown in Table 6.1, seven samples were uniformly taken across each uncertain range. Then each combination of samples is used to build an underlying plant using (6.7). These plants give the initial plant set $\mathcal{H} = \{p_1, p_2, p_3, ..., p_{N_m}\}$ with $N_m = 343$ underlying plant models. This set $\mathcal{H}$ is used as the input to Algorithm 1, in which the tuning parameter is set to $\gamma = 1$. This is chosen to establish whether a minimum plant model set can provide satisfactory performance. The inverse ILC update (5.4) is still employed as the design procedure $\hat{c} = K(p)$ due to its fast convergence. A 10^{th} order zero phase low-pass filter Q_2 was designed with cut-off frequency $3Hz$ to better reject high frequency noise and disturbances. The effectiveness of this filter Q_2 applied with ILC system was proved by [Elci et al., 2002], where the tracking error was reduced by a factor of 100 over 6 ILC trials in the presence of high-frequency vibration disturbances. Hence the ILC update used in this experiment is given by

$$u_2(k+1) = Q_2[u_2(k) - P_{\hat{p}}^{-1} y_2(k)], \quad \forall P_{\hat{p}} \in \mathcal{H}. \tag{6.15}$$

The output of Algorithm 1 is the minimal candidate plant set $\mathcal{P} = \{P_{\hat{p}_1}, P_{\hat{p}_2}, \cdots, P_{\hat{p}_{N_p}}\}$ comprising $N_p = 95$ plants (248 having been removed). The corresponding candidate controller set $\mathcal{C} = \{C_{\hat{c}_1}, C_{\hat{c}_2}, C_{\hat{c}_3}, \cdots, C_{\hat{c}_{N_p}}\}$ also contains 95 ILC controllers. This controller $\mathcal{C}$ set will then be used to examine the capability of EMMILC in the next section.

6.4 Evaluation of Tracking Performance

To evaluate the performance of EMMILC, it will be compared to standard ILC. The latter is designed using (6.15) with the nominal plant $\hat{p}_{52}$ (corresponding to $p_{52} \in \mathcal{P}$), which is very similar to model $p_{1,1}$ identified using $Z_{1,1}^{N}$. This choice of plant model replicates how standard ILC would normally be designed, since it uses a model that has no muscle fatigue.

To ensure fair comparison, EMMILC is implemented with the same choice of initial model. This yields the initial ILC update $\hat{c}_{52} = K(p_{52})$. The section 6.3.1 illustrated that about 280 seconds of continuous FES stimulation was adequate to cause fatigue in the wrist flexor and extensor muscles. This has been evidenced by the output amplitude dropping to 61% of its initial level. To induce fatigue, both EMMILC and standard ILC are implemented over 50 trials lasting 400 seconds in total according to a standardised protocol, thereby comprehensively covering the 280 seconds duration of the identification test, which demonstrated the onset of fatigue. The subject is allowed to rest sufficiently (longer than one hour) before each experiment to prevent initial fatigue before stimulation.

To illustrate the capability of EMMILC, its tracking performance is now compared with the results of standard ILC at trial 10 for initial convergence, and trial 50 for long-term convergence. The tracking plots are shown in Figure 6.13 for standard ILC and Figure 6.14 for EMMILC. The findings indicate that EMMILC is capable of maintaining robust performance even after achieving initial convergence. In contrast, the tracking performance of standard ILC significantly degraded as a result of model mismatch caused by physiological variations.

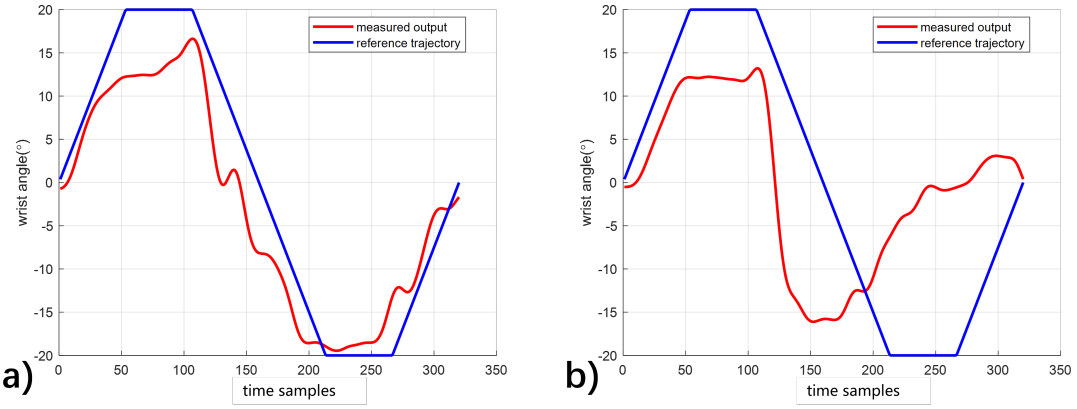

FIGURE 6.13: The tracking plots in time domain for standard ILC at a): trial 10 and b): trial 50.

To measure the variation of tracking performance along the trials, the error ratio $ER(k)$ is computed for each ILC trial k. A smaller value of $ER(k)$ indicates higher accuracy

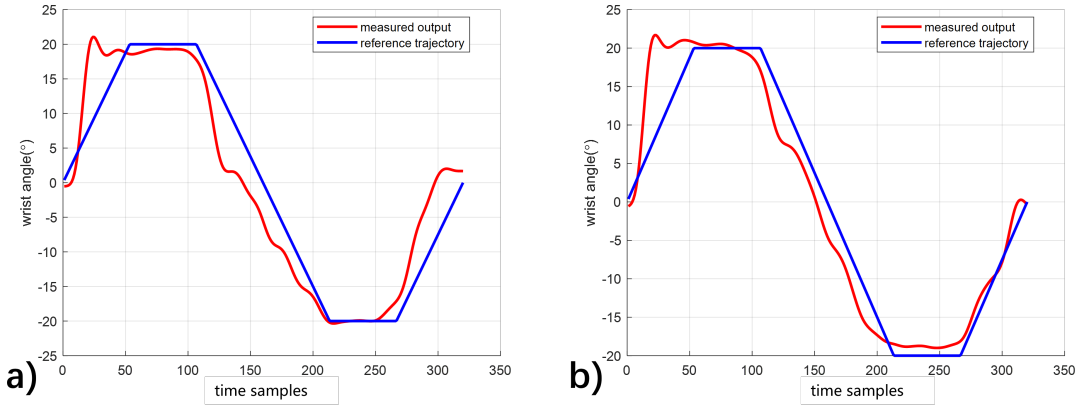

FIGURE 6.14: The tracking plots in time domain for EMMILC at a): trial 10 and b): trial 50.

over trial k. This is defined by

$$ER(k) := \frac{\|y_2(k)\|}{\|y_{ref}\|}. \tag{6.16}$$

The results are illustrated by Figure 6.15, and the corresponding EMMILC switching signal is shown by Figure 6.16.

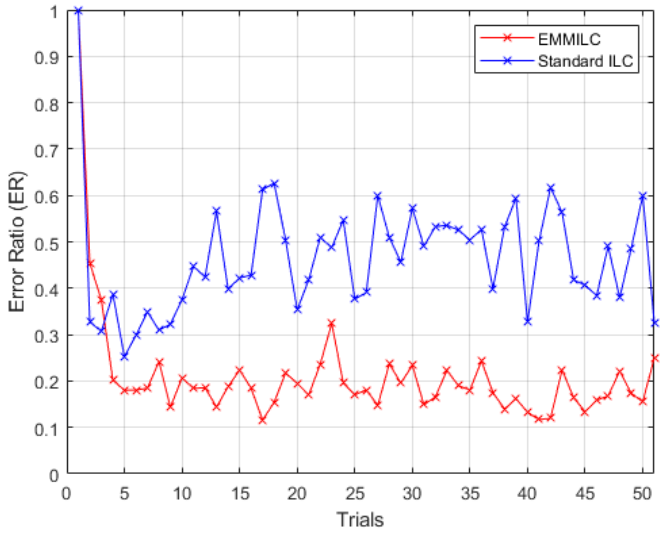

FIGURE 6.15: Comparison of tracking performance between standard ILC and EMMILC.

The results showed that the standard ILC approach reduced tracking error by 70% of its initial value within 5 trials by using the update $\hat{c}_{52} = K(p_{52})$. However, there was a fast occurrence of fatigue after trial 8 that significantly degraded the tracking performance of standard ILC to the end of experiment. This motivated EMMILC to provide a better robust performance.

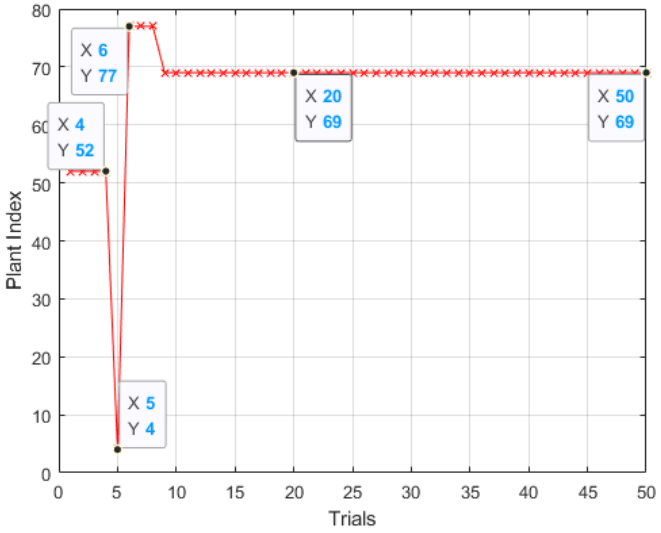

FIGURE 6.16: EMMILC switching signal.

As a comparison, EMMILC kept its tracking error at a low level (20% of initial error) with the existence of fatigue by switching to ILC update $\hat{c}_{69} = K(p_{69})$ at the end of trial 8 (shown by Figure 6.16). Across 50 stimulation trials lasting over 400 seconds, EMMILC maintained lower tracking errors compared to standard ILC, despite the onset of muscle fatigue during the 280 seconds of the identification test, as illustrated by Figure 6.7. This provides strong evidence that EMMILC can appropriately cope with physiological changes (e.g. fatigue) by updating the candidate plant models generated from Algorithm 1, and hence yields a better robust performance that outperforms existing standard ILC.

6.5 Initial Evaluation of Misalignment

The earlier results showed feasibility with a single test participant. The effect of fatigue and other physiological variation was evaluated, however perfect electrode positioning was assumed. However, in practice the electrodes will never be positioned exactly as they were during previous sessions or when the model identification was performed.

To mimic real conditions over a programme of rehabilitation, the previous tests are now repeated on four further subjects using both aligned electrode (**AE**) and misaligned electrode (**ME**) positions as shown in Figure 6.17. The electrode initially positioned on the distal side of the extensor is shifted towards the proximal side of the extensor by approximately 2.5 cm, corresponding to half the width of the electrode pad. This aims to replicate the variation in electrode placement that would naturally occur in clinical practice.

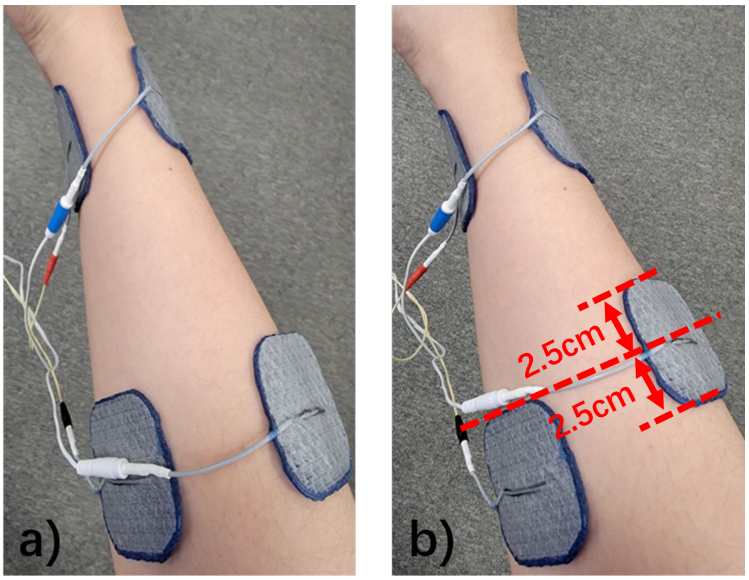

FIGURE 6.17: Electrode placements: a) **AE** and b) **ME** positions.

To address misalignment, it is first necessary to include its effect in the model (6.7). It is observed from multiple tests that the closer the two electrodes in a pair are positioned to one another, the smaller the resulting muscle torque becomes. This is illustrated by Figure 6.17 b), where the electrodes positioned on the wrist extensor are closer to one another, yielding smaller wrist extension in contrast to the wrist flexion movement. This can be modelled by multiplying the stimulation applied to each muscle by a different scalar value, where a smaller scalar value corresponds to greater electrode misalignment. These are implemented in the previous model (6.7) by exchanging the gain h_{IRC} for the piecewise linear function

$$w = h_{IRC}(u_1) := \begin{cases} \alpha u_1, & u_1 \geq 0 \\ \beta u_1, & u_1 < 0 \end{cases}, \tag{6.17}$$

where w is the internal muscle torque, and α, β are the misalignment parameters for FCR and ECR muscles respectively. Then system model (6.7) is replaced by

$$Y_1(s) = \underbrace{\frac{1}{I_s s^2 + B_s s + K_s}}_{H_{RBD}} \underbrace{\frac{\omega_n^2}{s^2 + 2\omega_n s + \omega_n^2}}_{H_{LAD}} W(s), \tag{6.18}$$

where $X(s)$ denotes the Laplace transformed signal $x(t)$ in the time domain. This new model form can be applied directly to the identification and candidate model design procedures described in Section 6.3 and 4.2, simply exchanging parameter h_{IRC} with parameters α, β.

To conduct misalignment tests, four unimpaired subjects were recruited, as a prerequisite for later clinical tests with stroke patients. The identification procedure described

in Section 6.3 was applied to only one subject to identify an uncertainty set. This aims to evaluate whether a candidate model set generated using one subject's data could yield satisfactory performance with all subjects. If successful, this would effectively remove the need for model identification and hence constitute a major step towards achieving model-free, home-based FES rehabilitation. Having collected data sets, the identified models had a fitting accuracy range of $61\% - 71\%$ and a validation accuracy range of $59\% - 68\%$. The parameters of these identified models varied in the ranges summarised in Table 6.2. This test involved an elder subject with reduced muscle power, which led to significantly smaller values of muscle stiffness compared with the values identified in Table 5.1 and 6.1. Nonetheless, this uncertainty space given in Table 6.2 remained valid for all subjects, as the stiffness values that exceeded the uncertainty range were absorbed by other amplitude parameters (e.g., α and β). Applying the design procedure

TABLE 6.2: Values of wrist parameters.

Parameter	Symbol	Uncertainty range	Unit
Natural frequency	ω_n	$5 \sim 15$	rads/s
Stiffness	K_s	$0.01 \sim 0.08$	Nm/rad
Damping	B_s	$0.001 \sim 0.01$	Nms/rad
Inertia	I_s	$0.00001 \sim 0.0001$	Nms^2/rad
Coefficient α	α	$0.6 \sim 1.2$	N/A
Coefficient β	β	$0.9 \sim 1.1$	N/A

Algorithm 1 then produced a minimal candidate set $\mathcal{P} = \{P_{p_1}, P_{p_2}, ..., P_{p_{N_p}}\}$ comprising $N_p = 116$ plants (4 having been removed).

The first tests compared standard ILC with EMMILC for all subjects using **AE** positioning. Standard ILC required a new model to be identified. Therefore the identification procedure described in Section 6.3 was applied with each subject. The resulting identified model was then lifted to give $P_{\hat{p}}$ which was applied with standard ILC update (6.15) to track y_{ref} over 50 trials, in order to fully induce muscle fatigue during intensive stimulation.

After a 20-minute rest, EMMILC was then performed over 50 trials using the same candidate set defined above for each subject. The tracking performance was measured by introducing the new, more informative, performance index

$$PI_{N_k} = \sum_{k=1}^{N_k} \frac{\|y_2(k)\|}{\|y_{ref}\|}, \tag{6.19}$$

where N_k denotes a total trial number of interest. This index accumulates the error ratio over the first N_k trials and captures both convergence speed and final tracking accuracy [Ratcliffe et al., 2006b]. The smaller the value of PI_{N_k}, the better the tracking performance over the N_k trials. By computing this index, the tracking performance for each subject is shown in Table 6.3 for standard ILC, and Table 6.4 for EMMILC.

TABLE 6.3: Quantified performance PI_{50} and PI_{10} values for each subject using standard ILC with **AE** and **ME** electrode positions.

	Standard ILC			
Subject	**AE**(PI_{50})	**AE**(PI_{10})	**ME**(PI_{50})	**ME**(PI_{10})
a	14.94	4.75	23.17	7.67
b	16.33	5.98	23.44	7.55
c	16.42	4.93	21.94	5.45
d	30.94	7.69	105.11 (diverging)	9.35

TABLE 6.4: Quantified performance PI_{50} and PI_{10} values for each subject using EMMILC with **AE** and **ME** electrode positions.

	EMMILC			
Subject	**AE**(PI_{50})	**AE**(PI_{10})	**ME**(PI_{50})	**ME**(PI_{10})
a	13.95	5.81	15.11	5.77
b	12.32	3.68	12.09	4.06
c	16.39	4.91	14.88	4.67
d	26.76	7.96	32.54	8.89

This shows that all subjects performed better using EMMILC, as the PI_{50} values are smaller than those of standard ILC. Specifically, Figure 6.20 shows the results with subject *a*, where EMMILC has approximately 25% better performance. In terms of the convergence over the initial 10 trials, measured using PI_{10}, EMMILC provides similar performance compared with standard ILC.

Figure 6.22 a) shows the control effort $\|u_2(k)\|$ applied to subject b over trial $k = 1, 2, \ldots, 50$ using standard ILC and EMMILC. In both cases the FES energy increases over time due to muscle fatigue. However, this continuous increase of stimulation increases patient discomfort, especially in the case of standard ILC. In comparison, EMMILC has reduced the stimulation required by using the most accurate plant model on every trial, thereby minimising energy. In contrast, standard ILC employs an inaccurate plant model which wastes effort by exciting modes/frequencies not required by the task.

In a home-use or wearable scenarios there is limited processing power, meaning that fewer candidate plant models can be supported. To investigate the effect of limited computational resources, EMMILC was next redesigned to have fewer candidate plants. This was achieved by designing $Q_{\hat{c}}$ in Algorithm 1 to reduce robustness when minimising (3.59) and hence cover the uncertainty space with fewer candidate plants. As a compromise, the convergence rate of each plant model is reduced. To examine this, four candidate sets were produced with a descending number of plants. Each of them was applied on one subject with **AE** positioning over 50 trials. The results are then presented in Table 6.5.

The results show that the tracking performance of EMMILC reduces as the number of candidate plants (and hence computational load) reduces. Comparison between Table

TABLE 6.5: Quantified performance for four different plant sets.

Plant set	No. plants	PI_{50} value
$\mathcal{P}_1$	$N_p = 116$	12.32
$\mathcal{P}_2$	$N_p = 97$	13.81
$\mathcal{P}_3$	$N_p = 71$	14.03
$\mathcal{P}_4$	$N_p = 30$	14.66

6.5 and Table 6.3 shows that, even with only 30 models, the performance of EMMILC is still superior to that of standard ILC. This supports the efficacy of EMMILC to be used for home-based FES rehabilitation. However, the subject reported a larger oscillation of wrist movements as the number of candidate models decreased, slightly reducing comfort during testing.

The test procedure was then repeated with the **ME** position. Results show that EMMILC significantly outperformed standard ILC, which could not stabilise the system with subject *d*. This is manifested in both short-term (PI_{10}) and long-term (PI_{50}) convergence in Table 6.4. The tracking plots of standard ILC with electrode pads in **AE** and **ME** positions were shown in Figure 6.18. This demonstrated that even a minor misplacement of one electrode pad can substantially degrade the performance of standard ILC. As a comparison, EMMILC maintained good performance with electrode misaligned, as shown in Figure 6.19. This not only illustrated that EMMILC outperformed standard ILC in handling model uncertainty, but also produced remarkable outcomes that the candidate plant set employed for all subjects was built only for subject *b*. This confirms the possibility that no further identification is required for different subjects.

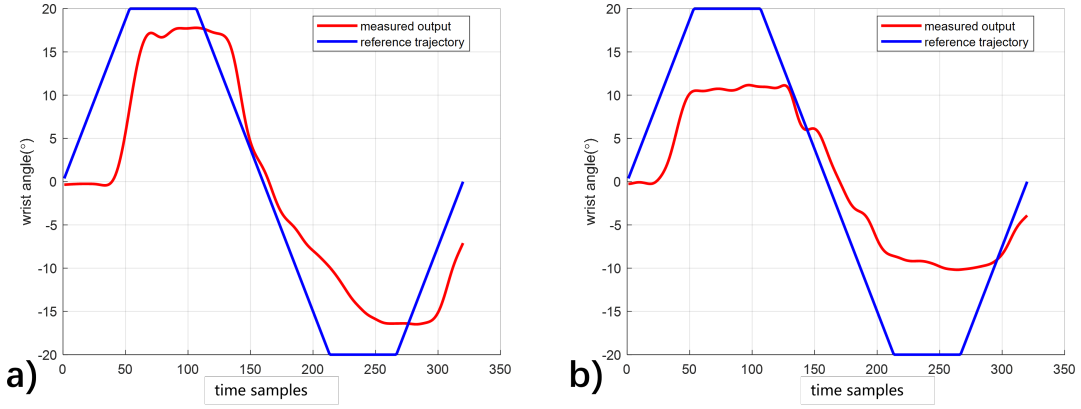

FIGURE 6.18: The tracking plots in time domain for standard ILC with electrode pad at a): **AE** position and b): **ME** position.

To illustrate the switching process, the tracking results of subject *a* are shown for **AE** (Figure 6.20) and **ME** (Figure 6.21), positioning. As in Figure 6.20 a), standard ILC decreased its tracking error to 26% of its initial value within 10 trials. In comparison,

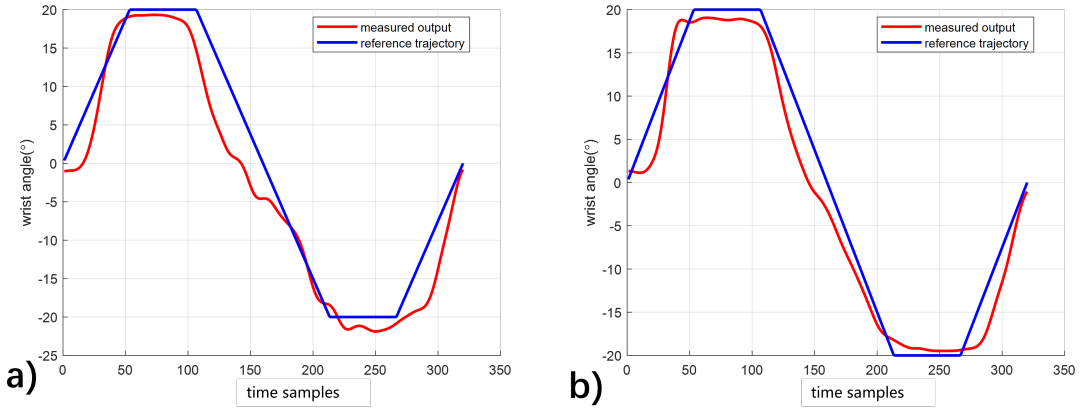

FIGURE 6.19: The tracking plots in time domain for EMMILC with electrode pad at a): **AE** position and b): **ME** position.

EMMILC required 10 trials to reach 14% of its initial value. The switching process is shown Figure 6.20 b), where the change in wrist dynamics started to increase after trial 29. EMMILC adapted to this by switching to other candidate plants. As shown in Figure 6.21 a), EMMILC decreased to 19% of its initial error after 10 trials, but standard ILC decreased to only 47% of its initial error. Similarly, EMMILC also adapted to the increased physiological variation following trial 29, as shown in Figure 6.21 b).

Figure 6.22 b) shows the control effort used by each ILC type. EMMILC clearly applied much smaller stimulation inputs to subject *b* compared to standard ILC with **ME** positioning, illustrating that it can deal with fatigue much more effectively. EMMILC also achieved far better performance with **ME** positioning, as shown in Table 6.4.

6.6 Summary

This chapter introduced an experimental set-up and associated hardware that corresponded to a realistic FES rehabilitation scenario. Co-activation and muscle force equalisation were applied to reduce the effect of the muscle recruitment dead-zone. Then, a comprehensive identification procedure was conducted to capture parametric variations that include fatigue and electrode positioning. As a result, the initial plant set was constructed by sampling the variation in all the wrist model parameters. The minimum candidate plant set provided by Algorithm 1 was then tested by implementing EMMILC on a healthy subject. The results experimentally confirmed the proof of concept and showed that EMMILC outperforms standard ILC. Further experiments involved conducting additional misalignment tests. The EMMILC framework was experimentally tested with four healthy test subjects and automatically adapted to their levels of fatigue and electrode misalignment. As a result, EMMILC has improved performance by 28% compared to standard ILC.

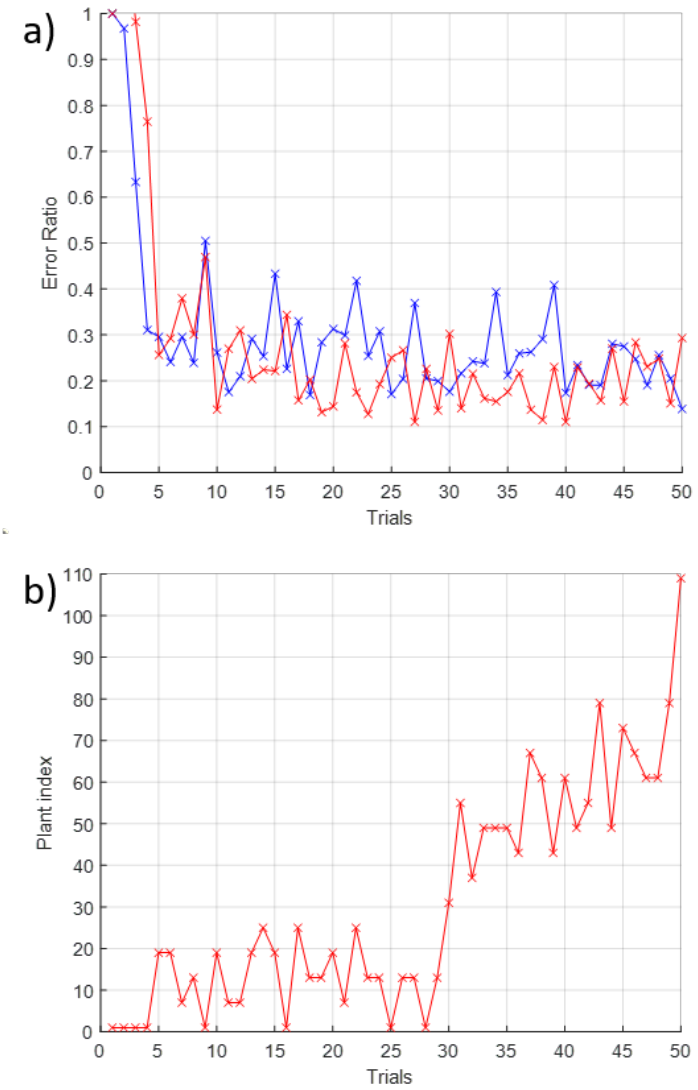

FIGURE 6.20: The tracking performance with electrodes in standard position shown by a) [Red line] Tracking error ratio of EMMILC in each trial with standard electrode positioning. [Blue line] Tracking error ratio of Standard ILC in each trial with standard electrode positioning. b) Switched plant for EMMILC in each trial.

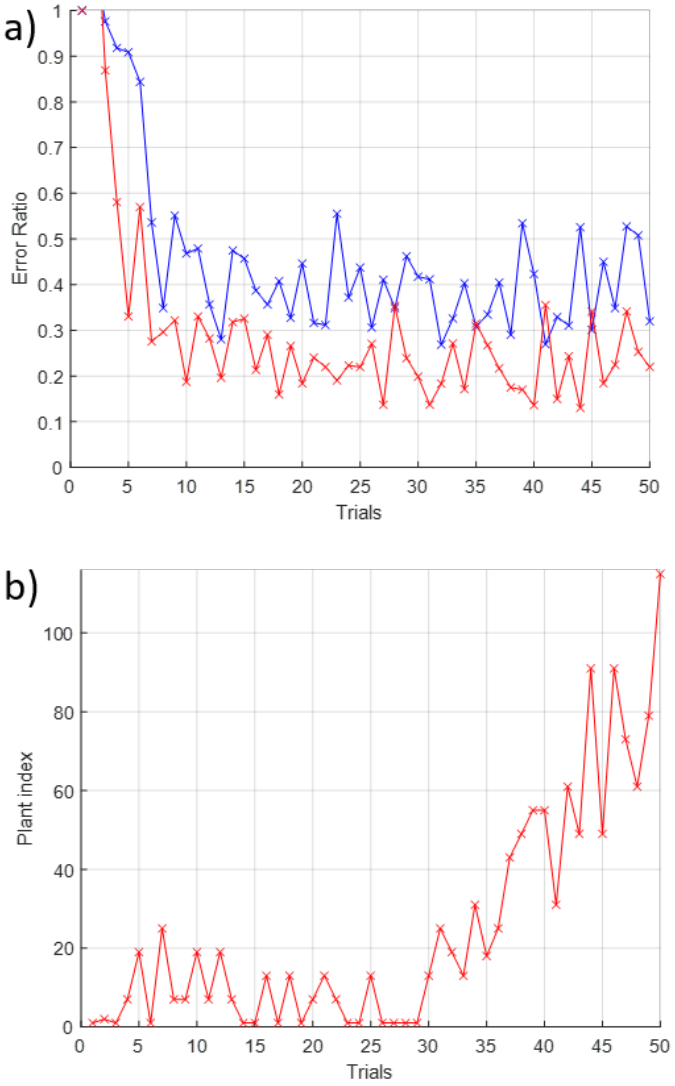

FIGURE 6.21: The tracking performance with electrodes in misaligned position shown by a) [Red line] Tracking error ratio of EMMILC in each trial with misaligned electrode positioning. [Blue line] Tracking error ratio of Standard ILC in each trial with misaligned electrode positioning. b) Switched plant for EMMILC in each trial.

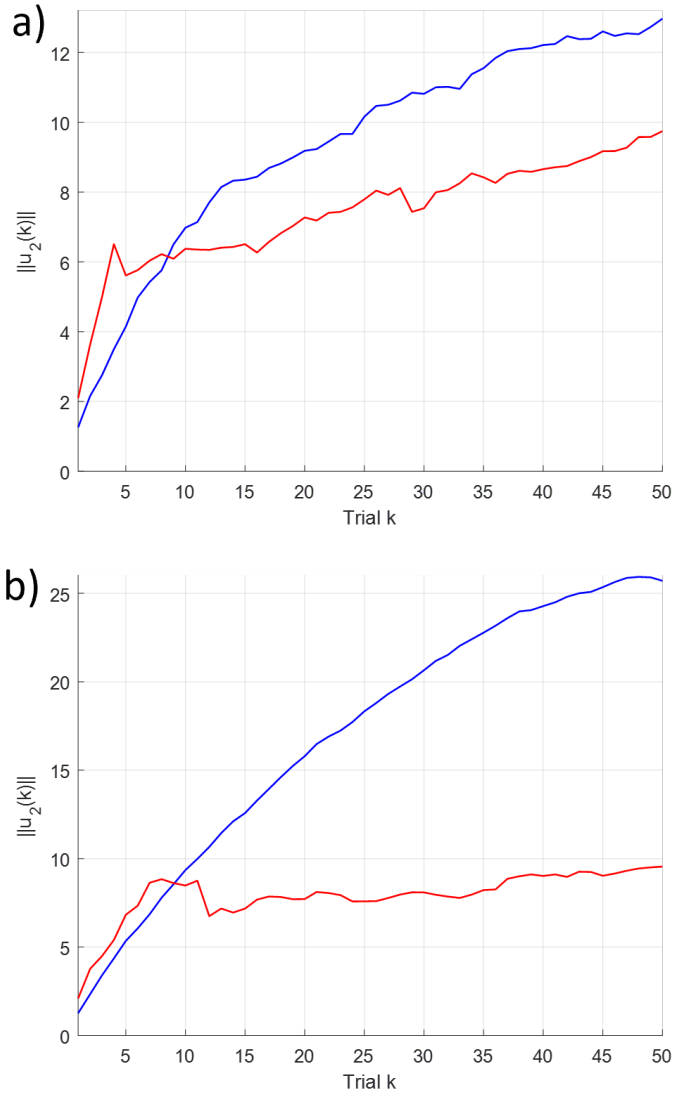

FIGURE 6.22: Control energy $\|u_2(k)\|$ plots of a) [Red line] EMMILC in trial k with **AE** positioning. [Blue line] standard ILC in trial k with **AE** positioning. b) As above but with **ME** positioning.

Chapter 7

Numerical Evaluation of Misalignment

While the previous chapters have validated EMMILC's capability in handling model uncertainty, they have ignored the issue of misalignment, which often results in decreased accuracy in practical applications. Positioning of electrodes often takes $10-15$ minutes and will inevitably vary between sessions. The assessment provided in Chapter 2 also indicates that spatial inaccuracies in the application of FES could result in discomfort [Micera et al., 2010] when stimulated, as well as lead to inadequate movement outcomes [Crema et al., 2018]. This source of uncertainty has not been investigated in FES control, either experimentally or numerically. The purpose of this chapter is to investigate the misalignment effect by building on the simulation from Chapter 5. It first evaluates how differing degrees of misalignment influence the effectiveness of standard ILC, and then goes on to assess the effectiveness of the previous EMMILC design in handling them.

7.1 Misaligned Model

To capture the effect of electrode misalignment, it is essential to model the effect of varying the point at which FES is applied via an electrode positioned on the skin surface. Early studies [Livshitz et al., 2001; Kenney et al., 2016; Chu et al., 2023] primarily used the finite element method to compute the current distribution within nerves and optimise electrodes positioning. However, these models were computationally intensive and incompatible with model-based control applications. To address these limitations, [Freeman et al., 2016; Kutlu et al., 2016a] treated the stimulation effect as a linearly combined activation of all muscles. This reduced computational burden and was applicable for model-based control design. However, they ignored the effects of misalignment, limiting its applicability for adaptive FES control in a home-use scenario. An alternative model was proposed in [Gauthier et al., 2017], where an analytical model based on Fourier series was used to calculate the electric field distribution, which offered more

physical meaning than a weighted sum. Unfortunately, it still did not consider spatial misalignment, and was not validated for FES-based upper-limb rehabilitation. Obien et al. [2015] presented a rigorous analysis by applying Coulomb's law to determine the electric distribution across the electrode array, a method grounded in underlying physics. Therefore, this approach will now be adapted to determine the effect of electrode position change.

Consider an electrode positioned within a fixed coordinate system (x_1, x_2), such that FES is applied to the muscle activation point located at (x_1', x_2'). According to Coulomb's law, the electric field F generated by a charge of magnitude q at a distance r can be described by the formula $\frac{\kappa q}{r^2}$, where κ is the Coulomb's constant. As a result, we model our electrode pad as an area of S which has uniform charge, and is situated around the muscle activation point (x_1', x_2'), as illustrated in Figure 7.1 a). Consequently, this yields the electric field at the muscle activation point of

$$F(t) = \underbrace{\left(\iint_S \frac{\kappa}{\|(x_1, x_2) - (x_1', x_2')\|^2} dx_1 dx_2 \right)}_{A} u(t). \tag{7.1}$$

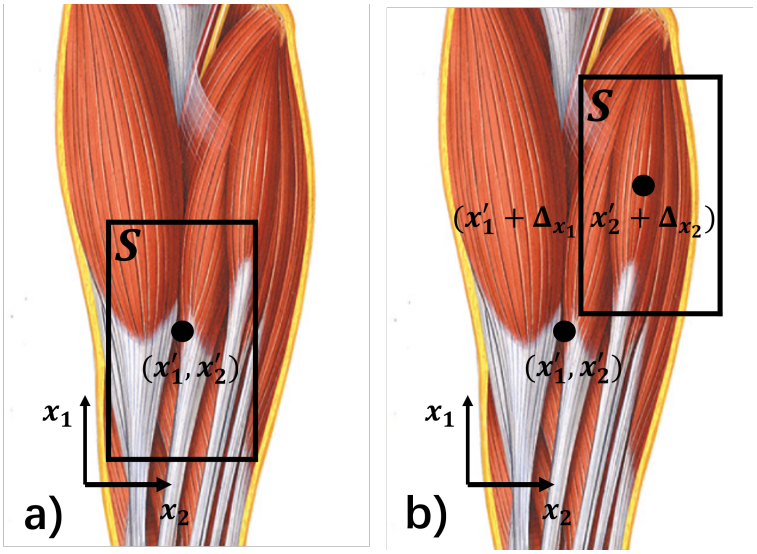

FIGURE 7.1: Geometry coordinates (x_1, x_2) with muscle activation points defined by a): standard position (x_1', x_2'). b): a shift in electrode position given by $(\Delta_{x_1}, \Delta_{x_2})$.

Specifically. the result $F(t)$ can be interpreted as the electric field contribution at the muscle activation point (x_1', x_2') from a unit charge located at (x_1, x_2) in the fixed coordinate system. The integral in (7.1) is performed over the surface area S of the electrode pad, excluding a unit charge located at (x_1, x_2) that perfectly aligns with the muscle activation site (x_1', x_2') to avoid singularity ($(x_1, x_2) \neq (x_1', x_2')$).

Here stimulation signal $u(t)$ is assumed to equal charge $q(t)$. If this is not the case, its constant of proportionality can be absorbed into κ. In Chapter 5, the input to the h_{IRC}

block was $u(t)$, as shown in Figure 5.1. Based on the field (7.1), this input $u(t)$ therefore corresponds to $\frac{F(t)}{A}$.

Now consider a shift in electrode position given by $(\Delta_{x_1}, \Delta_{x_2})$, as illustrated in Figure 7.1 b). The field is decreased to

$$F(t) = \left(\oiint_S \frac{\kappa}{\|(x_1, x_2) - (x_1' + \Delta_{x_1}, x_2' + \Delta_{x_2})\|^2} dx_1 dx_2 \right) u(t), \tag{7.2}$$

and the h_{IRC} block's input reduces from $u(t)$ to a new value given by

$$v(t) = \frac{F(t)}{A} = \underbrace{\left(\oiint_S \frac{\|(x_1, x_2) - (x_1', x_2')\|^2}{\|(x_1, x_2) - (x_1' + \Delta_{x_1}, x_2' + \Delta_{x_2})\|^2} dx_1 dx_2 \right)}_{A(\Delta_{x_1}, \Delta_{x_2})} u(t). \tag{7.3}$$

If there is no misalignment, then $A(\Delta_{x_1}, \Delta_{x_2}) = A(0,0) = 1$, and $v(t) = u(t)$ is restored.

To modify the hand model (5.1) detailed in Chapter 5, to incorporate the impact of misalignment, Figure 5.1 becomes

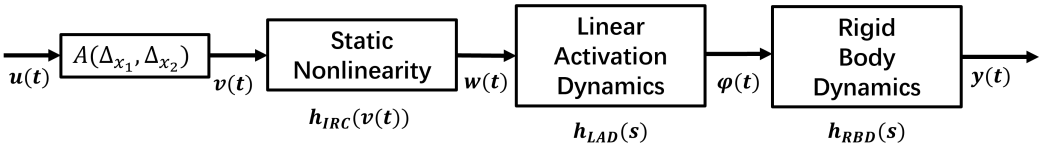

FIGURE 7.2: Modified model structure that includes the effect of misalignment $A(\Delta_{x_1}, \Delta_{x_2})$, where the FES is reduced.

Model (5.1) is modified to the general form

$$P_p = h_{IRC} \, \frac{\omega_n^2}{s^2 + 2\omega_n s + \omega_n^2} \, \frac{1}{I_s s^2 + B_s s + K_s} \, A(\Delta_{x_1}, \Delta_{x_2}), \tag{7.4}$$

where $A(\Delta_{x_1}, \Delta_{x_2})$ is defined in (7.3).

Recall from Section 5.1 that the lifted plant $P_{\hat{p}}$ is derived from the unlifted plant P_p, which is characterised by the state-space representation $p = (A_p, B_p, C_p, D_p)$. To fit the misaligned plant (7.4) into the ILC framework, the matrix B_p and D_p are simply modified to $B_p A(\Delta_{x_1}, \Delta_{x_2})$ and $D_p A(\Delta_{x_1}, \Delta_{x_2})$, respectively. Inserting these into the matrix (5.2), this yields the misaligned lifted plant

$$P_{\hat{p}} = \begin{bmatrix} D_p A(\Delta_{x_1}, \Delta_{x_2}) & 0 & \cdots & 0 & 0 \\ C_p B_p A(\Delta_{x_1}, \Delta_{x_2}) & D_p A(\Delta_{x_1}, \Delta_{x_2}) & \cdots & 0 & 0 \\ C_p A_p B_p A(\Delta_{x_1}, \Delta_{x_2}) & C_p B_p A(\Delta_{x_1}, \Delta_{x_2}) & \cdots & 0 & 0 \\ \vdots & \vdots & \ddots & \vdots & \vdots \\ C_p A_p^{N-2} B_p A(\Delta_{x_1}, \Delta_{x_2}) & C_p A_p^{N-3} B_p A(\Delta_{x_1}, \Delta_{x_2}) & \cdots & D_p A(\Delta_{x_1}, \Delta_{x_2}) & 0 \\ C_p A_p^{N-1} B_p A(\Delta_{x_1}, \Delta_{x_2}) & C_p A_p^{N-2} B_p A(\Delta_{x_1}, \Delta_{x_2}) & \cdots & C_p B_p A(\Delta_{x_1}, \Delta_{x_2}) & D_p A(\Delta_{x_1}, \Delta_{x_2}) \end{bmatrix}. \tag{7.5}$$

In Chapter 5, the true lifted plant $P_{\hat{p}^*}$ was considered to be an aligned plant. This is equivalent to the misaligned structure (7.5) with $A(\Delta_{x_1}, \Delta_{x_2}) = A(0,0) = 1$. If there is misalignment $(\Delta_{x_1}, \Delta_{x_2})$, the true lifted plant $P_{\hat{p}^*}$ will be computed using (7.5) with $A(\Delta_{x_1}, \Delta_{x_2}) \neq 1$. The ILC plant dynamics are

$$y_1(k) = P_{\hat{p}^*} u_1(k), \tag{7.6}$$

which fits into the structure of Figure 3.2, and makes Theorem 3.1 applicable for designing a robust ILC controller.

7.2 Numerical Evaluation of Standard ILC

Having defined the misaligned model, the numerical evaluation performed in Chapter 5 using standard ILC is now repeated with the misaligned plant P_{p^*}. Aiming to focus exclusively on misalignment, the ILC controller is designed by applying the aligned model $P_{\hat{p}}$ to design procedure $C_{\hat{c}} = K(P_{\hat{p}})$ with (5.4). The control parameters are identical to the settings in Chapter 5. As a comparison, the shifts $(\Delta_{x_1}, \Delta_{x_2})$ in electrode position are set to $(0,0)cm$, $(0.4,0.4)cm$, $(0.8,0.8)cm$, $(1.2,1.2)cm$, and $(1.6,1.6)cm$, corresponding to increasing levels of misalignment in both the x_1 and x_2 directions. The error norm convergence over 20 ILC trials are shown by Figure 7.3.

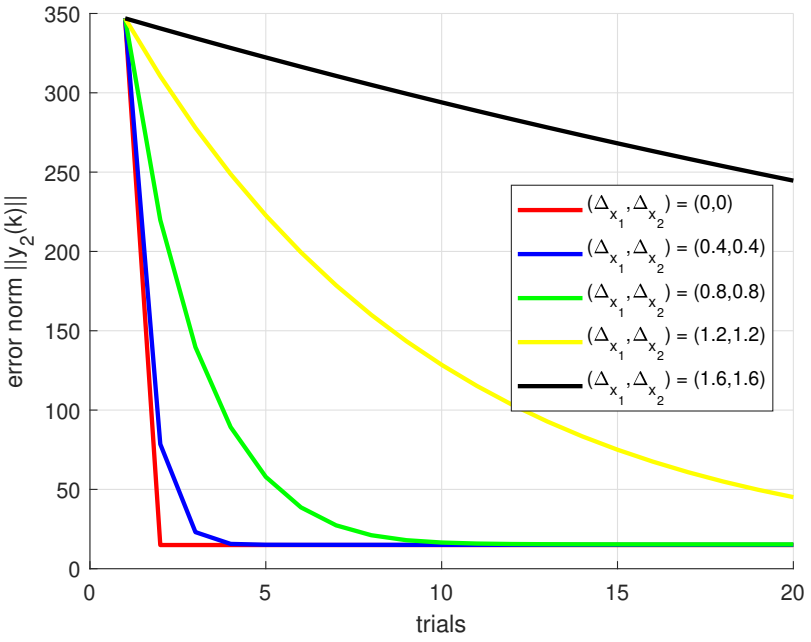

FIGURE 7.3: Convergence of error norm (Standard ILC) for each trial k with respect to increasing levels of misalignment.

Utilising the performance index (5.5), the performance of standard ILC can be compared effectively across varying levels of misalignment. Table 7.1 displays the results, illustrating an 860.17% increase in the accumulated error of standard ILC when the electrode is displaced by a distance of 2.26cm from the muscle activation site. The effect of misalignment has been to dramatically reduce the convergence rate of ILC.

TABLE 7.1: Comparison of standard ILC performance for increasing levels of misalignment $(\Delta_{x_1}, \Delta_{x_2})$.

$(\Delta_{x_1}, \Delta_{x_2})$	$A(\Delta_{x_1}, \Delta_{x_2})$	Distance to muscle (cm)	Performance index E
$(0, 0)$	1	0	610.31
$(0.4, 0.4)$	0.7788	0.57	688.68
$(0.8, 0.8)$	0.3679	1.13	1.12×10^3
$(1.2, 1.2)$	0.1054	1.70	2.97×10^3
$(1.6, 1.6)$	0.0183	2.26	5.86×10^3

7.3 Numerical Evaluation of EMMILC

In contrast to the application of standard ILC, EMMILC is now applied using the candidate set defined in Chapter 5. Essentially, the same EMMILC is used, but it is now implemented on a misaligned true plant rather than the aligned one. The error norm convergence over 20 ILC trials is shown in Figure 7.4. Similarly, Table 7.2 compares the performance of EMMILC with respect to increasing levels of misalignment. It illustrates an 853.02% reduction in the effectiveness of EMMILC when the electrode is displaced by a distance of 2.26cm from the muscle activation site.

Surprisingly, EMMILC fails to outperform the standard ILC results presented in Table 7.1. The reason lies in the selection of the candidate plant set. In Chapter 5, the plant set was designed to cover fatigue. The step response of each candidate plant is shown in Figure 7.5 a), illustrating that the lowest steady-state amplitude is 3.61×10^{-3}. This corresponds to the most fatigued model in the plant set built in Chapter 5, and serves as a starting point of misalignment. As misalignment increases, the misaligned true plants result in even smaller steady-state gains compared to the starting point, as illustrated in Figure 7.5 b). As a result, all candidate plants utilised in Chapter 5 are not available for capturing the effect of misalignment. This results in the degraded performance of EMMILC, which is similar to standard ILC.

The obvious question is how to improve the performance of EMMILC by choosing a better candidate plant set. While no single parameter within model (5.1) can directly alter the response amplitude, several parameters do influence the steady-state gain. The stiffness K_s dominates in these parameters, and has the greatest impact on modifying the steady-state gain [Charles and Hogan, 2011]. In this case, the effectiveness of EMMILC can therefore be improved by broadening the range of stiffness K_s as indicated by

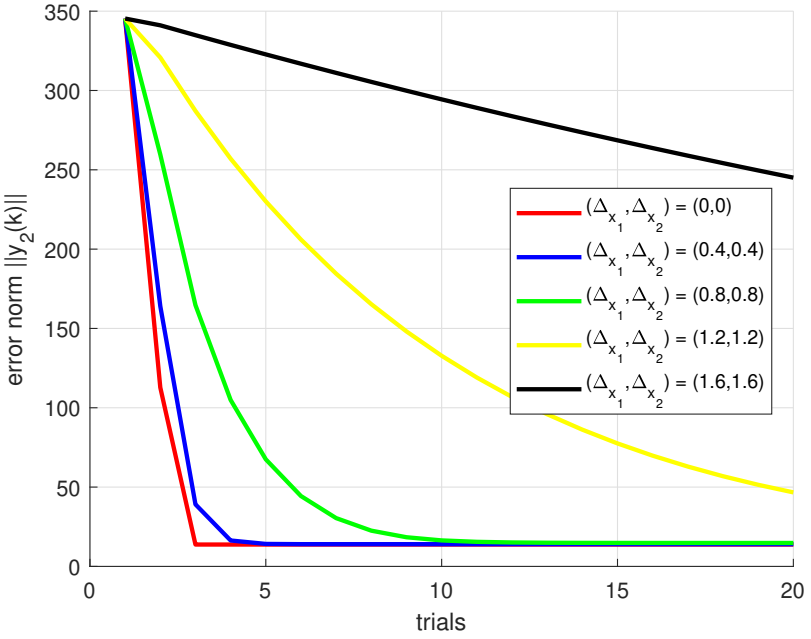

FIGURE 7.4: Convergence of error norm (EMMILC) for each trial k with respect to increasing levels of misalignment.

TABLE 7.2: Comparison of EMMILC performance for increasing levels of misalignment $(\Delta_{x_1}, \Delta_{x_2})$.

$(\Delta_{x_1}, \Delta_{x_2})$	Distance to muscle (cm)	Performance index E
$(0, 0)$	0	613.71
$(0.4, 0.4)$	0.57	689.63
$(0.8, 0.8)$	1.13	1.12×10^3
$(1.2, 1.2)$	1.70	2.96×10^3
$(1.6, 1.6)$	2.26	5.85×10^3

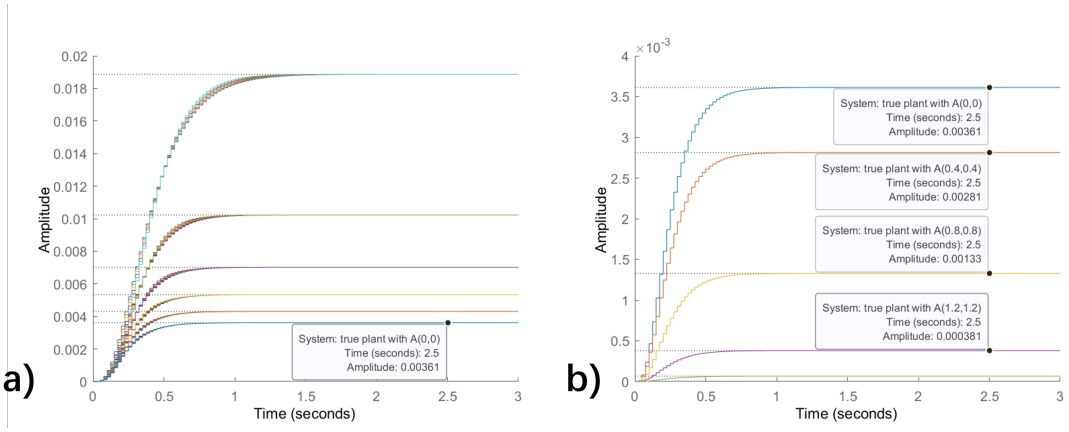

FIGURE 7.5: Step response of a): each candidate plant (including the true plant P_{p^*}), and b): the misaligned true plant with increasing levels of misalignment $(\Delta_{x_1}, \Delta_{x_2})$ shown in Table 7.2.

the values in Table 5.1, which includes more candidate plant models that have smaller

steady-state gains. To verify this, the uncertain range of K_s in Table 5.1 is expanded to $0.62 \sim 12.96$. The previous EMMILC evaluation is re-conducted using the new candidate plant set, comprising more candidate plants that have smaller steady-state gains. This yields the EMMILC error convergence results depicted in Figure 7.6, and the corresponding EMMILC performance quantified in Table 7.3. Compared with Table 7.2, this only illustrates a 355.25% reduction in the effectiveness of EMMILC when the electrode is displaced by a distance of 2.26*cm* from the muscle activation site. These results indicate that it is possible to address the misalignment by expanding the candidate plant set.

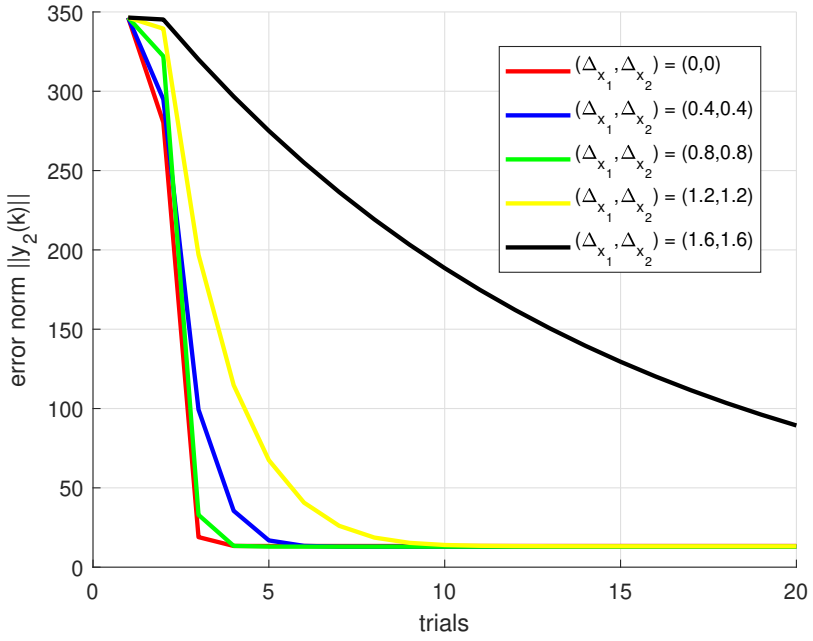

FIGURE 7.6: Convergence of error norm (EMMILC) results from the expanded candidate plant set.

TABLE 7.3: Comparison of EMMILC performance using the expanded candidate plant set.

$(\Delta_{x_1}, \Delta_{x_2})$	Distance to muscle (cm)	Performance index E
$(0, 0)$	0	869.85
$(0.4, 0.4)$	0.57	987.04
$(0.8, 0.8)$	1.13	923.41
$(1.2, 1.2)$	1.70	1.31×10^3
$(1.6, 1.6)$	2.26	3.96×10^3

7.4 Stimulation of unintended muscles

The Previous evaluation shows that numerical improvement of performance can be achieved by EMMILC. However, the practical application may experience additional

performance degradation or even system instability. This is because, as the electrode misalignment with the target activation site increases, it inevitably stimulates unintended muscles, thereby producing extra torques that disrupt the intended movements. To assess this, assume that the previous model used an extensor muscle positioned at the point $(0, 0)$ as the target activation site for modulating finger extension movement. An antagonistic flexor muscle located at $(1.6, 1.6)$ is now added in the same coordinates to induce finger flexion movement, as illustrated by Figure 7.7. The combined action of the two muscle torques results in the overall muscle torque that activates the joint, as depicted in Figure 7.8.

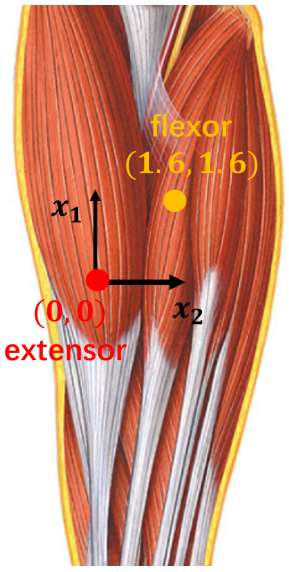

FIGURE 7.7: Defined muscle locations for finger extensor $(0, 0)$, and flexor $(1.6, 1.6)$.

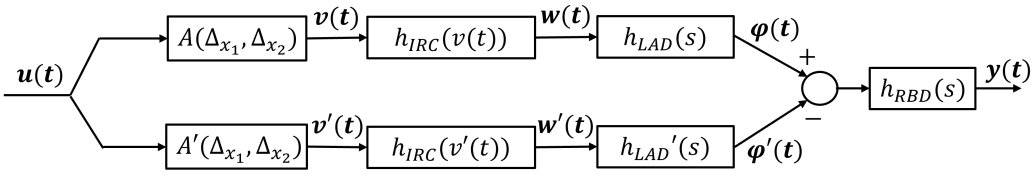

FIGURE 7.8: Modified model structure where the extensor torque $\varphi(t)$ is canceled by the counteracting torque $\varphi'(t)$, resulting from the unintended stimulation applied on the flexor muscle.

Having extended the previous model to include this new muscle, parameters are required for the flexor dynamics. Godfrey et al. [2013] demonstrated that actuating finger extensors requires more stimulation compared to finger flexors for hand impairment. This will be modeled by reducing the stiffness of the flexor muscle to $2.24 Nm/rad$, while keeping the other parameters the same as in Chapter 5. The effect is to reduce steady-state gain of the flexor, which effectively means it requires more stimulation.

A simulation will now be conducted to mimic the impact of an electrode pad that becomes gradually misaligned. To achieve this, the stimulation electrode starts at $(0, 0)$,

aligned with the extensor muscle. It then moves slowly to $(1.6, 1.6)$ as depicted in Table 7.3. As a result, the flexor muscle is increasingly activated, producing flexion torque that opposes the desired extension, as shown in Figure 7.8. The EMMILC evaluation is conducted again employing the expanded candidate plant set utilised in the previous section. Figure 7.9 illustrates the convergence outcomes, indicating that system's performance notably deteriorates as misalignment increases. This results from the increased opposing torque produced by unintentional activation of the finger flexor, creating a positive error feedback loop that degrades performance. In other words, as the stimulation site moves towards the flexor, the overall model shown in Figure 7.8 is dominated by the flexor dynamics. Consequently, the overall torque becomes negative, however, it is impossible to apply negative stimulation to remove the error feedback. Therefore, in this situation, the EMMILC cannot provide stability. Since standard ILC is a special case of EMMILC, it will also fail. This clearly reduces the practicality of deploying FES devices in home-use scenarios, as the electrode misalignment often occurs. To overcome this limitation, a more comprehensive framework is needed to enhance muscle selectivity, enabling the automatic delivery of FES to the target muscle's intended activation site.

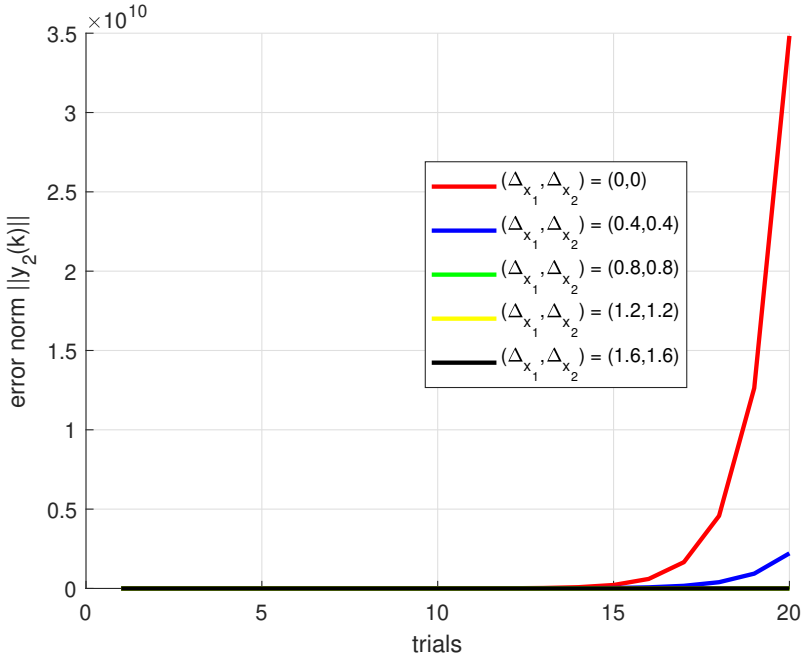

FIGURE 7.9: Convergence of error norm (EMMILC) results from the stimulation on two muscles.

7.5 Summary

This chapter illustrated how misalignment of electrodes affects system dynamics. A novel misalignment model based on underlying physics was introduced to quantitatively represent the decrease in FES caused by positional displacement. The simulation findings initially revealed that increasing misalignment drastically reduces standard ILC performance by nearly 860.17%. In comparison, while EMMILC displayed more resilience to dynamic changes as discussed in Chapter 5, it still faced a performance reduction (approximately 355.25%) as that of standard ILC when misalignment was elevated. In practice, performance degrades further due to potential stimulation of unintended muscles. This was shown in the stimulation of both finger flexor and extensor muscles. Because the stimulation point does not change, no controller can adequately compensate for extreme misalignment. For instance, if the stimulation point is associated with the flexor model, a stabilising controller would have to apply negative stimulation, which is impossible to achieve. To address this, an effective solution is to physically modify the stimulation point to minimise the activation of unintended muscles when misalignment occurs. This motivates a comprehensive approach that merges the previous EMMILC framework to compensate for electrode misalignment using electrode arrays. This will be developed in the next chapter.

Chapter 8

Application of EMMILC to Electrode Arrays

In the preceding chapter, the consequences of electrode misalignment were analysed for both standard ILC and EMMILC, showing a significant degradation in tracking accuracy with increased misalignment. This occurs due to a substantial reduction in FES, along with the possibility of inadvertently stimulating unintended muscles. As discussed in Chapter 2, single-pad FES devices struggle with spatial uncertainties and are often utilised for generating basic and slow movements involving one or two muscles. An electrode array system can potentially address this by automatically modifying the stimulation location. This chapter first develops a MIMO model and control structure for electrode arrays. To address misalignment, the analysis from Chapter 7 is then expanded to place this within the EMMILC framework of Chapter 5.

8.1 Definition of Array Geometry

Electrode arrays enable distinct muscle sites to be individually activated by separate FES channels, facilitating the tracking of more complex movements across various muscles and electrode positions. However, this also increases system complexity, transforming it from a SISO to a MIMO structure. To tackle these challenges, this section begins with introducing a mathematical model for an electrode array, expanding the single-electrode formulation (7.3) into a more comprehensive framework designed for use with an electrode array.

Consider an electrode array consisting of n pads, positioned over underlying muscles indexed as $j = 1, 2, ..., l$. Each muscle is associated with an activation site S_j defined within the same coordinate system, as depicted in Figure 8.1. At time t, the stimulation signal $u_i(t)$ is applied to the i^{th} electrode pad located at (x_1^i, x_2^i) where $i = 1, 2, ..., n$.

Based on the Coulomb's law model (7.1), the electric field delivered to the activation

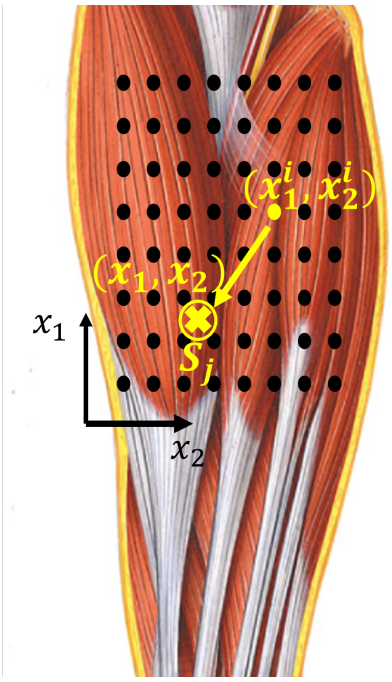

FIGURE 8.1: Coordinate system where electrode pad i stimulates muscle j defined on the surface S_j.

site of the j^{th} muscle by the stimulation $u_i(t)$, is

$$v_j(t) = \underbrace{\left(\oiint_{S_j} \frac{\kappa}{\|(x_1, x_2) - (x_1^i, x_2^i)\|^2} dx_1 dx_2 \right)}_{A_{j,i}} u_i(t). \tag{8.1}$$

The overall electric field delivered to the muscle activation site j is then the summation

$$v_j(t) = \sum_{i=1}^{n} A_{j,i} u_i(t), \tag{8.2}$$

which gives rise to the overall mapping

$$v(t) = Au(t). \tag{8.3}$$

The next step involves modeling the resultant activation of muscle j by stimulation $v_j(t)$, and computing the response of the rigid body dynamics to the cumulative effect of all l muscles. These will be introduced in the next section.

8.2 Aligned Array Dynamics

The prior model configuration shown in Figure 7.2 has been modified to fit into the nonlinear MIMO framework, facilitating its application with electrode arrays. The electric field applied to the j^{th} muscle activation point then feeds into the static function $h_{IRC,j}(v_j(t))$, which is then combined with the linear activation dynamics $h_{LAD,j}(s)$ in a cascaded manner. Each $h_{LAD,j}(s)$ block produces an active force $f_j(t)$, which is subsequently connected to a tendon network as established in [Valero-Cuevas et al., 2007]. The muscle torques are combined by the tendon network to activate each joint. Suppose the tendons are connected to m joints, then the torque produced around joint q is formulated as

$$\tau_q(t) = \sum_{j=1}^{l} R_{q,j}(y_q(t)) f_j(t), \quad q = 1, 2, ..., m, \tag{8.4}$$

where $R_{q,j}(y(t))$ is the moment arm of muscle j about joint q. This moment arm is produced by the geometry of the tendon network, and is a function of the joint angle $y(t)$. It is computed by

$$R_{q,j}(y(t)) = \frac{\partial E_j(y_q)}{\partial y_q}, \tag{8.5}$$

where $E_j(y)$ represents the tendon excursion of muscle j associated with muscle j, and anatomical parameters defined in [Soska et al., 2012]. The torque (8.4) can then be expressed as a vector

$$\tau(t) = R(y(t)) f(t), \tag{8.6}$$

where $R(y(t))$ is the tendon network matrix, which is generally nonlinear with respect to the joint angles [Soska et al., 2012]. The torque vector $\tau(t)$ then actuates the rigid body dynamics h_{RBD}, which are represented by the standard form

$$M(y(t))\ddot{y}(t) + C(y(t), \dot{y}(t)) + G(y(t)) + D(y(t), \dot{y}(t)) = \tau(t). \tag{8.7}$$

Here matrix $M(y(t))$ represents the joint inertia, $C(y(t), \dot{y}(t))$ captures Coriolis and centrifugal effects, $G(y(t))$ is gravitational torque, and $D(y(t), \dot{y}(t))$ models joint damping and friction. The overall muscle dynamics are hence illustrated by the general form shown in Figure 8.2. Note that this model structure represents a nonlinear perspective of the model forms illustrated in Figure 6.5 and Figure 7.2. Additionally, it incorporates the physiological tendon network for linking muscles to joints. Having established this general model, the next step involves developing controllers suitable for this structure.

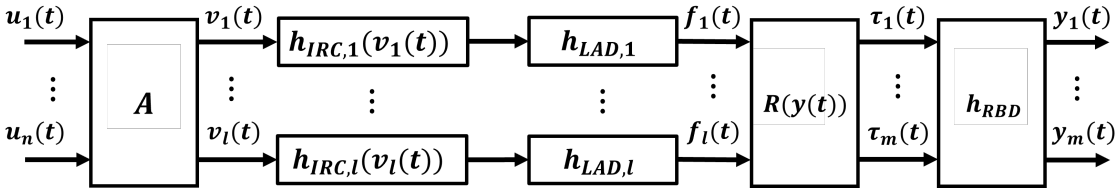

FIGURE 8.2: A general form of the MIMO dynamics of the aligned array.

8.3 Control Design for Aligned Arrays

The nonlinearities in components of the general model structure shown in Figure 8.2 makes subsequent control design challenging. However, the system is often approximated as linear in control design for the following reasons:

Assumption 1. *For finger movements, the elements within the tendon network $R(y(t))$ are predominately static scalar values [Soska et al., 2012] due to the structure of the hand and restricted range of functional movements in rehabilitation. Thus, the tendon network simplifies to a fixed matrix [Theodorou et al., 2011], denoted by R.*

Furthermore, the rigid body dynamics h_{RBD} also can be approximated as linear over restricted ranges, as shown next

Assumption 2. *The rigid body dynamics (8.7) can be regarded as linear during planar movements when $G(y(t))$ is fixed and the angular velocity remains sufficiently low, resulting in linear inertia $M(y(t))$ and Coriolis $C(y(t), \dot{y}(t))$ matrices. Under the same condition, the friction and damping term $D(y(t), \dot{y}(t))$ can be assumed to be piecewise linear, as supported by experimental modeling results from stroke participants identified under constrained planar motion [Freeman et al., 2009a]. These justify a linear formulation of the overall rigid body dynamics h_{RBD}.*

Building on these two assumptions, Figure 8.2 is modified to

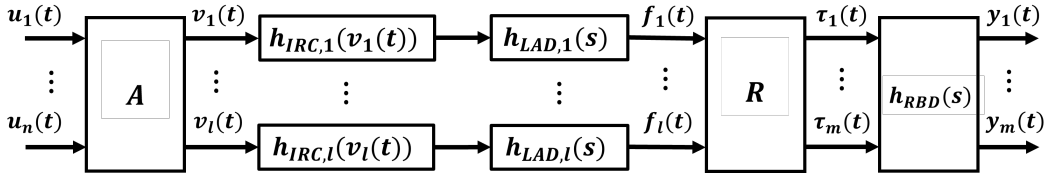

FIGURE 8.3: The simplified form of the aligned array dynamics with fixed matrix R and linear $h_{RBD}(s)$.

This is one possible way to interpret the model structure (see Figure 7.2) for practical control design. The MIMO system illustrated in structure (8.3) can therefore be simplified to

$$P_p : u \to y : y = h_{RBD} R h_{LAD} h_{IRC} A u, \tag{8.8}$$

with the same structure of h_{IRC}, h_{LAD} dynamics as used in Chapter 5, the components can be chosen to take the following forms

$$y = [y_1(t), y_2(t), ..., y_m(t)]^\top, \quad u = [u_1(t), u_2(t), ..., u_n(t)]^\top,$$

$$h_{RBD}(s) = \begin{bmatrix} \frac{1}{I_{s,1,1}s^2+B_{s,1,1}s+K_{s,1,1}} & \cdots & \frac{1}{I_{s,1,m}s^2+B_{s,1,m}s+K_{s,1,m}} \\ \vdots & \ddots & \vdots \\ \frac{1}{I_{s,m,1}s^2+B_{s,m,1}s+K_{s,m,1}} & \cdots & \frac{1}{I_{s,m,m}s^2+B_{s,m,m}s+K_{s,m,m}} \end{bmatrix}, R = \begin{bmatrix} R_{1,1} & R_{1,2} & \dots & R_{1,l} \\ R_{2,1} & R_{2,2} & \dots & R_{2,l} \\ \vdots & \vdots & \ddots & \vdots \\ R_{m,1} & R_{m,2} & \dots & R_{m,l} \end{bmatrix},$$

$$h_{LAD}(s) = \begin{bmatrix} \frac{\omega_{n,1}^2}{s^2+2\omega_{n,1}s+\omega_{n,1}^2} & 0 & \dots & 0 \\ 0 & \frac{\omega_{n,2}^2}{s^2+2\omega_{n,2}s+\omega_{n,2}^2} & \dots & 0 \\ \vdots & \vdots & \ddots & \vdots \\ 0 & 0 & \dots & \frac{\omega_{n,l}^2}{s^2+2\omega_{n,l}s+\omega_{n,l}^2} \end{bmatrix},$$

$$h_{IRC} = \begin{bmatrix} h_{IRC,1} & 0 & \dots & 0 \\ 0 & h_{IRC,2} & \dots & 0 \\ \vdots & \vdots & \ddots & \vdots \\ 0 & 0 & \dots & h_{IRC,l} \end{bmatrix}, \quad A = \begin{bmatrix} A_{1,1} & A_{1,2} & \dots & A_{1,n} \\ A_{2,1} & A_{2,2} & \dots & A_{2,l} \\ \vdots & \vdots & \ddots & \vdots \\ A_{l,1} & A_{l,2} & \dots & A_{l,n} \end{bmatrix},$$

where $h_{IRC,j}$ are approximated as constants as detailed in Chapter 5. The array matrix A has elements $A_{j,i}$ which are defined in (8.1).

Since the model (8.8) is linear, the design of MIMO ILC can be conducted directly. Nevertheless, as shown in Section 7.4, the input $u(t)$ must remain positive. Therefore, it is strategical to activate electrode pads that align with the target muscles, thereby facilitating the intended motion. This can be achieved by the following design

Remark 1. *Suppose each of the m joint angles is primarily actuated by a single muscle, and the activated electrode pads are chosen to stimulate each of these muscles independently. Then the matrix R contains only a single non-zero element in each row and column. Similarly, matrix A only has a single non-zero element in each row, and a single non-zero element in each column corresponding to each activate electrode pad. The system dynamics are hence decoupled, and an independent controller can be designed for each stimulation channel.*

Without being decoupled, this MIMO system (8.8) can still be controlled, but controller design poses an extra challenge to achieve precise task movements. Since it has four states, it can be expressed in state-space form, $p = (A_p, B_p, C_p, D_p)$, with elements $A_p \in \mathbb{R}^{4m\times 4m}$, $B_p \in \mathbb{R}^{4m\times n}$, $C_p \in \mathbb{R}^{m\times 4m}$, and $D_p \in \mathbb{R}^{m\times n}$. These elements can be inserted into (5.2) over a time period $t = 1, 2, ..., N$ to yield the lifted plant $P_{\hat{p}}$. In this case, any MIMO ILC methods [Kutlu et al., 2016a; Soska et al., 2012] can be employed to determine the update. The EMMILC approach used in Chapter 5 can also be applied by designing a candidate plant set that covers the uncertain parameters in model

(8.8). However, a key component of uncertainty is misalignment, and Chapter 7 has illustrated that electrode misalignment significantly decreases the convergence rate, a consequence that also occurs for arrays. To tackle this, the next section begins by defining the dynamics of a misaligned array, which are essential for the subsequent control design.

8.4 Misaligned Array Dynamics

The misalignment in the array structure results from both translational $z = (\Delta_{x_1}, \Delta_{x_2})$ and rotational θ deviations, as defined in Figure 8.4 a). Following the framework of the

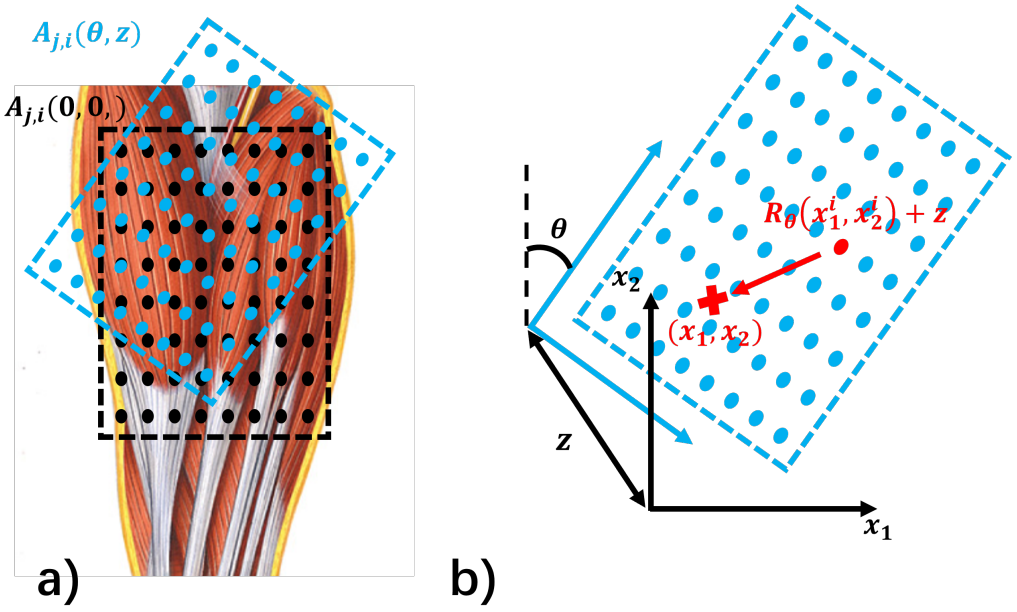

FIGURE 8.4: Electrode array misalignment illustrated by a): rotation θ and translation z. b): misaligned array geometry.

misaligned model (7.2), the field delivered to muscle j, from electrode pad i, is reduced to

$$F_j(t) = \underbrace{\left(\oiint_{S_j} \frac{\kappa}{\|(x_1, x_2) - (R_\theta(x_1^i, x_2^i) + z)\|^2} dx_1 dx_2 \right)}_{A_{j,i}(\theta,z)} u_i(t), \tag{8.9}$$

where $R_\theta = \begin{bmatrix} \cos\theta & -\sin\theta \\ \sin\theta & \cos\theta \end{bmatrix}$ is a 2D rotation matrix, and κ is Coulomb's constant. The misaligned array geometry is illustrated by Figure 8.4 b). The contribution to the j^{th}

muscle's h_{IRC} block from electrode pad i hence reduces from $u_i(t)$ to

$$v_j(t) = \frac{F_j(t)}{A_{j,i}} = \underbrace{\left(\iint_{S_j} \frac{\|(x_1, x_2) - (x_1^i, x_2^i)\|^2}{\|(x_1, x_2) - (R_\theta(x_1^i, x_2^i) + z)\|^2} dx_1 dx_2 \right)}_{A_{j,i}(\theta,z)} u_i(t). \tag{8.10}$$

If there is no misalignment (e.g., $\theta = 0, z = (0,0)$), then $A_{j,i}(\theta, z) = 1$.

The total input delivered to muscle activation location j, therefore is

$$v_j(t) = \sum_{i=1}^{n} A_{j,i}(\theta, z) u_i(t), \tag{8.11}$$

which therefore yields the overall array mapping

$$v(t) = A(\theta, z) u(t), \tag{8.12}$$

where the fixed matrix $A(\theta, z) \in \mathbb{R}^{l \times n}$ has elements $A_{j,i}(\theta, z)$ defined in (8.10).

Consequently, the misaligned true model is

$$P_{p^*} : u \to y : y = h_{RBD} R h_{LAD} h_{IRC} A(\theta, z) u, \tag{8.13}$$

with components defined in Section 8.2. These can be approximated by linear forms as was done in Section 8.3. This model will be used in the next section to formulate an ILC scheme capable of automatically addressing the misalignment (θ, z).

8.5 Control Design for Misaligned Arrays

To address misalignment, the stimulation sites must be adjusted to "realign" with the target muscles if the misalignment (θ, z) is known. To do this, suppose an ILC update C_c is designed for the aligned plant P_p with form (8.8). Suppose this true plant is now misaligned by (θ, z), but a mapping $T(\theta, z)$ is now added in the controller to realign the system (8.13). At ILC trial k, the ILC update applied with the misaligned system (8.13) then becomes

$$\begin{aligned} C_c : y \mapsto u : u_2(k) &= T(\theta, z) v(k), \\ v(k+1) &= v(k) - L y_2(k), \end{aligned} \tag{8.14}$$

where the observed signals (u_2, y_2) are defined by the closed-loop system shown in Figure 3.2. This update (8.14) is identical to (5.4), but does not include the realignment mapping $T(\theta, z)$. This mapping $T(\theta, z)$ aims to cancel the misaligned effect caused by $A(\theta, z)$. To achieve this, $T(\theta, z)$ is chosen to minimise the difference between the aligned system (8.8) and the realigned true plant. This can be expressed by the optimisation

problem

$$\begin{aligned}\min_{T(\theta,z)} &\|h_{RBD}Rh_{LAD}h_{IRC}A - h_{RBD}Rh_{LAD}h_{IRC}A(z,\theta)T(\theta,z)\| \\ &\leq \|h_{RBD}Rh_{LAD}h_{IRC}\| \min_{T(\theta,z)} \|A - A(z,\theta)T(\theta,z)\|.\end{aligned} \tag{8.15}$$

By solving $\min_{T(\theta,z)} \|A - A(z,\theta)T(\theta,z)\|$, the realignment mapping $T(\theta,z)$ then has the form

$$T(\theta,z) = A(\theta,z)^{\dagger}A, \tag{8.16}$$

where the term $A(\theta,z)^{\dagger}$ has the effect of physically realigning the stimulation sites if (θ,z) are known. The overall closed-loop structure of the ILC update (8.14) is illustrated by Figure 8.5, where $P_{\hat{p}^*}$ is the misaligned true plant (8.13) in the lifted form.

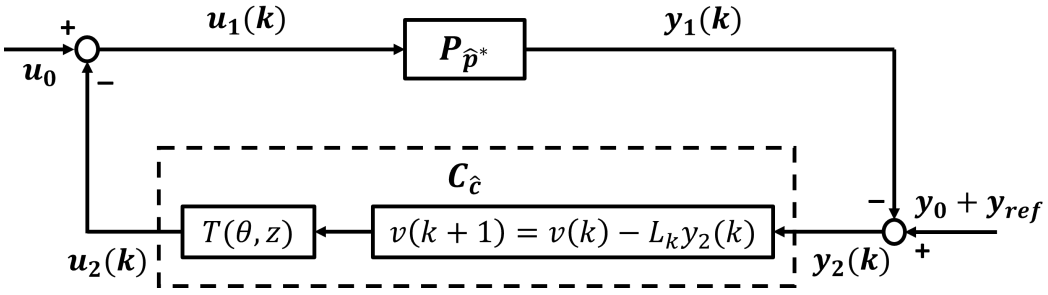

FIGURE 8.5: The structure of the realigned ILC controller applied with the misaligned true plant.

This realignment mapping (8.16) can also be applied to the single-pad system (7.6) with misalignment term $A(\Delta_{x_1},\Delta_{x_2})$. This can be achieved by modifying $T(\theta,z)$ to $T(\Delta_{x_1},\Delta_{x_2}) = A(\Delta_{x_1},\Delta_{x_2})^{-1}$. The ILC update (8.14) then realigns the system (7.6) by yielding $A(\Delta_{x_1},\Delta_{x_2})^{-1}A(\Delta_{x_1},\Delta_{x_2}) = A(0,0) = 1$.

Having defined this realignment approach, the next step is to show how the term $A(\theta,z)^{\dagger}$ can physically modify the stimulation site to eliminate the effect of misalignment in the true plant. This realignment action will be demonstrated by performing a simple case study using standard ILC in the next section.

8.6 Simulation of Standard ILC with Realignment

Consider an 8×8 array ($n = 64$), with each electrode pad indexed by $i = 1,2,...,64$. Suppose this array is placed over $m = 2$ underlying muscles, indexed by $j = 1,2$. These muscles include the wrist extensor muscle positioned at $(2.2,2.2)$ and finger extensor muscle at $(7,7)$, as illustrated by Figure 8.6 a). Following the design approach in Remark 1, each target muscle primarily actuates a single joint angle, indexed by $q = 1,2$, as shown in Figure 8.7 a). Two active electrode pads positioned at $(7.5,7.5)$ and $(2,2)$

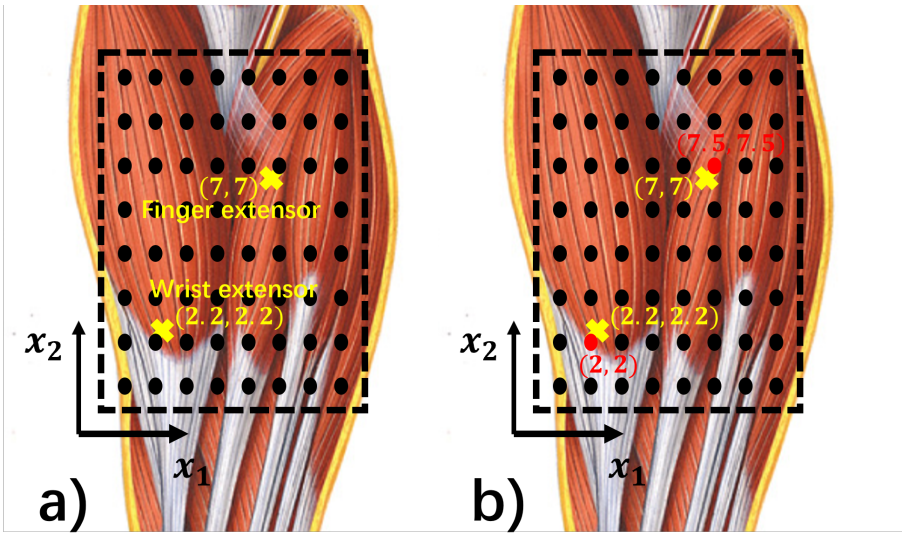

FIGURE 8.6: The 8×8 array geometry [black dots] with a): two underlying muscles [yellow cross]. b): the most aligned electrode pad [red dot] chosen to stimulate each muscle independently.

that mostly closely align with these two muscles are chosen to stimulate each muscle independently, as illustrated by Figure 8.6 b). The desired hand motion, is defined by the two joint angle references depicted in Figure 8.7 b).

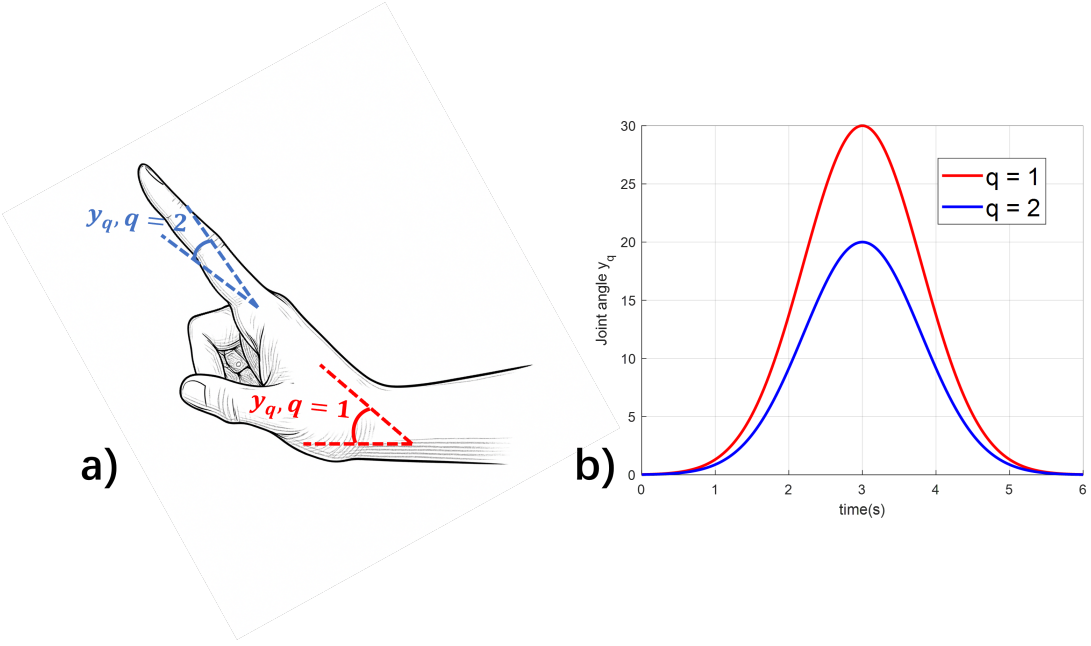

FIGURE 8.7: The joint angles y_q characterised by a): wrist extension when $q = 1$ and finger extension when $q = 2$, which are independently actuated. b): the reference signal described by these two joint angles.

Having defined an aligned array, the next step is to generate an aligned model for it. Using the positions shown by Figure 8.7 b), the stimulation $v_j(t)$ delivered to muscle j,

given by electrode pad i, is computed using (8.1). This then yields the overall mapping $v(t) = Au(t)$, where the mapping A defines the stimulation given by each of the 64 pads. Because only the two electrode pads shown in Figure 8.7 b) are activated, the aligned model A is then computed as

$$A = \begin{bmatrix} 0 & 0 & \cdots & 0 & \overbrace{0.71}^{10^{\text{th}}\text{ electrode pad}} & 0 & \cdots & 0 & 0 & 0 & \cdots & 0 & 0 \\ 0 & 0 & \cdots & 0 & 0 & 0 & \cdots & 0 & \underbrace{0.99}_{47^{\text{th}}\text{ electrode pad}} & 0 & \cdots & 0 & 0 \end{bmatrix}, \quad (8.17)$$

which is also decoupled because each active electrode pad was selected to actuate each muscle independently, as defined in Figure 8.7 b). The input $v(t)$ then feeds into the h_{IRC} block of the aligned system P_p in the form (8.8), where the parameters in h_{RBD}, h_{LAD} and h_{IRC} are equal to the values used in Section 7.4. To simplify the implementation, the decoupled tendon matrix R is defined as $R = \begin{bmatrix} 1 & 0 \\ 0 & 1 \end{bmatrix}$.

Following the establishment of the aligned system, the next step is to mimic the array misalignment. Suppose this array is now misaligned by $\theta = -30^\circ$ and $z = (-1.6, 1.6)cm$, as illustrated by Figure 8.8. The misaligned array model $A(\theta, z)$ can be computed using

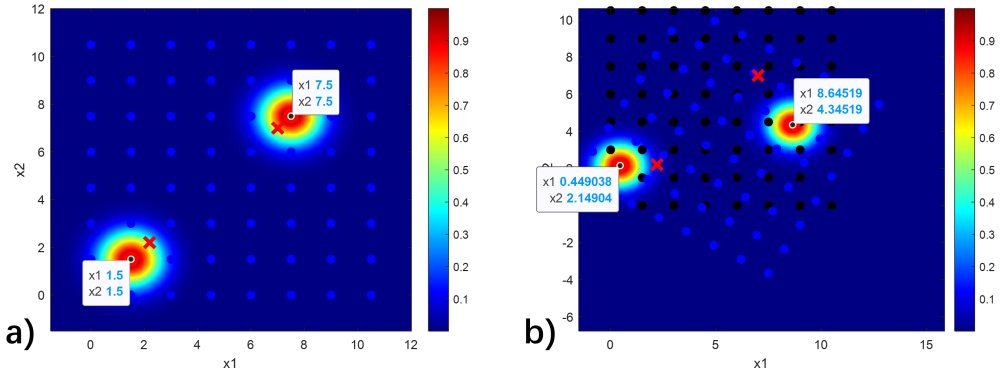

FIGURE 8.8: The coloured map (larger colour number indicates larger $A(\theta, z)$) in coordinates system (x_1, x_2)cm with a): aligned array where the stimulation [coloured area] is delivered to each target muscle [red cross]. b): misaligned array with new stimulation sites.

(8.10)-(8.12)

$$A(\theta,z) = \begin{bmatrix} 0 & 0 & \cdots & 0 & \overbrace{0.57}^{7^{\text{th}}\text{ electrode pad}} & 0 & \cdots & 0 & 0 & 0 & \cdots & 0 & 0 \\ 0 & 0 & \cdots & 0 & 0 & 0 & \cdots & 0 & \underbrace{0.23}_{52^{\text{th}}\text{ electrode pad}} & 0 & \cdots & 0 & 0 \end{bmatrix}, \tag{8.18}$$

which then yields the misaligned true plant P_{p^*} with form (8.13), where the components h_{RBD}, h_{LAD}, R, and h_{IRC} remain the same as those of the aligned model.

Prior to testing the realignment controller, standard ILC is applied without realignment to demonstrate the impact of misalignment on the tracking performance when using an electrode array. To achieve this, the previously defined aligned plant P_p is now lifted and used to design a standard ILC controller, employing the identical update method as it used in Chapter 7 without realignment. This yields the tracking result over 20 trials illustrated by Figure 8.9, demonstrating an extremely slow convergence rate for each joint angle. The tracking error merely decreases to 99.4% of its initial value for wrist extension, and 51.4% of its initial value for finger extension. Figure 8.10 presents the tracking plots updated over 20 trials, illustrating that the error has not reached its lowest feasible value by the end of all trials. This results from the misaligned mapping $A(\theta,z)$ with elements shown in (8.18), which significantly reduces the stimulation received by the target muscles.

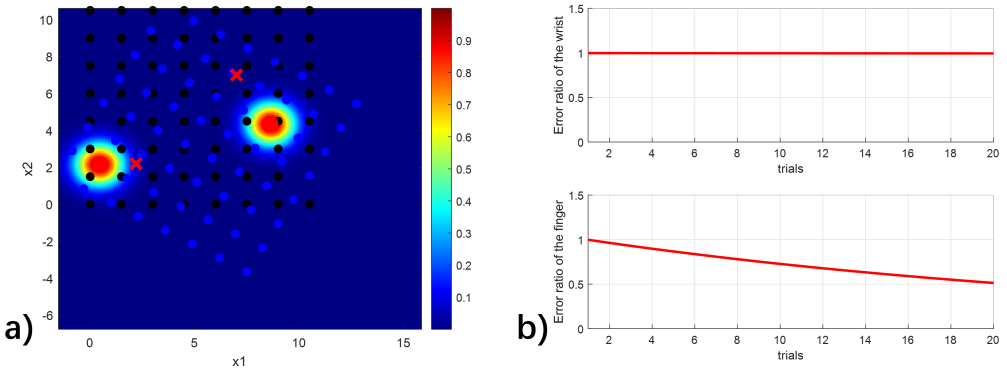

FIGURE 8.9: Illustration of a): misaligned stimulation sites and target muscles in coordinates system (x_1, x_2)cm. b): ILC error convergence for tracking each joint angle.

This can be addressed by applying the realignment mapping $T(\theta,z) = A(\theta,z)^{\dagger}A$, where the term $A(\theta,z)^{\dagger}$ is intended to mitigate the misaligned effect $A(\theta,z)$ of the true dynamics (8.13) by ensuring $A(\theta,z)^{\dagger}A(\theta,z) \approx I$. This aims to significantly reduce the difference between the misaligned and aligned dynamics, and yield $P_{p^*} \approx P_p$. Using

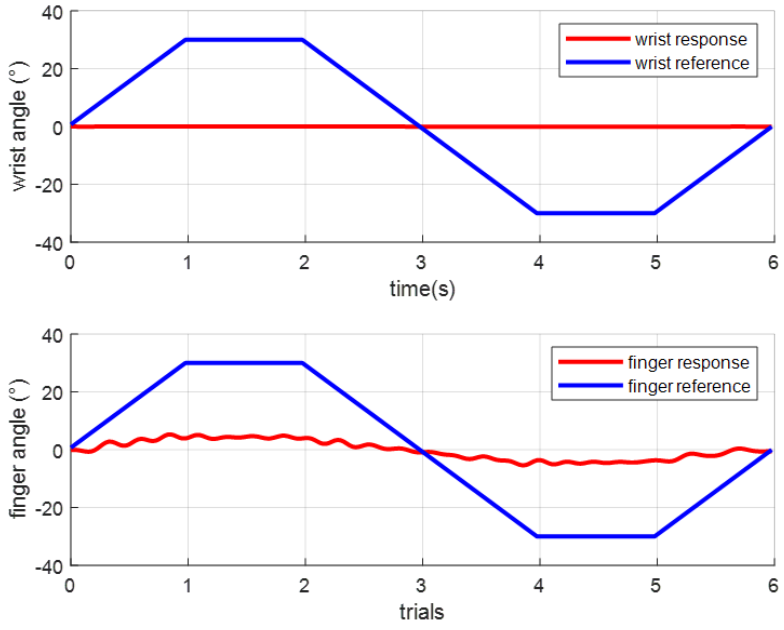

FIGURE 8.10: Tracking plots of the standard ILC update over 20 trials without realignment part.

the same ILC settings, the tracking result over 20 trials is shown in Figure 8.11, illustrating that the tracking error decreases to 8.4% of the initial error for both the wrist and finger joints. This performance considerably outperforms the previous case by applying the mapping $T(\theta, z)$, which physically realigns the stimulation sites, as illustrated by Table 8.1. With realignment term $T(\theta, z)$ applied, the spatial error is decreased by 78.1% for the wrist extensor muscle, and 76.4% for the finger extensor muscle. The misaligned effect was not completely canceled. Because there is no electrode pad in the misaligned array whose position exactly matches the active electrode pads in the aligned array, as shown by comparing Figure 8.8 a) and b). As a result, the mapping $T(\theta, z)$ can physically realign the stimulation site by only selecting the electrode pad that is spatially closest to the intended stimulation site. Although this does not fully resolve the misalignment issue, it minimises its impact.

TABLE 8.1: The true stimulation sites with or without realignment action $T(\theta, z)$.

Aligned stim sites	Realignment?	True stim sites	Distance (cm)
$(1.5, 1.5)$ and $(7.5, 7.5)$	Without $T(\theta, z)$	$(0.45, 2.15)$ and $(8.65, 4.35)$	1.23 and 3.35
	With $T(\theta, z)$	$(1.75, 1.40)$ and $(6.80, 7.14)$	0.27 and 0.79

Although realigned stimulation accelerates convergence, the standard ILC update (8.14) may still fail due to physiological variations in the misaligned true plant (8.13). For instance, if the muscle becomes more and more fatigued, which can be captured by the increasing the value of K_s in the h_{RBD} block. To model this effect, the K_s value of the unknown misaligned plant P_{p^*} implemented before is doubled. The previous

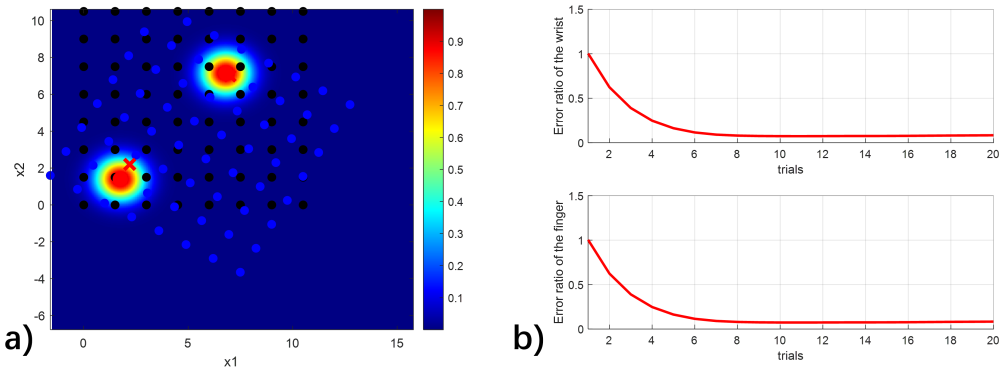

FIGURE 8.11: Illustration of a): **realigned** stimulation sites and target muscles in coordinates system (x_1, x_2)cm. b): ILC error convergence for tracking each joint angle.

standard ILC is now repeated on this misaligned and fatigued true plant, producing the error convergence results across 20 trials shown in Figure 8.13. Figure 8.12 presents the tracking plots over 20 trials for both joints utilising the standard ILC update (8.14). In this case, Figure 8.12 a) demonstrates that the implementation of the realignment ILC (8.14) has effectively modified the stimulation points, ensuring initial convergence.Nevertheless, Figure 8.12 b) indicates that physiological changes, such as fatigue, can significantly degrade tracking performance after initial convergence. This necessitates the integration of a realignment controller with the EMMILC method to concurrently address various model uncertainties.

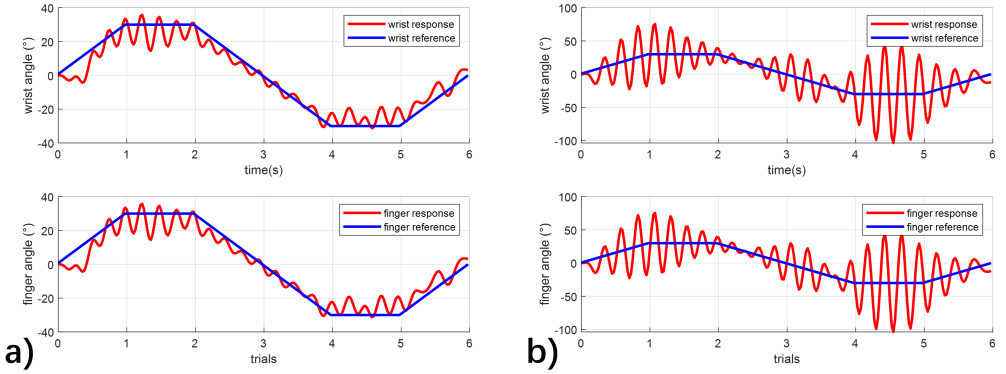

FIGURE 8.12: Tracking plots of the standard ILC update (8.14) over a): 10 trials for initial convergence and b): 20 trials for long-term convergence.

The results indicate that despite realigning the stimulation sites, the tracking error still diverges. This results from the mismatch between the unknown true plant and the plant model used in ILC design. This limitation can be effectively addressed by employing EMMILC with a comprehensive candidate plant set, which captures the true dynamics. Therefore, the next step involves broadening the previous candidate plant set to include different misaligned models, thereby allowing compensation for both physiological variations and spatial uncertainties.

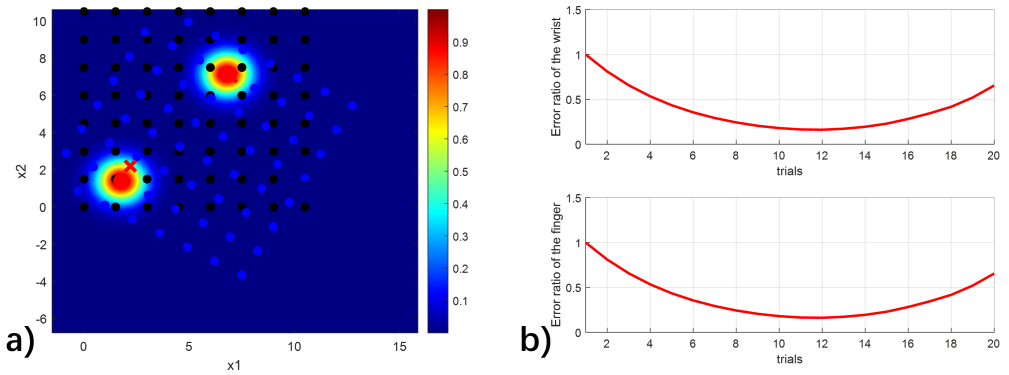

FIGURE 8.13: Illustration of a): **realigned** stimulation sites and target muscles in coordinates system (x_1, x_2)cm. b): ILC error convergence with the misaligned and also fatigued true plant.

8.7 Simulation of EMMILC with Realignment

Using realignment mapping $T(\theta, z)$ requires the misalignment (θ, z) to be known. However, the misaligned true plant is unknown in practice. This can be addressed by expanding the previous candidate plant set, adding more candidate plant models (8.13) corresponding to possible values of misalignment (θ, z), where $z = (\Delta_{x_1}, \Delta_{x_2})$. To establish these additional plants, the varying range of the misalignment (θ, z) is required. Taking the identical set of physiological parameters as used in Chapter 5, the range of misalignment parameters (θ, z) shown in Table 8.2 is added. Following the same EMMILC design procedure as detailed in Chapter 4, this then produces a new set of candidate plants. Then, a simulation is performed to demonstrate the effectiveness of this expanded candidate set. Using the same true plant from the previous section, which is misaligned and also fatigued, the tracking results using realignment EMMILC over 20 trials are shown in Figure 8.15. The tracking error for each muscle was decreased to 3.7% of its initial value after 3 iterations. The tracking plots of realignment EMMILC over 20 trials for both joints are shown in Figure 8.14.

These results demonstrated that EMMILC outperformed the standard ILC for electrode arrays. Additionally, it verified that EMMILC did not assume any limited uncertainty in design procedure. The misaligned stimulation site was immediately realigned after the first trial. The results in Figure 8.13 demonstrate that, in comparison to traditional ILC outcomes, EMMILC has been validated in effectively addressing physiological changes and spatial uncertainties. This raises the potential for employing EMMILC and electrode arrays to tackle practical issues in the upper-limb rehabilitation.

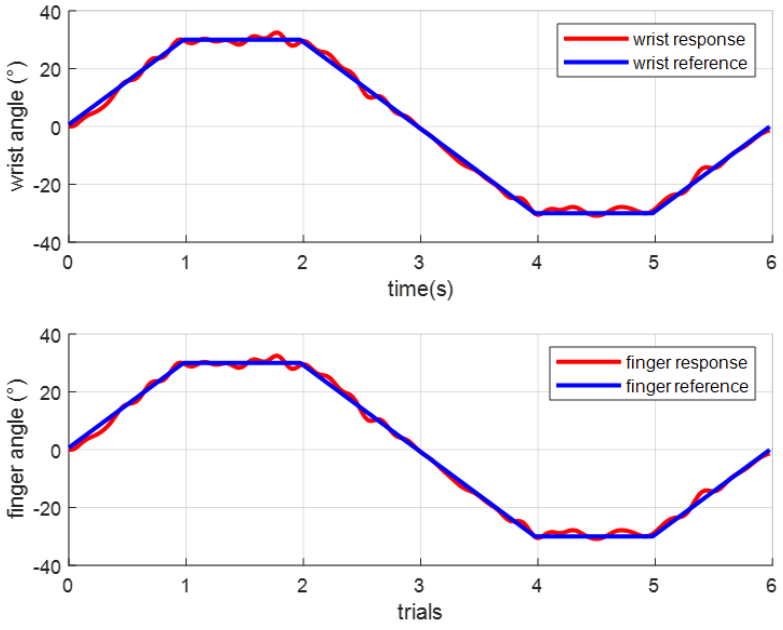

FIGURE 8.14: Tracking plots of the realignment EMMILC for wrist and finger joints over 20.

TABLE 8.2: Values of hand parameters for the uncertain true plant.

Parameter	Symbol	Uncertainty range	Unit
IRC constant	h_{IRC}	0.0117	N/A
Natural frequency	ω_n	9.4248	rads/s
Stiffness	K_s	$0.62 \sim 3.24$	Nm/rad
Damping	B_s	0.128	Nms/rad
Inertia	I_s	$0.0007 \sim 0.00612$	Nms^2/rad
Rotation	θ	$0 \sim 30$	degree(◦)
Horizontal shift	Δ_{x_1}	$0 \sim 1.6$	cm
Vertical shift	Δ_{x_2}	$0 \sim 1.6$	cm

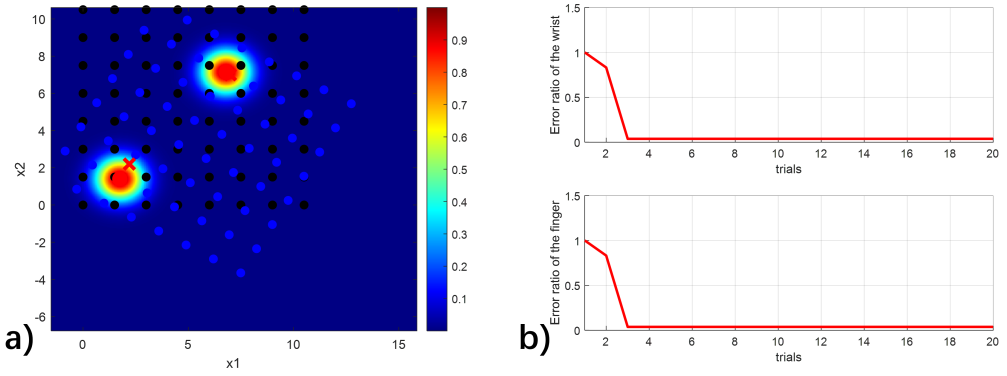

FIGURE 8.15: Illustration of a): **realigned** stimulation sites and target muscles in coordinates system (x_1, x_2)cm. b): EMMILC error convergence with the misaligned and also fatigued true plant.

8.8 Summary

This chapter systematically investigated the application of ILC to electrode array systems. Starting from the single pad aligned model, it generalised an aligned model for arrays and corresponding control design. Subsequently, the misaligned array system was modeled to capture the spatial errors. To address misalignment, a mapping strategy was derived to physically realign the stimulation sites with the target muscles. Then, simulations were performed to compare standard ILC against EMMILC with array misalignment and physiological variations. The outcomes indicated that the performance of standard ILC deteriorated significantly in the presence of misalignment and muscle fatigue. In contrast, EMMILC leveraged a set of candidate models representing uncertain dynamics, reducing the tracking error to less than 3.7% within 3 trials. These results showed that EMMILC consistently outperformed standard ILC in the control of an array system with uncertainties. This offers EMMILC the potential to tackle practical challenges in upper-limb FES rehabilitation.

Chapter 9

Conclusions and Future Work

Surveys of people with stroke show that existing FES commercial devices cannot achieve the intensive and goal-oriented task training that is needed for effective stroke rehabilitation. Users report that their devices take a long time to set up and are often inconvenient for home use. FES electrode arrays can potentially address this problem by providing better muscle selectivity and enabling suitable stimulation sites to be located and appropriately controlled in an automatic, rapid fashion. However, the currently available control methods for FES arrays are relatively crude: they take a long time to set-up, are predominantly open-loop, and none are capable of adapting to varying physiological dynamics or variation in alignment.

The aim of this programme of research was to develop a control framework for FES electrode arrays that enables complex gestures to be accurately achieved without excessive set-up procedure. This novel approach developed in this thesis combines two ingredients:

- a multiple-model adaptive architecture that has previously been shown to be effective using a single electrode pad and an isometric task, and
- an update procedure that learns from previous attempts at the task, that has been successful in clinical trials, again using single pad electrodes.

The major contribution has been to develop and evaluate a comprehensive design approach for multiple model ILC. This was evaluated on a key problem in stroke rehabilitation. Multiple models were fitted by capturing underlying wrist dynamics which linked FES and induced movements together. These models allowed ILC updates to learn from previous experience to perform fast and precise tracking tasks. To achieve an adaptive architecture, Algorithm 1 minimised the number of required models to establish a candidate plant set, and a switching algorithm automatically selected the ILC controller corresponding to one of the models that best explained the measured input

and output data. Experiments were performed on healthy subjects, and initial results using single-pad electrodes showed that the tracking error was reduced to 20% of its initial value within 5 trials, and maintained the same level of error in the presence of pronounced muscle fatigue. However, tracking accuracy in practical applications could be decreased by the issue of electrode misalignment, which had not been resolved by other multiple-model approaches.

In response to this issue, a model of single-pad electrode misalignment was then developed, focusing on the distribution of the electric field. Rigorous simulations on a simplified linear model demonstrated that even slight misalignment could cause stimulation of unintended muscles, which significantly destabilised both conventional ILC and EMMILC. These results then highlighted the critical need for electrode array, which aimed to adaptively activate the selected muscles.

To apply selective stimulation, the EMMILC approach was extended to electrode arrays for the first time. It began by establishing an aligned MIMO model that generalised single-electrode dynamics to electrode array systems, clearly defining the spatial relationships between electrodes and activated muscles. Array misalignment was then investigated by deriving explicit MIMO dynamics for rotational and translational misalignment. To address misalignment, this research introduced a physical realignment strategy, dynamically correcting stimulation sites via solving an optimization problem. Numerical evaluation was implemented on fatigued and misaligned array system. Results showed that, compared to standard ILC, EMMILC applied with array realignment term reduced tracking errors to less than 3.7% of initial levels within three trials, and the spatial errors was decreased by 78%. These results effectively conformed EMMILC's capability of handling misalignment and physiological uncertainties.

Current research has established the EMMILC framework's capability to reduce tracking error under muscle fatigue and electrode misalignment, yet its evidence remains insufficient: experimental validation to date involves healthy participants with single-pad stimulation, whereas array misalignment and MIMO control have only been examined numerically under simplified single-DOF tasks. The modeling and control design rely heavily on low-dimensional linear approximations. An electrode array hardware is designed in Appendix B. However, this hardware platform is still at the laboratory prototype stage, being wired, unminiaturised, lacking long-term evaluations for reliability and fault tolerance. Consequently, it has not yet demonstrated practical effectiveness and safety. Virtual electrode identification still follows a sequential activating procedure, increasing unnecessary set-up time and offering no optimisation-based selection strategy. The compatibility of both EMMILC approach and array hardware with individuals, across different days, and in the face of extensive physiological variations (e.g., skin-electrode impedance) has not been established. This results in conservative design of candidate plant sets that lack satisfactory robustness to cover a wider uncertainty space. Furthermore, the application of EMMILC approach can in principle be

extended to diverse populations and broader biomedical fields, allowing for identification tests to be completely removed for any healthy subjects or stroke patients in clinical trials. Experimental validation has so far been limited to upper-limb scenarios; extension to lower-limb or gait contexts with faster, coupled dynamics is untested. These constraints restrict the current evidence base and show the gap between the current research prototype and clinical, home-based upper-limb FES array systems.

9.1 Future Work

To achieve broader applications, future research will aim to enhance the existing EMMILC approach, which will facilitate the intensive and goal-oriented upper-limb FES training tasks using array systems. The effectiveness of EMMILC framework will then be confirmed by performing extensive clinical evaluations with both healthy participants and stroke patients. This can be divided into several steps:

1. This research has demonstrated the effectiveness of the EMMILC approach in addressing fatigue and array misalignment. The next stage is to design a home-use electrode array FES system to further verify the clinical feasibility and reliability of EMMILC in practical applications. As the first step, a hardware platform prototype has been preliminarily designed and initially validated (see Appendix B), comprising an 8×8 electrode array, a high-voltage analogue multiplexer switching board, and a Leap Motion depth camera for joint angle measurement. Experimental results show that the platform can achieve high spatial selectivity and reliably identify target muscles under repositioning. Future work will focus on translating this array system prototype into a clinically viable home-based FES platform by further miniaturising the hardware and reducing power consumption, ultimately facilitating wireless operation. In the mean time, investigate the long-term safety and reliability, focusing on automatic fault detection with fail-safe shutdown. To overcome the inefficiency of sequential virtual electrode activation, an optimisation or learning based active search methods will be developed to select optimal electrodes and identify target muscles in a more efficient way. Subsequent user-centered research will quantify workflow and usability by measuring setup identification time and automated realignment following array repositioning. Comparative hardware trials against standard ILC and EMMILC will finally characterise convergence speed and robustness to physiological variations, thereby guiding subsequent research towards effective home-based FES system. Progress in this point means turning the laboratory prototype system into a clinical (ultimately wireless) platform that non-expert users can set up quickly at their home. These aims to confirm that it is possible to remove the need for identification tests, and therefore is a solid foundation for future clinical translation.

This is an intermediate-duration project aimed at comprehensively improving the hardware system.

2. Using this hardware platform, the clinical feasibility of implementing EMMILC will be completed by performing a series of comprehensive experiments with electrode array for both healthy participants and upper-limb stroke patients. These tests involve activating each virtual electrode to identify the physiological dynamics of every underlying muscles. Each underlying muscle model will also be expanded to a model set based on the possible range of misalignment variables (θ, z). The combined candidate plant set will then be experimentally tested using the designed hardware platform to confirm EMMILC's clinical capability of handling both physiological variation and array misalignment. The progress means to deliver rapid, stable error convergence when moved from healthy subjects to a stroke patients, confirming the feasibility of the EMMILC framework in practical FES training. this should be achievable in the medium term to organise more experiments.

3. An important research direction is to investigate whether a single candidate model set is feasible for all participating subjects. This involves identifying the underlying hand models across different days for individuals with varying ages, genders, and degrees of upper-limb impairments. If the identified models exhibit notable differences among subjects, they will be incorporated to expand the candidate plant set. The ultimate progress is to eliminate the necessity of model identification for any subject, thereby enabling comprehensive automation of FES-based upper-limb rehabilitation suitable for clinical and home environments. This should be an intermediate-duration project to perform multiple tests.

4. To support functional movements involving a variety of muscles and joints, EMMILC approach will be expanded for controlling multi-degree-of-freedom movements. This can be achieved by experimentally identifying MIMO models that characterise interactions among multiple joints and muscles. Data collection protocols must systematically excite the dynamics to capture full coupling effects and muscle synergies accurately. Then, update candidate models to incorporate higher dimension parameters describing joint coupling and muscle synergies. The updated candidate plant set will then be used to conduct EMMILC experiments involving multi-finger grasping and combined wrist-finger movements, and explicitly compare their performance with conventional ILC method. This will naturally take longer and is a medium-to-long-term project.

5. To control complex movements, the system's dimension must be reduced in MIMO control design to ensure the time required by hardware to compute control signals is acceptable for home users. One possible solution has been investigated in [Freeman, 2014], which suggests finding a restricted input subspace $\mathcal{W} \in \mathbb{R}^{mN \times qN}, 0 <$

$q < m$. This maps a lower dimensional input $v_k \in \mathbb{R}^{qN}$ (to be controlled) to a higher dimensional input $u_k \in \mathbb{R}^{mN}$, i.e. $m = 24$, which yields $u_k = \mathcal{W}v_k$ and hence enables the control of a higher dimensional array system ($y_k = Gu_k$) using a lower dimensional control input v_k. The subset $\mathcal{W}$ can be identified using input and output data from previous experiments. Specifically, select those input and output data pairs $(u_{k,n}, y_{k,n})$ with $n = 1, 2, ..., a$ from previous experimental data with outputs $y_{k,n}$ that are sufficiently close to the reference signal. Then, the input subset can be directly identified as $\mathcal{W} = [u_{k,1}, u_{k,2}, ..., u_{k,a}]$ such that $qN = a$. The ultimate progress is to perform tasks of greater dimensionality without substantially increasing computational loads, thereby preventing hardware deceleration when handling extensive plant sets. This should be a short-term project.

6. The limited experimental data can also be used to produced multiple input subsets $(\mathcal{W}_1, \mathcal{W}_2, ..., \mathcal{W}_b)$ that include more physiological information such as skin impedance. These will then generate more candidate models $(G\mathcal{W}_1, G\mathcal{W}_2, ..., G\mathcal{W}_b)$ that enrich the candidate plant set and hence provide greater robustness. Progress in this area enable non-expert users to have satisfactory rehabilitation outcome without excessive controller calibration. This should be achievable in the medium term.

7. In Section 8.3, the true system is approximated as linear in control design by satisfying Assumptions 1 and 2. These assumptions restrict the range and velocity of functional movements, which limits the feasibility of the EMMILC approach in practice. To address this limitation, the whole approach will be extended to the nonlinear case. This starts from collecting input and output data, with the input $u_k = \mathcal{W}v_k$ to the nonlinear system and the response y_k. Secondly, linearise the system around an operating point v_a, which can be unpacked to $[v_a(0)^\top, v_a(1)^\top, ..., v_a(N-1)^\top]^\top$. This can be repeated in multiple tests to produce multiple linearised underlying plants, which can be combined with above points to enrich the candidate plant set. This enables a rigorous EMMILC framework to not only be used with FES-based stroke rehabilitation, but also with other sophisticated applications that lack robustness. This should also be an intermediate-duration project to perform multiple tests.

8. This thesis focused exclusively on upper-limb rehabilitation, but the underlying EMMILC framework also has potential applications in other related biomedical areas such as lower-limb rehabilitation (e.g., gait rehabilitation). Initial work will include identifying lower-limb muscle models, building candidate plant set for lower-limb by following the steps 2-4, and validating the EMMILC approach through preliminary experiments with both healthy subjects and stroke patients. These extensions would illustrate the expanded clinical feasibility of EMMILC beyond its initial framework in this research, offering additional benefit to other researchers and therapists. This should be achievable in the long term.

Appendix A

An extended version of Theorem 3.1 is given below, including a proof of the 2-norm bound on $||\Pi_{P_{\hat{p}^*}//C_{\hat{c}}}||$ given by (3.59).

Theorem A.1. *Let P_p, P_{p^*} be systems of form (3.3) and $C_{\hat{c}}$ be an ILC design for P_p such that condition (3.61) holds. Then this ILC design also stabilises the true plant P_{p^*} provided*

$$\delta(p, p^*) < \|\Pi_{P_{\hat{p}}//C_{\hat{c}}}\|^{-1}, \tag{A.1}$$

where the mapping

$$\begin{aligned}\|\Pi_{P_{\hat{p}}//C_{\hat{c}}}\| &= \left\| \begin{pmatrix} (I - C_{\hat{c}}P_{\hat{p}})^{-1} & -(I - C_{\hat{c}}P_{\hat{p}})^{-1}C_{\hat{c}} \\ P_{\hat{p}}(I - C_{\hat{c}}P_{\hat{p}})^{-1} & -P_{\hat{p}}(I - C_{\hat{c}}P_{\hat{p}})^{-1}C_{\hat{c}} \end{pmatrix} \right\| \\ &\leq \|(P_{\hat{p}}, I)\| \left(\frac{||(I, P_{\hat{p}})^\top|| \|Q_{\hat{c}}L_{\hat{c}}\|}{1 - \sigma} + 1 \right). \end{aligned} \tag{A.2}$$

The internal signals are bounded from their ideal values as

$$||\Pi_{P_{\hat{p}^*}//C_{\hat{c}}}|| \leq ||\Pi_{P_{\hat{p}}//C_{\hat{c}}}|| \frac{1 + \delta(p, p^*)}{1 - ||\Pi_{P_{\hat{p}}//C_{\hat{c}}}|| \delta(p, p^*)}. \tag{A.3}$$

Proof. This can be proved by extending the 1-norm and ∞-norm cases shown in [Bradley, 2010], to the 2-norm case. First set $w = (u_0, y_0 + y_{ref})^\top$ in (3.53) and apply (3.57), (3.58) to give

$$\begin{aligned}\left[\Pi_{P_{\hat{p}}//C_{\hat{c}}} w\right](k) = \begin{pmatrix} I \\ P_{\hat{p}} \end{pmatrix} \Big(\sum_{i=1}^{k} \Big\{ [Q_{\hat{c}}(I - L_{\hat{c}}P_{\hat{p}})^{i-1}(Q_{\hat{c}}L_{\hat{c}}y_{ref} \\ - Q_{\hat{c}}L_{\hat{c}}(P_{\hat{p}}, -I)w_0(k-i)) \Big\} + u_0(k) \Big)\end{aligned}$$

and it follows that an upper bound on $\|\Pi_{P_{\hat{p}}//C_{\hat{c}}}\|$ is

$$\sup_{\substack{w_0(k)\in\mathbb{R}^{mN\times nN}\\ \|w_0\|\neq 0}} \frac{\left(\sum_{k=0}^{\infty}\left\|\begin{pmatrix} I \\ P_{\hat{p}}\end{pmatrix}\sum_{i=1}^{k}\left[Q_{\hat{c}}(I-L_{\hat{c}}P_{\hat{p}})\right]^{i-1}Q_{\hat{c}}L_{\hat{c}}(-P_{\hat{p}},I)\times w_0(k-i)+u_0(k)\right\|^2\right)^{\frac{1}{2}}}{\left(\sum_{k=0}^{\infty}\|w_0(k)\|^2\right)^{\frac{1}{2}}}$$

Setting $u_0 = 0$ and $y_0 = 0$ separately and applying relationship

$$\frac{\|\Pi_{P_{\hat{p}}//C_{\hat{c}}}w_0\|}{\|w_0\|} = \frac{\left\|\Pi_{P_{\hat{p}}//C_{\hat{c}}}\begin{pmatrix}u_0\\0\end{pmatrix}\right\| + \left\|\Pi_{P_{\hat{p}}//C_{\hat{c}}}\begin{pmatrix}0\\y_0\end{pmatrix}\right\|}{\left\|\begin{pmatrix}u_0\\y_0\end{pmatrix}\right\|} \leq \left\|\Pi_{P_{\hat{p}}//C_{\hat{c}}}\Big|_{y_0=0}\right\| + \left\|\Pi_{P_{\hat{p}}//C_{\hat{c}}}\Big|_{u_0=0}\right\|$$

yields (A.2) after significant further manipulation. □

Appendix B

This study has shown the efficacy of the EMMILC method in addressing fatigue and array misalignment. To facilitate the application of EMMILC in practical FES training, this appendix outlines the development of a potential home-based FES hardware platform using an electrode array. The array platform includes a high-voltage analog multiplexer switching board alongside a Leap Motion depth camera for assessing joint angles.

B.1 Hardware Design of Electrode Array

A variety of array layouts have been employed in stroke rehabilitation. The Chapter 2 reviewed different arrays but mainly focused on the tracking accuracy. However, the revision highlighted that the choice of array layouts balanced muscle selectivity, spatial coverage, and hardware integration feasibility. Grid arrays with fewer electrode pads offer simplicity for identification and control, but often lack the muscle selectivity required by adaptive stimulation. For instance, the 4×4 arrays used in [Malešević et al., 2012; Crema et al., 2021] exhibited simple configuration. However, the restricted number of activation sites resulted in limited virtual electrode combinations, proving insufficient to correct spatial error. Similarly, Wang et al. [2021] employed a 4×5 array to minimise fatigue by performing sequential stimulation. Unfortunately, the limited coverage of the array presented difficulties in controlling complex movements involving various muscles. Larger layouts like a 4×6 array [Kutlu et al., 2015, 2016b] or 5×8 array [Freeman, 2014] improved muscle coverage and have been successfully applied with ILC. However, there was no control strategy or clinical evidence that confirmed their capability of coping with array misalignment. In [Keller et al., 2006b,a], a higher-dimensional array arranged in a 6×10 format was utilised to improve the selectivity of stimulation sites. However, it was mainly designed to mitigate fatigue or facilitate simple feedback control, rather than implement adaptive stimulation to correct spatial errors.

In contrast, the 8×8 electrode array used in the ShefStim system [Kenney et al., 2016] provided an optimal balance across these dimensions. Using finite element modeling, it was verified that this array configuration achieved greater spatial selectivity and reduced current spread by optimising electrode size, spacing, and surface resistivity. The experimental findings demonstrated that even untrained subjects could configure this array within 5 minutes without precisely placing it above the target muscles, as its effective integration with the control algorithm could compensate for any misalignment within 9 minutes. This was done by simply cycling through each pad element and choosing the one that produced the best movement. Therefore, an 8×8 array configuration is employed in this research to test EMMILC. Each electrode pad has dimensions of 12 mm $\times$ 12 mm, with a spacing of 1 mm between neighboring pads. This size design was chosen to reduce the unintended stimulation in adjacent muscle groups as justified in [Du et al., 2021]. The design will be printed on 0.1mm thick polycarbonate with two conductive layers: one side containing the pads, and the other side containing the connective tracks. These tracks link each electrode pad to a 0.5 mm-pitch terminal that operates as a flat cable. The array board was designed using EAGLE (version 9.6.2), and manufactured as a flexible printed circuit in order to adhere closely to the skin surface. The result is shown in Figure B.1. Having designed the electrode array, the next step is to investigate how to dynamically deliver the stimulation input to any specified electrode pad. This requires an an effective multiplexer device, which will be designed in the next section.

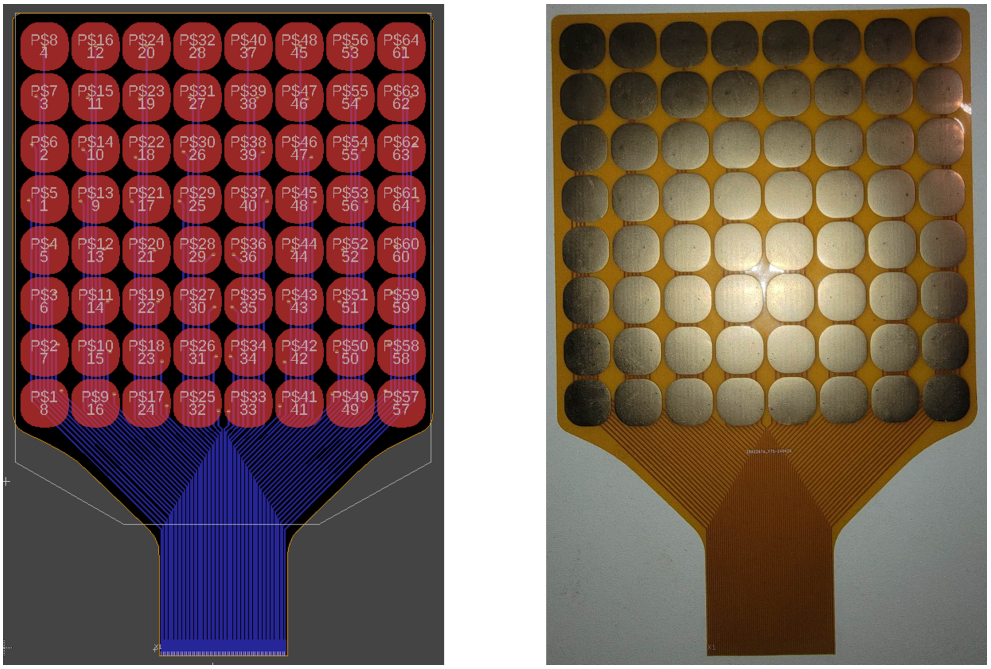

FIGURE B.1: (left) 8×8 surface electrode array and its manufactured item (right).

B.2 Hardware Design of Analog Multiplexer

The implementation of the designed array required a suitable high-voltage analog switch to dynamically activate or deactivate each electrode pad. Two channels of stimulation were chosen, to correspond with the use-case considered in Chapter 8. Each pad must be capable of being switched to either channel or to neither. To achieve this, an efficient multiplexer device was designed, integrating four 16-channel, high-voltage analog switches. The analog switch HV2607 microchip technology was chosen because

- The HV2607 can be operated with low-voltage supplies, and requires a positive voltage supply between $4.5V$ to $6.3V$, and a negative voltage supply between $-6.3V$ to $-4.5V$. These two supply voltages can be simply generated using an isolated dual-output DC-DC power converter (e.g. IAB0105D05 manufactured by XP Power), which converts a $+5V$ input to $\pm 5V$ outputs.
- Each analog switch in the HV2607 can be controlled separately through SPI communication integrated on the Raspberry Pi 4B board used in Chapter 6, which generates a sequence of $3.3V$ logic input signals that fall within the required voltage range of $2.7V$ to $5.5V$.
- The HV2607 analog switches are capable of switching analog input signals within a voltage range from $-110V$ to $110V$. This range encompasses the $100V$ voltage delivered by the commercial Odstock stimulator (Odstock Medical Limited, UK), as also used in Chapter 6.

Subsequently, all 64 switches were wired to a 0.5 mm-pitch, 64 pin connector that is compatible with flexible printed circuits or flat cables. The 64 pin terminal of the electrode array was inserted into this connector, where each pin was then directed to an electrode pad. The components of this multiplexer board are shown in Figure B.2. The circuit for the multiplexer is shown in Figure B.3. The Raspberry Pi 4B's SPI module was employed to dynamically control each analog switch, with the input ports of this multiplexer board being connected according to the specifications in Table B.1. Each HV2607 is controlled via a 16-bit binary code, where an analog switch is triggered when the corresponding bit is set to binary '1'. This FES device was tested and will next be used with human participants.

B.3 Hardware for Hand Tracking

To perform controller tests, it is essential for the hardware system to have real-time joint angle data measurements. In Chapter 6, the wrist angle was recorded using an instrumented wrist rig functioning as an electro-goniometer. However, this method is

TABLE B.1: The input ports of the integrated multiplexer board. SR: Shift Register.

Input port	Symbol	Operating Power	Connect to	Supplied Power
Positive Supply Voltage	V_{DD}	$+4.5 \sim +6.3$V	IAB0105D05 Positive Output	$+5V$
Negative Supply Voltage	V_{SS}	$-6.3 \sim -4.5$V	IAB0105D05 Negative Output	$-5V$
Logic Supply Voltage	V_{LL}	$+3 \sim +5.5$V	Raspi 4B 3.3V DC Power	$+3.3V$
Data In Logic Input	D_{IN}	$+2.7 \sim +5.5$V	Raspi 4B SPI module GPIO10(MOSI)	$+3.3V$
SPI Clock Logic Input	CLK	$+2.7 \sim +5.5$V	Raspi 4B SPI module GPIO11 (SCLK)	$+3.3V$
Latch Enable Logic Input (Low Active)	LE	$0 \sim +0.3$V $+2.7 \sim +5.5$V	Raspi 4B GPIO25	$\leq +0.3$V (Trigger SR)
Digital Ground	GND	N/A	Raspi 4B GPIO6 (GND)	N/A
Stimulation input Channel 1	$CH1$	$-110 \sim +110$V	Odstock stimulator Channel 1	$+100$V (Loaded)
Stimulation input Channel 2	$CH2$	$-110 \sim +110$V	Odstock stimulator Channel 2	$+100$V (Loaded)

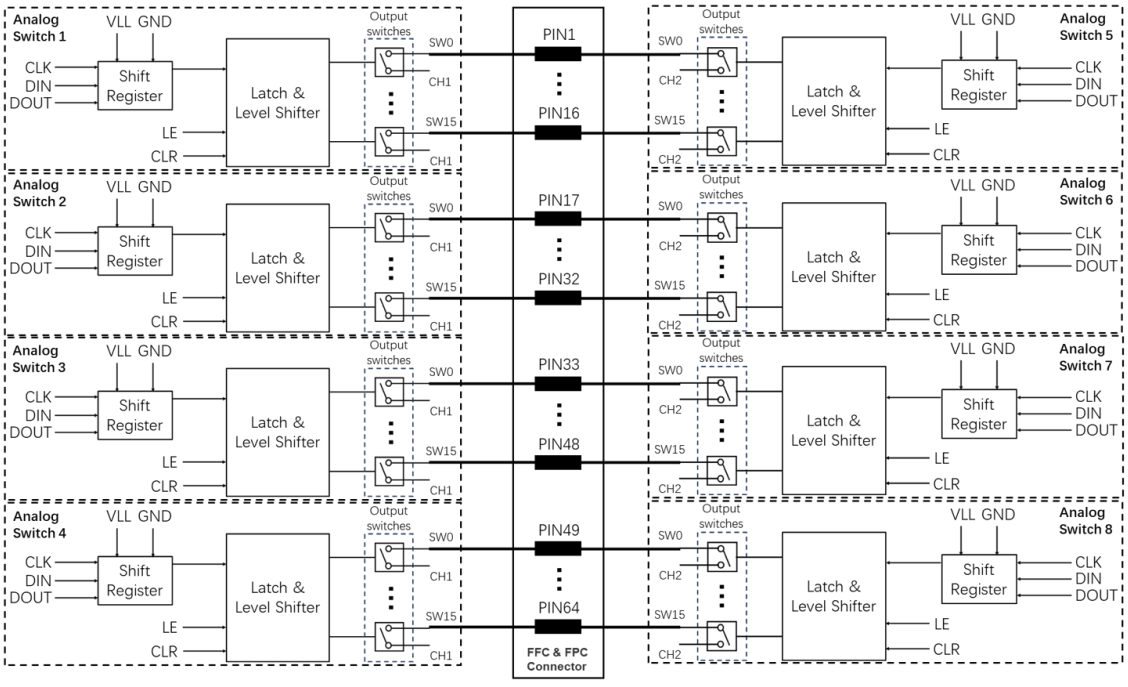

FIGURE B.2: Block diagram of the multiplexer board with 2 channels, 64 switches.

limited to measure only the planar wrist joint angle, which does not meet the requirement for the array system to record multiple hand joint angles. To accurately measure hand positions, a depth camera (Leap Motion Controller 2, Ultraleap) was selected to capture the depth information of each joint position in the environment (i.e., the distance between the joints detected and the camera itself). This can be used to produce

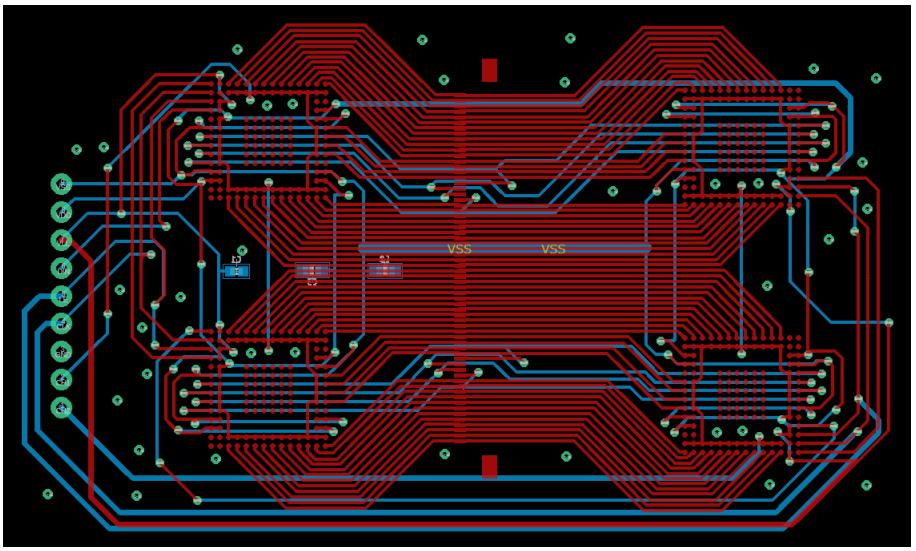

FIGURE B.3: The EAGLE circuit of the multiplexer integrating four HV2607 microchips.

the 3D coordinates for each joint, yielding a joint skeleton structure for the hand, as illustrated by Figure B.4 a). The variations of joint coordinates are then used to compute

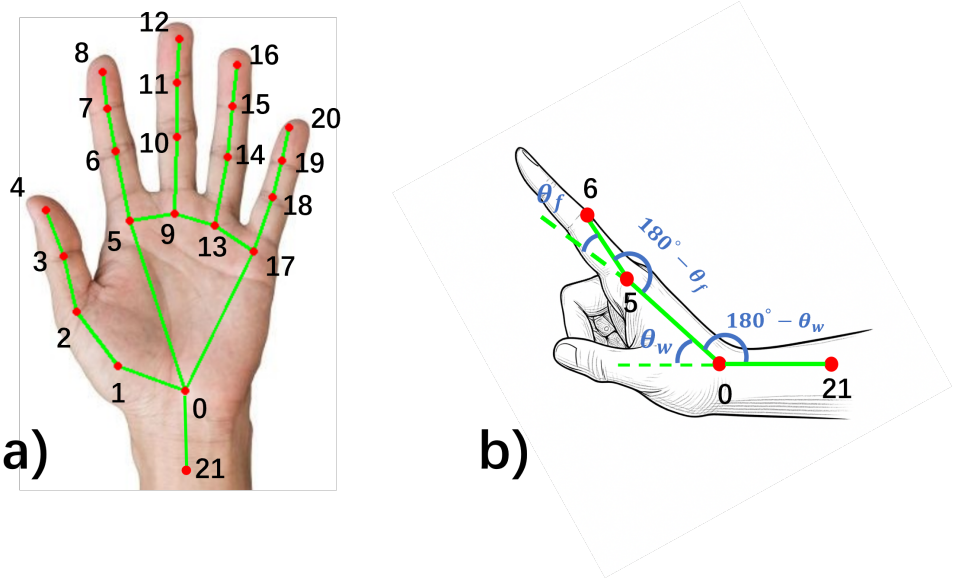

FIGURE B.4: Skeleton structure of a): joints indexed by $1, 2, ..., 20$. b): joint angles of the index finger and wrist.

the joint angles. The joint skeleton is defined in Figure B.4 a), where the joints indexed by 21, 0, 5, and 6 have Cartesian coordinates represented by J_{21}, J_0, J_5, and J_6, respectively. As illustrated by Figure B.4 b), the index finger joint angle θ_f, characterised by the coordinates of joints 0, 5, and 6, is computed in degrees as

$$\theta_f = 180 - \frac{180}{\pi} arccos\left(\frac{(J_6 - J_5)\cdot(J_0 - J_5)}{\|J_6 - J_5\|\|J_0 - J_5\|}\right). \tag{B.1}$$

Similarly, the wrist joint angle θ_w, characterised by the coordinates of joints 21, 0, and 5, is computed in degrees as

$$\theta_w = 180 - \frac{180}{\pi} arccos\left(\frac{(J_5 - J_0)\cdot(J_{21} - J_0)}{\|J_5 - J_0\|\|J_{21} - J_0\|}\right). \tag{B.2}$$

Using this method, any joint angle within this skeleton system can be computed in real-time, and subsequently relayed to the ILC update algorithm operating on the Raspberry Pi 4B board. This is achieved using a custom-made application written in C using Visual Studio, which utilises a WiFi server to interface with a client running on the Raspberry Pi's real-time Simulink programme. Figure B.5 illustrates the interaction among hardware components, which will experimentally tested in the next section.

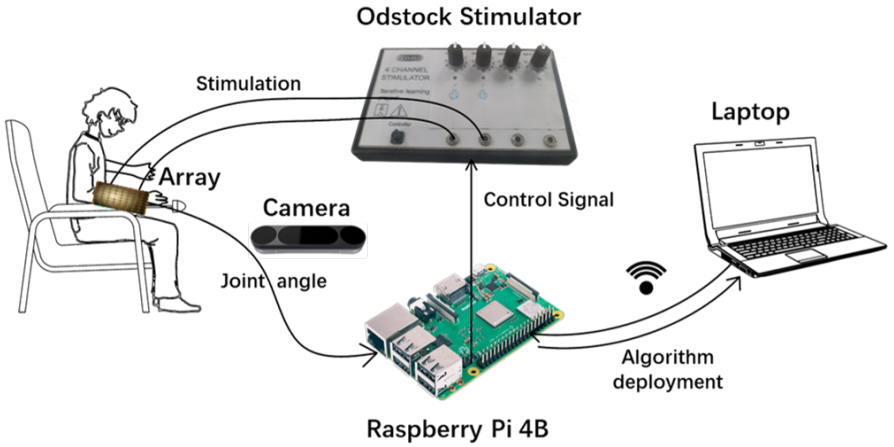

FIGURE B.5: The closed-loop interaction between hardware components.

B.4 Experimental Validation of Hardware Platform

After developing this hardware platform incorporating a novel array system, this section involves experimentally verifying its ability to adjust stimulation sites, which is crucial for the practical implementation of realignment ILC. The key point is to show that the activation of each stimulation site in the array corresponds to a joint movement. To achieve this, an experimental protocol is designed to sequentially activate each of 49 predefined 2×2 virtual electrodes (VE) in the array. This VE strategy is employed due to its capability of generating a stronger and uniform electric field, in order to activate deeper muscles or motor nerves [Kenney et al., 2016] and reduce discomfort [RaviChandran et al., 2023]. During the test, a stimulation pulsewidth of 300μs was applied to each VE sequentially through the port $CH1$ detailed in Table B.1, and the amplitude was gradually increased to a maximum tolerable limit. The wrist and finger joint angles defined in Figure 8.7 were measured as primary output data to describe the intended hand gesture when the stimulation amplitude reached its maximal

value. An unimpaired subject participated in the test once per day for three consecutive days, and was required to place the array device on the forearm each day by themselves, as shown in the Figure B.6 a). The ethics approval was granted by University of Southampton Ethics and Research Governance Online (ERGO), ID 102462.

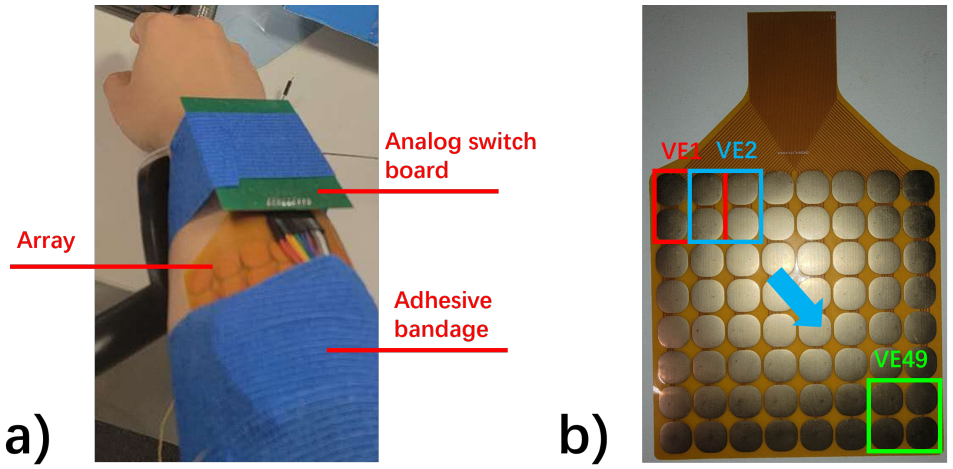

FIGURE B.6: Hardware system illustrated by a): array device on the forearm placed by the subject. b): sequential activation of each VE, indexed by $1, 2, ..., 49$.

By sequentially activating each of the 49 VEs, as illustrated in Figure B.6 b), the measured wrist angles θ_w, and finger angles θ_f for each day, were collected as the sets

$$\begin{aligned} \theta_w &= \{\theta_w(1), \theta_w(2), ..., \theta_w(49)\} \\ \theta_f &= \{\theta_f(1), \theta_f(2), ..., \theta_f(49)\}, \end{aligned} \tag{B.3}$$

where $\theta(a)$ denotes the joint angle measured when activating the a^{th} VE. To show the stimulation sites, the measured joint angles in each data set are illustrated in Figure B.7 for the test on day 1, Figure B.8 for day 2, and Figure B.9 for day 3.

By comparing the maps of the two joint angles recorded over three separate days, it can be visually summarised that the wrist movement is stronger when the VEs on the left side of the array are activated. Similarly, the index finger movement is stronger when the VEs in the middle of array are activated. This indicates that the array platform can effectively achieve spatial selectivity by associating each joint movement with the stimulation of a specific site.

Moreover, this test is also used to identify the target muscle stimulated by a VE which primarily actuates the main joint of the intended movement. This approximately satisfies the condition of the design approach outlined in Remark 1, thereby simplifying the control design, as detailed in Section 8.3. Among these Figures B.7, B.8, and B.9, a target muscle is identified by activating a VE that predominantly excites the main joint while

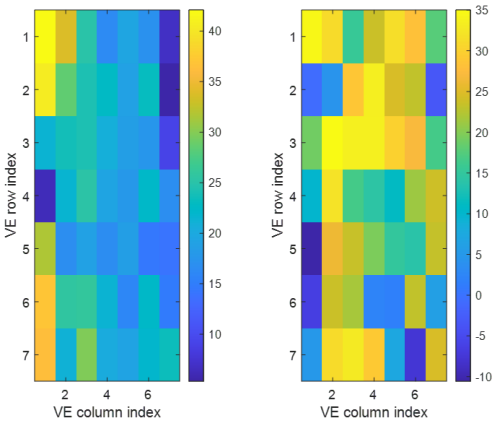

FIGURE B.7: The joint angles in the data sets θ_w [left] and θ_f [right] produced by activating each VE on day 1. Units in degrees.

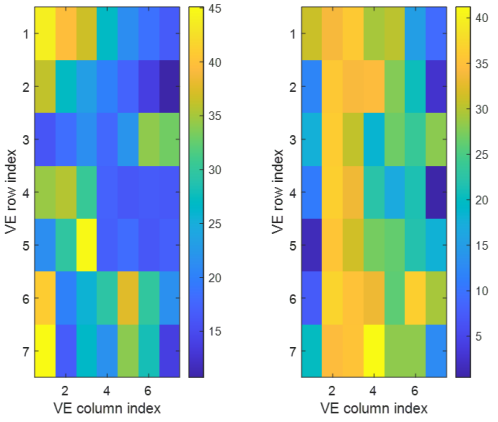

FIGURE B.8: The joint angles in the data sets θ_w [left] and θ_f [right] produced by activating each VE on day 2. Units in degrees.

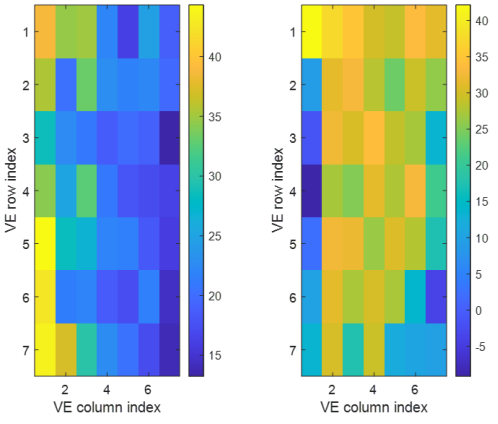

FIGURE B.9: The joint angles in the data sets θ_w [left] and θ_f [right] produced by activating each VE on day 3. Units in degrees.

minimally actuating another joint. This can be expressed by the optimisation problem

$$\begin{aligned} a_w &= \arg \max_{a \in \{1,2,\ldots,49\}} \left| \theta_w(a) - \theta_f(a) \right|, \\ a_f &= \arg \max_{a \in \{1,2,\ldots,49\}} \left| \theta_f(a) - \theta_w(a) \right|, \quad \theta_w(a) \in \theta_w, \quad \theta_f(a) \in \theta_f, \end{aligned} \tag{B.4}$$

where the solution, a_w^{th}, VE stimulates the target wrist muscle that primarily actuates the wrist joint. Similarly, the solution a_f^{th} VE stimulates the target finger muscle that primarily actuates the finger joint. By solving (B.4), the target stimulation sites of the wrist and finger muscles for each day are shown in Table B.2.

TABLE B.2: Target muscles identified for each day by solving (B.4).

	Target VE for wrist	**Target VE for finger**
Day 1	$a_w = 29$	$a_f = 14$
Day 2	$a_w = 28$	$a_f = 14$
Day 3	$a_w = 22$	$a_f = 21$

Having identified the target stimulation sites, they can be used by the controllers defined in early chapters. As described in Chapter 8, they might be misaligned when the array is repositioned. To address this, the realignment EMMILC approach can be applied with a set of candidate models (8.13), as implemented in Chapter 8. These results confirm the spatial selectivity achieved by this hardware platform, which can effectively choose stimulation sites in order to activate specified joint movements.

References

H. Ahn, K. L. Moore, and Y. Chen. Schur stability radius bounds for robust iterative learning controller design. In *Proceedings of the 2005 American Control Conference*, volume 1, pages 178–183, 2005.

N. Alibeji, N. Kirsch, B. E. Dicianno, and N. Sharma. A modified dynamic surface controller for delayed neuromuscular electrical stimulation. *IEEE/ASME Transactions on Mechatronics*, 22(4):1755–1764, 2017.

B. C. Allen, C. A. Cousin, C. A. Rouse, and W. E. Dixon. Robust cadence tracking for switched fes-cycling with an unknown time-varying input delay. *IEEE Transactions on Control Systems Technology*, 30(2):827–834, 2022a.

B. C. Allen, K. J. Stubbs, and W. E. Dixon. Data-based and opportunistic integral concurrent learning for adaptive trajectory tracking during switched fes-induced biceps curls. *IEEE Transactions on Neural Systems and Rehabilitation Engineering*, 30:2557–2566, 2022b.

N. Amann, D. H. Owens, and E. Rogers. Iterative learning control for discrete time systems with exponential rates of rate convergence. In *Proceeding of The Institution of Electrical Engineers on Control Theory and Applications*, pages 217–224, 1996.

N. Amann, D. H. Owens, and E. Rogers. Predictive optimal iterative learning control. *International Journal of Control*, 69(2):203–226, 1998.

K. D. Anderson. Targeting recovery: Priorities of the spinal cord-injured population. *Journal of neurotrauma*, 21(10):1371–83, 2004.

S. Arimoto, S. Kawamura, and F. Miyazaki. Bettering operation of dynamic systems by learning: A new control theory for servomechanism or mechatronics systems. In *The 23rd IEEE Conference on Decision and Control*, pages 1064–1069, 1984a.

S. Arimoto, S. Kawamura, and F. Miyazaki. Bettering operation of robots by learning. *Journal of Robotic systems*, 1(2):123–140, 1984b.

S. Arimoto, S. Kawamura, F. Miyazaki, and et.al. Learning control theory for dynamical systems. In *1985 24th IEEE Conference on Decision and Control*, pages 1375–1380, 1985.

M. Ayatinia, M. Forouzanfar, and A. Ramezani. An lmi approach to robust iterative learning control with initial state learning. *International Journal of Systems Science*, 53 (12):2664–2678, 2022.

B. R. Ballester, N. S. Ward, F. Brander, and et.al. Relationship between intensity and recovery in post-stroke rehabilitation: a retrospective analysis. *Journal of Neurology, Neurosurgery & Psychiatry*, 93(2):226–228, 2022.

E. C. Balta, D. M. Tilbury, and K. Barton. Iterative learning spatial height control for layerwise processes. *Automatica*, 167:111756, 2024.

K. Barton and A. Alleyne. Norm optimal ilc with time-varying weighting matrices. In *2009 American Control Conference*, pages 264–270, 2009.

G. Bijelić, A. Popović-Bijelić, N. Jorgovanović, and et.al. E actitrode: The new selective stimulation interface for functional movements in hemiplegics patients. *Serbian Journal of Electrical Engineering*, 1(3):21–28, 2004.

G. Bijelić, A. Popović-Bijelić, N. Jorgovanović, and et.al. Multi-field surface electrode for selective electrical stimulation. *Artificial Organs*, 29(6):448–452, 2005.

L. Blanken and T. Oomen. Multivariable iterative learning control design procedures: From decentralized to centralized, illustrated on an industrial printer. *IEEE Transactions on Control Systems Technology*, 28(4):1534–1541, 2019.

L. Blanken, S. Koekebakker, and T. Oomen. Data-driven feedforward tuning using non-causal rational basis functions: With application to an industrial flatbed printer. *Mechatronics*, 71:102424, 2020.

R. S. Bradley. *The Robust Stability of Iterative Learning Control*. PhD thesis, University of Southampton, 2010.

M. E. Brandstater and L. A. Shutter. Rehabilitation interventions during acute care of stroke patients. *Topics in Stroke Rehabilitation*, 9(2):48–56, 2002.

O. Brend, C. Freeman, and M. French. Multiple-model adaptive control of functional electrical stimulation. *IEEE Transactions on Control Systems Technology*, 23(5):1901–1913, 2015.

D. A. Bristow, M. Tharayil, and A. G. Alleyne. A survey of iterative learning control. *IEEE Control Systems Magazine*, 26(3):96–114, 2006.

D. Buchstaller and M. French. Robust stability for multiple model adaptive control: Part i—the framework. *in IEEE Transactions on Automatic Control*, 61(3):677–692, 2016a.

D. Buchstaller and M. French. Robust stability for multiple model adaptive control: Part ii—gain bounds. *in IEEE Transactions on Automatic Control*, 61(3):693–708, 2016b.

J. H. Burridge and M. Ladouceur. Clinical and therapeutic applications of neuromuscular stimulation: A review of current use and speculation into future developments. *Neuromodulation: Technology at the Neural Interface*, 4(4):147–154, 2001.

A. P. L. Bó, L. O. da Fonseca, and A. C. C. de Sousa. Fes-induced co-activation of antagonist muscles for upper limb control and disturbance rejection. *Medical Engineering & Physics*, 38(11):1176–1184, 2016.

Z. Cai, C. T. Freeman, P. L. Lewin, and et.al. Iterative learning control for a non-minimum phase plant based on a reference shift algorithm. *Control Engineering Practice*, 16(6):633–643, 2008.

S. K. Charles and N. Hogan. Dynamics of wrist rotations. *Journal of Biomechanics*, 44(4): 614–621, 2011.

S. K. Charles and N. Hogan. Stiffness, not inertial coupling, determines path curvature of wrist motions. *Journal of Neurophysiology*, 107(4):1230–1240, 2012.

X. Chu, X. Song, R. Li, Q. Li, Q. Li, X. Gu, and D. Ming. Multielectrode array-based percutaneous nerve stimulation strategy with ultrasound guidance for ulnar nerve injury. *IEEE Transactions on Neural Systems and Rehabilitation Engineering*, 31:1502–1510, 2023.

E. H. Copur, C. T. Freeman, B. Chu, and et.al. System identification for fes-based tremor suppression. *European Journal of Control*, 27:45–59, 2016.

A. Crema, N. Malešević, I. Furfaro, and et.al. A wearable multi-site system for nmes-based hand function restoration. *in IEEE Transactions on Neural Systems and Rehabilitation Engineering*, 26(2):428–440, 2018.

A. Crema, I. Furfaro, F. Raschellà, M. Rossini, J. Zajc, C. Wiesener, W. Baccinelli, D. Proserpio, A. Augsten, N. Immick, S. Becker, M. Weber, T. Schauer, K. Krakow, G. Gasperini, F. Molteni, M. F. Russold, M. Bulgheroni, and S. Micera. Reactive exercises with interactive objects: Interim analysis of a randomized trial on task-driven nmes grasp rehabilitation for subacute and early chronic stroke patients. *Sensors*, 21 (20), 2021.

B. H. Dobkin. Strategies for stroke rehabilitation. *The Lancet Neurology*, 3(9):528–536, 2004.

A. M. Dollar. *Classifying Human Hand Use and the Activities of Daily Living*, pages 201–216. Springer International Publishing, Cham, 2014.

T. Donkers, J. van de Wijdeven, and O. Bosgra. Robustness against model uncertainties of norm optimal iterative learning control. In *2008 American Control Conference*, pages 4561–4566, 2008.

M. K. Donovan-Hall, J. Burridge, B. Dibb, and et.al. The views of people with spinal cord injury about the use of functional electrical stimulation. *Artificial Organs*, 35(3): 204–211, 2011.

H. Dou, K. Tan, T. Lee, and et.al. Iterative learning feedback control of human limbs via functional electrical stimulation. *Control Engineering Practice*, 7(3):315–325, 1999.

A. Dromerick, M. Edwardson, D. Edwards, M. Giannetti, J. Barth, K. Brady, E. Chan, M. Tan, I. Tamboli, R. Chia, M. Orquiza, R. Padilla, A. Cheema, M. Mapstone, M. Fiandaca, H. Federoff, and E. Newport. Critical periods after stroke study: translating animal stroke recovery experiments into a clinical trial. *Frontiers in Human Neuroscience*, 9, 2015.

J. Du, A. Morales, J. Paknahad, P. Kosta, J.-M. C. Bouteiller, E. Fernández, and G. Lazzi. Electrode spacing and current distribution in electrical stimulation of peripheral nerve: A computational modeling study using realistic nerve models. In *EMBC*, pages 4416–4419, 2021.

H. Elci, R. Longman, M. Phan, J.-N. Juang, and R. Ugoletti. Simple learning control made practical by zero-phase filtering: applications to robotics. *IEEE Transactions on Circuits and Systems I: Fundamental Theory and Applications*, 49(6):753–767, 2002.

T. Excell, C. T. Freeman, K. Meadmore, and et.al. Optimisation of hand posture stimulation using an electrode array and iterative learning control. *Journal of Automatic Control*, 21(1):1–4, 2013.

S. Fekri, M. Athans, and A. Pascoal. Rmmac: a novel robust adaptive control scheme. part i. architecture. In *2004 43rd IEEE Conference on Decision and Control (CDC) (IEEE Cat. No.04CH37601)*, volume 2, pages 1134–1139, 2004a.

S. Fekri, M. Athans, and A. Pascoal. Rmmac: a novel robust adaptive control scheme. part ii. performance evaluation. In *2004 43rd IEEE Conference on Decision and Control (CDC) (IEEE Cat. No.04CH37601)*, volume 2, pages 1140–1145, 2004b.

F. Felici and T. Oomen. Enhancing current density profile control in tokamak experiments using iterative learning control. In *2015 54th IEEE Conference on Decision and Control (CDC)*, pages 5370–5377, 2015.

C. Freeman, P. Sampson, J. Burridge, and A.-M. Hughes. Repetitive control of functional electrical stimulation for induced tremor suppression. *Mechatronics*, 32:79–87, 2015.

C. Freeman, K. Yang, J. Tudor, and M. Kutlu. Feedback control of electrical stimulation electrode arrays. *Medical Engineering Physics*, 38(11):1185–1194, 2016.

C. T. Freeman. Electrode array-based electrical stimulation using ilc with restricted input subspace. *Control Engineering Practice*, 23:32–43, 2014.

C. T. Freeman. *Control System Design for Electrical Stimulation in Upper Limb Rehabilitation*. Springer International Publishing. Springer International Publishing, 2016.

C. T. Freeman and M. French. Estimation based multiple model iterative learning control. In *2015 54th IEEE Conference on Decision and Control (CDC)*, pages 6070–6075, 2015.

C. T. Freeman, P. L. Lewin, and E. Rogers. Experimental evaluation of iterative learning control algorithms for non-minimum phase plants. *International Journal of Control*, 78 (11):826–846, 2005.

C. T. Freeman, A.-M. Hughes, J. H. Burridge, P. H. Chappell, P. L. Lewin, and E. Rogers. A model of the upper extremity using fes for stroke rehabilitation. *Journal of Biomechanical Engineering*, 131(3):031011, 2009a.

C. T. Freeman, A. M. Hughes, J. H. Burridge, and et.al. Iterative learning control of fes applied to the upper extremity for rehabilitation. *Control Engineering Practice*, 17(3): 368–381, 2009b.

C. T. Freeman, P. L. Lewin, E. Rogers, and et.al. Discrete fourier transform based iterative learning control design for linear plants with experimental verification. *Journal of Dynamic Systems, Measurement and Control*, 131(3):031006–1–031006–10, 2009c.

C. T. Freeman, E. Rogers, A.-M. Hughes, J. H. Burridge, and K. L. Meadmore. Iterative learning control in health care: Electrical stimulation and robotic-assisted upper-limb stroke rehabilitation. *IEEE Control Systems Magazine*, 32(1):18–43, 2012.

T. L. C. J. M. N. C. L. H. J. S. C. T. S. French, B and C. Watkins. Repetitive task training for improving functional ability after stroke. *Cochrane Database of Systematic Reviews*, (11), 2016.

B. Freriks, H. J. Hermens, C. Disselhorst-Klug, and et.al. *SENIAM 8: European Recommendations for Surface ElectroMyoGraphy*, chapter 2: The Recommendations for Sensors and Sensor Placement Procedures for Surface ElectroMyoGraphy. Roessingh Research and Development, 1999.

K. Furuta and M. Yamakita. The design of a learning control system for multivariable systems. In *Proceedings of the IEEE International Symposium on Intelligent Control*, pages 371–376, 1987.

V. Gauthier, A. Bolopion, and M. Gauthier. Analytical formulation of the electric field induced by electrode arrays: Towards automated dielectrophoretic cell sorting. *Micromachines*, 8(8):253, 2017.

T. T. Georgiou and M. C. Smith. Optimal robustness in the gap metric. In *Proceedings of the 28th IEEE Conference on Decision and Control*, volume 3, pages 2331–2336, 1989.

S. B. Godfrey, P. S. Lum, E. Chan, and M. L. Harris-Love. Cortical effects of repetitive finger flexion- vs. extension-resisted tracking movements: a tms study. *Journal of Neurophysiology*, 109(4):1009–1016, 2013.

R. Gopura, K. Kiguchi, and E. Horikawa. A study on human upper-limb muscles activities during daily upper-limb motions. *International Journal of Bioelectromagnetism*, 12(2):54–61, 2010.

S. Gunnarsson and M. Norrlöf. On the design of ilc algorithms using optimization. *Automatica*, 37(12):2011–2016, 2001.

Y. Handa, N. Hoshimiya, Y. Iguchi, and et.al. Development of percutaneous intramuscular electrode for multichannel fes system. *in IEEE Transactions on Biomedical Engineering*, 36(7):705–710, 1989.

T. J. Harte, J. Hätönen, and D. H. Owens. Discrete-time inverse model-based iterative learning control: stability, monotonicity and robustness. *International Journal of Control*, 78(8):577–586, 2005.

K. S. Hayward, S. F. Kramer, V. Thijs, and et.al. A systematic review protocol of timing, efficacy and cost effectiveness of upper limb therapy for motor recovery post-stroke. *Systematic reviews*, 8(1):187, 2019.

L. Hladowski, K. Galkowski, Z. Cai, and et.al. Experimentally supported 2d systems based iterative learning control law design for error convergence and performance. *Control Engineering Practice*, 18(4):339–348, 2010.

A. Hochstenbach-Waelen and H. A. Seelen. Embracing change: practical and theoretical considerations for successful implementation of technology assisting upper limb training in stroke. *Journal of neuroengineering and rehabilitation*, 9:1–12, 2012.

E. F. Hodkin, Y. Lei, J. Humby, I. S. Glover, S. Choudhury, H. Kumar, M. A. Perez, H. Rodgers, and A. Jackson. Automated FES for upper limb rehabilitation following stroke and spinal cord injury. *IEEE Transactions on Neural Systems and Rehabilitation Engineering*, 26(5):1067–1074, 2018.

O. A. Howlett, N. A. Lannin, L. Ada, and et.al. Functional electrical stimulation improves activity after stroke: A systematic review with meta-analysis. *Archives of Physical Medicine and Rehabilitation*, 96(5):934–943, 2015.

D. Huang, J.-X. Xu, V. Venkataramanan, and T. C. T. Huynh. High-performance tracking of piezoelectric positioning stage using current-cycle iterative learning control with gain scheduling. *IEEE Transactions on Industrial Electronics*, 61(2):1085–1098, 2014.

A. Hughes, C. Freeman, J. Burridge, P. Chappell, P. Lewin, and E. Rogers. Feasibility of iterative learning control mediated by functional electrical stimulation for reaching after stroke. *Neurorehabilitation and neural repair*, 23(6):559–568, 2009.

A. Hughes, J. Burridge, S. Demain, and et.al. Translation of evidence-based assistive technologies into stroke rehabilitation: Users' perceptions of the barriers and opportunities. *BMC health services research*, 14:124, 2014.

B. Huo, Y. Liu, Y. Qin, and et.al. Disturbance observer based iterative learning control for upper limb rehabilitation. In *IECON 2020 The 46th Annual Conference of the IEEE Industrial Electronics Society*, pages 2774–2779, 2020.

J. Hätönen, C. Freeman, D. Owens, and et.al. A gradient-based repetitive control algorithm combining ilc and pole placement. *European Journal of Control*, 12(3):278–292, 2006.

T. Ikezoe, Y. Asakawa, Y. Fukumoto, R. Tsukagoshi, and N. Ichihashi. Associations of muscle stiffness and thickness with muscle strength and muscle power in elderly women. *Geriatrics & Gerontology International*, 12(1):86–92, 2012.

E. Imatz-Ojanguren, E. Irigoyen, D. Valencia-Blanco, and et.al. Neuro-fuzzy models for hand movements induced by functional electrical stimulation in able-bodied and hemiplegic subjects. *Medical Engineering & Physics*, 38(11):1214–1222, 2016.

S. V. Johansen, M. R. Jensen, B. Chu, J. D. Bendtsen, J. Mogensen, and E. Rogers. Broiler fcr optimization using norm optimal terminal iterative learning control. *IEEE Transactions on Control Systems Technology*, 29(2):580–592, 2019.

M. W. Keith, P. H. Peckham, G. B. Thrope, and et.al. Implantable functional neuromuscular stimulation in the tetraplegic hand. *The Journal of Hand Surgery*, 14(3):524–530, 1989.

T. Keller and A. Kuhn. Electrodes for transcutaneous (surface) electrical stimulation. *Journal of Automatic Control*, 18(2):35–45, 2008.

T. Keller, B. Hackl, M. Lawrence, and et.al. Identification and control of hand grasp using multi-channel tes. In *in Proceedings Annual Conference of the International FES Society (IFESS), (Zao, Japan)*, page 29–31, 2006a.

T. Keller, M. Lawrence, A. Kuhn, and M. Morari. New multi-channel transcutaneous electrical stimulation technology for rehabilitation. In *2006 International Conference of the IEEE Engineering in Medicine and Biology Society*, pages 194–197, 2006b.

L. P. Kenney, B. W. Heller, A. T. Barker, M. L. Reeves, J. Healey, T. R. Good, G. Cooper, N. Sha, S. Prenton, A. Liu, and D. Howard. A review of the design and clinical evaluation of the shefstim array-based functional electrical stimulation system. *Medical Engineering Physics*, 38(11):1159–1165, 2016.

M. Ketelhut, S. Stemmler, J. Gesenhues, M. Hein, and D. Abel. Iterative learning control of ventricular assist devices with variable cycle durations. *Control Engineering Practice*, 83:33–44, 2019.

C. Klauer, E. Ambrosini, S. Ferrante, and et.al. Co-activation and eemg-feedback for restoring hand-functions. In *2019 18th European Control Conference (ECC)*, pages 191–196, 2019.

M. G. H. Kristensen, H. Busk, and T. Wienecke. Neuromuscular electrical stimulation improves activities of daily living post stroke: A systematic review and meta-analysis. *Journal of Electromyography and Kinesiology*, 4(1):100167, 2022.

M. Kutlu, C. T. Freeman, E. Hallewell, A.-M. Hughes, and D. S. Laila. Fes-based upper-limb stroke rehabilitation with advanced sensing and control. In *2015 IEEE International Conference on Rehabilitation Robotics (ICORR)*, pages 253–258, 2015.

M. Kutlu, C. Freeman, E. Hallewell, A.-M. Hughes, and D. Laila. Upper-limb stroke rehabilitation using electrode-array based functional electrical stimulation with sensing and control innovations. *Medical Engineering Physics*, 38(4):366–379, 2016a.

M. Kutlu, C. T. Freeman, E. Hallewell, and et.al. Upper-limb stroke rehabilitation using electrode-array based functional electrical stimulation with sensing and control innovations. *Medical Engineering & Physics*, 38(4):366–379, 2016b.

G. Kwakkel. Impact of intensity of practice after stroke: no.s for consideration. *Disability and Rehabilitation*, 28(13-14):823–830, 2006.

D. G. Lainiotis. Partitioning: A unifying framework for adaptive systems, i: Estimation. In *Proceedings of the IEEE*, volume 64, pages 1126–1143, 1976a.

D. G. Lainiotis. Partitioning: A unifying framework for adaptive systems, ii: Control. In *Proceedings of the IEEE*, volume 64, pages 1182–1198, 1976b.

P. Langhorne, F. Coupar, and A. Pollock. Motor recovery after stroke: a systematic review. *The Lancet Neurology*, 8(8):741–754, 2009.

F. Le, I. Markovsky, C. T. Freeman, and et.al. Identification of electrically stimulated muscle models of stroke patients. *Control Engineering Practice*, 18(4):396–407, 2010.

J. H. Lee, K. S. Lee, and W. C. Kim. Model-based iterative learning control with a quadratic criterion for time-varying linear systems. *Automatica*, 36(5):641–657, 2000.

M. K. leung Chan, R. K. yu Tong, and K. Y. kwan Chung. Bilateral upper limb training with functional electric stimulation in patients with chronic stroke. *Neurorehabilitation and Neural Repair*, 23(4):357–365, 2009.

X. Li and W. Zhang. Multiple model iterative learning control. *Neurocomputing*, 73(13): 2439–2445, 2010.

X. Li, K. Wang, and D. Liu. An improved result of multiple model iterative learning control. *in IEEE/CAA Journal of Automatica Sinica*, 1(3):315–322, 2014.

W. T. Liberson, H. J. Holmquest, D. Scot, and et.al. Functional electrotherapy: stimulation of the peroneal nerve synchronized with the swing phase of the gait of hemiplegic patients. *Archives of Physical Medicine and Rehabilitation*, 42:101–105, 1961.

T. Lin, D. H. Owens, and J. Hätönen. Newton method based iterative learning control for discrete non-linear systems. *International Journal of Control*, pages 1263–1276, 2006.

Y. Liu, Y. Qin, B. Huo, and Z. Wu. Functional electrical stimulation based bicep force control via active disturbance rejection control. In *2020 5th International Conference on Advanced Robotics and Mechatronics (ICARM)*, pages 306–311, 2020.

L. Livshitz, J. Mizrahi, and P. Einziger. Interaction of array of finite electrodes with layered biological tissue: effect of electrode size and configuration. *IEEE Transactions on Neural Systems and Rehabilitation Engineering*, 9(4):355–361, 2001.

London: Intercollegiate Stroke Working Party. National clinical guideline for stroke for the uk and ireland. Available at www.strokeguideline.org, 2023.

R. Longman, Y. Peng, T. Kwon, and et.al. Adaptive inverse iterative learning control. *Journal of the Chinese Society of Mechanical Engineers, Transactions of the Chinese Institute of Engineers - Series C*, 32(6):493–506, 2011.

P. S. Lum, C. G. Burgar, P. C. Shor, and et.al. Robot-assisted movement training compared with conventional therapy techniques for the rehabilitation of upper-limb motor function after stroke. *Archives of Physical Medicine and Rehabilitation*, 83(7):952–959, 2002.

L. Ma, X. Liu, X. Kong, and K. Y. Lee. Iterative learning model predictive control based on iterative data-driven modeling. *IEEE Transactions on Neural Networks and Learning Systems*, 32(8):3377–3390, 2021.

P. Maciejasz, J. Eschweiler, K. Gerlach-Hahn, A. Jansen-Troy, and S. Leonhardt. A survey on robotic devices for upper limb rehabilitation. *Journal of neuroengineering and rehabilitation*, 11:1–29, 2014.

N. M. Malešević, L. Z. P. Maneski, V. Ilić, N. Jorgovanović, G. Bijelić, T. Keller, and D. B. Popović. A multi-pad electrode based functional electrical stimulation system for restoration of grasp. *Journal of neuroengineering and rehabilitation*, 9:1–12, 2012.

N. Malešević, L. Maneski, G. Bijelic, and et.al. Muscle twitch responses for shaping the multi-pad electrode for functional electrical stimulation. *Journal of Automatic Control*, 20(1):53–58, 2010a.

N. Malešević, L. Popović, G. Bijelić, and et.al. Classification of muscle twitch response using ann: Application in multi-pad electrode optimization. In *10th Symposium on Neural Network Applications in Electrical Engineering*, pages 11–13, 2010b.

S. Mandra, K. Galkowski, E. Rogers, and et.al. Performance-enhanced robust iterative learning control with experimental application to pmsm position tracking. *IEEE Transactions on Control Systems Technology*, 27(4):1813–1819, 2019.

K. A. Mann, F. W. Werner, and A. K. Palmer. Frequency spectrum analysis of wrist motion for activities of daily living. *Journal of orthopaedic research : official publication of the Orthopaedic Research Society*, 7(2):304–306, 1989.

MathWorks. *Analog Input Using SPI*. MathWorks, 2023. URL https://www.mathworks.com/help/releases/R2023a/supportpkg/raspberrypiio/ref/analog-input-using-spi.html. Accessed: 2025-07-16.

J. Mehrholz, T. Platz, J. Kugler, and et.al. Electromechanical and robot-assisted arm training for improving arm function and activities of daily living after stroke. *Stroke*, 40(5):e392–e393, 2009.

D. Meng. Convergence conditions for solving robust iterative learning control problems under nonrepetitive model uncertainties. *IEEE Transactions on Neural Networks and Learning Systems*, 30(6):1908–1919, 2019.

D. Meng and K. L. Moore. Robust iterative learning control for nonrepetitive uncertain systems. *IEEE Transactions on Automatic Control*, 62(2):907–913, 2017.

S. Meyer, A. H. Karttunen, V. Thijs, and et.al. How Do Somatosensory Deficits in the Arm and Hand Relate to Upper Limb Impairment, Activity, and Participation Problems After Stroke? A Systematic Review. *Physical Therapy*, 94(9):1220–1231, 2014.

S. Micera, T. Keller, M. Lawrence, and et.al. Wearable neural prostheses. *in IEEE Engineering in Medicine and Biology Magazine*, 29(3):64–69, 2010.

A. S. Morse. Supervisory control of families of linear set-point controllers - part i. exact matching. *in IEEE Transactions on Automatic Control*, 41(10):1413–1431, 1996.

A. S. Morse. Supervisory control of families of linear set-point controllers. 2. robustness. *in IEEE Transactions on Automatic Control*, 42(11):1500–1515, 1997.

P. Müller, C. Balligand, T. Seel, and et.al. Iterative learning control and system identification of the antagonistic knee muscle complex during gait using functional electrical stimulation. *IFAC-PapersOnLine*, 50(1):8786–8791, 2017.

H. Nahrstaedt, T. Schauer, R. Shalaby, and et.al. Automatic control of a drop-foot stimulator based on angle measurement using bioimpedance. *Artificial Organs*, 32(8): 649–654, 2008a.

H. Nahrstaedt, T. Schauer, R. Shalaby, S. Hesse, and J. Raisch. Automatic control of a drop-foot stimulator based on angle measurement using bioimpedance. *Artificial organs*, 32(8):649–654, 2008b.

D. S. Nichols-Larsen, P. Clark, A. Zeringue, A. Greenspan, and S. Blanton. Factors influencing stroke survivors' quality of life during subacute recovery. *Stroke*, 36(7): 1480–1484, 2005.

M. E. J. Obien, K. Deligkaris, T. Bullmann, D. J. Bakkum, and U. Frey. Revealing neuronal function through microelectrode array recordings. *Frontiers in Neuroscience*, 8: 423, 2015.

T. R. Oliveira, L. R. Costa, J. M. Y. Catunda, and et.al. Time-scaling based sliding mode control for neuromuscular electrical stimulation under uncertain relative degrees. *Medical Engineering and Physics*, 44:53–62, 2017.

D. H. Owens. *Iterative Learning Control: An Optimization Paradigm (Advances in Industrial Control)*. Springer, New York, 2016.

D. H. Owens and B. Chu. Combined inverse and gradient iterative learning control: performance, monotonicity, robustness and non-minimum-phase zeros. *International Journal of Robust and Nonlinear Control*, 24(3):406–431, 2014.

D. H. Owens, J. Hätönen, and S. Daley. Robust monotone gradient-based discrete-time iterative learning control. *International Journal of Robust and Nonlinear Control*, 19(6): 634–661, 2009.

D. H. Owens, C. T. Freeman, and B. Chu. An inverse-model approach to multivariable norm optimal iterative learning control with auxiliary optimisation. *International Journal of Control*, 87(8):1646–1671, 2014.

S. O'Dwyer, D. O'Keeffe, S. Coote, and et.al. An electrode configuration technique using an electrode matrix arrangement for fes-based upper arm rehabilitation systems. *Medical Engineering & Physics*, 28(2):166–176, 2006.

R. Padmanabhan, M. Bhushan, K. K. Hebbar, and et.al. Second-level adaptation and optimization for multiple model adaptive iterative learning control. In *2021 Seventh Indian Control Conference (ICC)*, pages 289–294, 2021.

K. Park, P. H. Chang, and S. H. Kang. In vivo estimation of human forearm and wrist dynamic properties. *in IEEE Transactions on Neural Systems and Rehabilitation Engineering*, 25(5):436–446, 2017.

K.-H. Park, Z. Bien, and D.-H. Hwang. Design of an iterative learning controller for a class of linear dynamic systems with time delay. In *IEE Proceedings-Control Theory and Applications*, volume 145, pages 507–512, 1998.

W. Paszke, R. Merry, and R. van de Molengraft. Iterative learning control by two-dimensional system theory applied to a motion system. In *2007 American control conference*, pages 5484–5489, 2007.

W. Paszke, E. Rogers, and K. Gałkowski. Experimentally verified generalized kyp lemma based iterative learning control design. *Control Engineering Practice*, 53:57–67, 2016.

A. W. Peaden and S. K. Charles. Dynamics of wrist and forearm rotations. *Journal of Biomechanics*, 47(11):2779–2785, 2014.

P. H. Peckham and G. H. Creasey. Neural prostheses: clinical applications of functional electrical stimulation in spinal cord injury. *Paraplegia*, 30(2):96–101, 1992.

T. Pelton, P. van Vliet, and K. Hollands. Interventions for improving coordination of reach to grasp following stroke: a systematic review. *International Journal of Evidence-Based Healthcare*, 10(2):89–102, 2012.

D. Popović and M. Popović. Automatic determination of the optimal shape of a surface electrode: Selective stimulation. *Journal of Neuroscience Methods*, 178(1):174–181, 2009.

L. Popović, M. Kostić, G. Bijelić, and et.al. Multi-pad electrode for effective grasping: Design. *in IEEE Transactions on Neural Systems and Rehabilitation Engineering*, 21(4): 648–654, 2013.

S. Prenton, L. P. Kenney, C. Stapleton, and et.al. Feasibility study of a take-home array-based functional electrical stimulation system with automated setup for current functional electrical stimulation users with foot-drop. *Archives of Physical Medicine and Rehabilitation*, 95(10):1870–1877, 2014.

J. D. Ratcliffe, T. J. Harte, J. Hätönen, and et.al. Practical implementation of a model inverse optimal iterative learning controller. *IFAC Proceedings Volumes*, 37(12):687–692, 2004.

J. D. Ratcliffe, J. J. Hatonen, P. L. Lewin, E. Rogers, T. J. Harte, and D. H. Owens. P-type iterative learning control for systems that contain resonance. *International Journal of Adaptive Control and Signal Processing*, 19(10):769–796, 2005.

J. D. Ratcliffe, P. L. Lewin, E. Rogers, and et.al. Norm-optimal iterative learning control applied to gantry robots for automation applications. *in IEEE Transactions on Robotics*, 22(6):1303–1307, 2006a.

J. D. Ratcliffe, P. L. Lewin, E. Rogers, J. J. Hatonen, and D. H. Owens. Norm-optimal iterative learning control applied to gantry robots for automation applications. *IEEE Transactions on Robotics*, 22(6):1303–1307, 2006b.

N. RaviChandran, K. Aw, and A. McDaid. Automatic calibration of electrode arrays for dexterous neuroprostheses: a review. *Biomedical Physics & Engineering Express*, 9(5): 052001, 2023.

R. S. Razavian, B. Ghannadi, N. Mehrabi, and et.al. Feedback control of functional electrical stimulation for 2-d arm reaching movements. *IEEE Transactions on Neural Systems and Rehabilitation Engineering*, 26(10):2033–2043, 2018.

D. J. Reinkensmeyer, P. Bonato, M. L. Boninger, L. Chan, R. E. Cowan, B. J. Fregly, and M. M. Rodgers. Major trends in mobility technology research and development: overview of the results of the nsf-wtec european study. *Journal of neuroengineering and rehabilitation*, 9:1–4, 2012.

F. Resquín, A. Cuesta Gómez, J. Gonzalez-Vargas, F. Brunetti, D. Torricelli, F. Molina Rueda, R. Cano de la Cuerda, J. C. Miangolarra, and J. L. Pons. Hybrid robotic systems for upper limb rehabilitation after stroke: A review. *Medical Engineering & Physics*, 38(11):1279–1288, 2016a.

F. Resquín, J. Gonzalez-Vargas, J. Ibáñez, and et.al. Feedback error learning controller for functional electrical stimulation assistance in a hybrid robotic system for reaching rehabilitation. *European journal of translational myology*, 26(3):255–261, 2016b.

A. Rezaeizadeh and R. S. Smith. Iterative learning control for the radio frequency subsystems of a free-electron laser. *IEEE Transactions on Control Systems Technology*, 26(5): 1567–1577, 2017.

E. Rogers, K. Galkowski, and D. Owens. *Control Systems Theory and Applications for Linear Repetitive Processes*. Lecture Notes in Control and Information Sciences. Springer Berlin Heidelberg, 2007. ISBN 9783540426639. URL https://books.google.co.uk/books?id=8YsUN2yWY2IC.

E. Rogers, D. H. Owens, H. Werner, C. T. Freeman, P. L. Lewin, S. Kichhoff, C. Schmidt, and G. Lichtenberg. Norm optimal iterative learning control with application to problems in accelerator based free electron lasers and rehabilitation robotics. *European Journal of Control*, 16(5):497–524, 2010.

E. Rogers, B. Chu, C. Freeman, and P. Lewin. *Iterative Learning Control Algorithms and Experimental Benchmarking*. Wiley, New York, 2023.

I. Rotariu, M. Steinbuch, and R. Ellenbroek. Adaptive iterative learning control for high precision motion systems. *IEEE Transactions on Control Systems Technology*, 16 (5):1075–1082, 2008.

C. A. Rouse, A. Parikh, V. Duenas, and et.al. Compensating for changing muscle geometry of the biceps brachii during neuromuscular electrical stimulation: A switched systems approach. In *2016 IEEE 55th Conference on Decision and Control (CDC)*, pages 1328–1333, 2016.

S. Saab. A discrete-time learning control algorithm for a class of linear time-invariant systems. *IEEE Transactions on Automatic Control*, 40(6):1138–1142, 1995.

P. Sampson, C. Freeman, S. Coote, S. Demain, P. Feys, K. Meadmore, and A.-M. Hughes. Using functional electrical stimulation mediated by iterative learning control and robotics to improve arm movement for people with multiple sclerosis. *IEEE transactions on neural systems and rehabilitation engineering*, 24(2):235–248, 2016.

G. Saposnik and M. Levin. Virtual reality in stroke rehabilitation. *Stroke*, 42(5):1380–1386, 2011.

G. N. Saridis and T. K. Dao. A learning approach to the parameter-adaptive self-organizing control problem. *Automatica*, 8(5):589–597, 1972.

S. Sa–e, C. T. Freeman, and K. Yang. Iterative learning control of functional electrical stimulation in the presence of voluntary user effort. *Control Engineering Practice*, 96: 104303, 2020.

T. Seel, C. Werner, J. Raisch, and T. Schauer. Iterative learning control of a drop foot neuroprosthesis — generating physiological foot motion in paretic gait by automatic feedback control. *Control Engineering Practice*, 48:87–97, 2016.

N. Sharma, C. M. Gregory, and W. E. Dixon. Predictor-based compensation for electromechanical delay during neuromuscular electrical stimulation. *IEEE Transactions on Neural Systems and Rehabilitation Engineering*, 19(6):601–611, 2011.

A. Simpkins. System identification: Theory for the user, 2nd edition (ljung, l.; 1999) [on the shelf]. *IEEE Robotics Automation Magazine*, 19(2):95–96, 2012.

T. Sinkjaer and D. Popovic. Peripheral nerve stimulation in neurological rehabilitation. In *First International IEEE EMBS Conference on Neural Engineering, 2003. Conference Proceedings.*, pages 474–476, 2003.

V. Sirtori, D. Corbetta, L. Moja, and et.al. Constraint-induced movement therapy for upper extremities in patients with stroke. *Stroke*, 41(1):e57–e58, 2010.

M. Sivan, J. Gallagher, R. Holt, A. Weightman, M. Levesley, and B. B. and. Investigating the international classification of functioning, disability, and health (icf) framework to capture user needs in the concept stage of rehabilitation technology development. *Assistive Technology*, 26(3):164–173, 2014.

SMARTmove project. Stroke statistics. Available at `www.smartmove.soton.ac.uk/`, 2020.

G. Snoek, M. IJzerman, F. Groen, and et.al. Use of the ness handmaster to restore hand function in tetraplegia. *Spinal cord*, 38(4):244–249, 2000.

A. Soska, C. Freeman, and E. Rogers. Ilc for fes-based stroke rehabilitation of hand and wrist. In *2012 IEEE International Symposium on Intelligent Control*, pages 1267–1272, 2012.

A. Soska, C. T. Freeman, T. Exell, and et.al. Surface electrode array based control of the wrist and hand. *IFAC Proceedings Volumes*, 46(11):164–169, 2013.

State of Nation. Stroke statistics. Available at https://www.stroke.org.uk/what-is-stroke/stroke-statistics, 2020.

J. W. Sturm, H. M. Dewey, G. A. Donnan, and et.al. Handicap after stroke: How does it relate to disability, perception of recovery, and stroke subtype? *Stroke*, 33(3):762–768, 2002.

J. E. Sullivan, J. Drogos, C. Carmona, and et.al. The post-stroke upper limb improvement effort survey (impetus): a survey of individuals with chronic stroke. *Topics in Stroke Rehabilitation*, 26(8):608–620, 2019.

Z. Sun, T. Qiu, A. Iyer, B. E. Dicianno, and N. Sharma. Continuous switching control of an input-delayed antagonistic muscle pair during functional electrical stimulation. *IEEE Transactions on Control Systems Technology*, 31(1):306–316, 2023.

H. G. Tan, C. Y. Shee, K. H. Kong, C. Guan, and W. T. Ang. Eeg controlled neuromuscular electrical stimulation of the upper limb for stroke patients. *Frontiers of Mechanical Engineering*, 6(1):71–81, 2011.

R. W. Teasell, N. C. Foley, S. K. Bhogal, and et.al. An evidence-based review of stroke rehabilitation. *Topics in stroke Rehabilitation*, 10(1):29–58, 2003.

E. Theodorou, E. Todorov, and F. J. Valero-Cuevas. Neuromuscular stochastic optimal control of a tendon driven index finger model. In *Proceedings of the 2011 American Control Conference*, pages 348–355, 2011.

R. Triolo, R. Nathan, Y. Handa, and et.al. Challenges to clinical deployment of upper limb neuroprostheses. *Journal of rehabilitation research and development*, 33(2):111–122, 1996.

R. Turk, S. V. Notley, R. M. Pickering, D. M. Simpson, P. A. Wright, and J. H. Burridge. Reliability and sensitivity of a wrist rig to measure motor control and spasticity in post-stroke hemiplegia. *Neurorehabilitation and Neural Repair*, 22(6):684–696, 2008.

M. Uchiyama. Formation of high-speed motion pattern of a mechanical arm by trial. *Transactions of the Society of Instrument and Control Engineers*, 14(6):706–712, 1978.

F. J. Valero-Cuevas, J.-W. Yi, D. Brown, R. V. McNamara, C. Paul, and H. Lipson. The tendon network of the fingers performs anatomical computation at a macroscopic scale. *IEEE Transactions on Biomedical Engineering*, 54(6):1161–1166, 2007.

A. L. van Ommeren, L. C. Smulders, G. B. Prange-Lasonder, J. H. Buurke, P. H. Veltink, and J. S. Rietman. Assistive technology for the upper extremities after stroke: systematic review of users' needs. *JMIR rehabilitation and assistive technologies*, 5(2):e10510, 2018.

J. M. Veerbeek, E. Wegen, R. Peppen, and et.al. What is the evidence for physical therapy poststroke? a systematic review and meta-analysis. *PLOS ONE*, 9(2):1–1, 2014.

R. Velik, N. M. Malešević, L. Popović, and et.al. Intfes: A multi-pad electrode system for selective transcutaneous electrical muscle stimulation. In *Proceedings Annual Conference of the International FES Society (IFESS)*, 2011.

H. Wang, Z. Bi, Y. Zhou, F. Li, K. Wang, X.-Y. Lu, and Z.-G. Wang. Wearable and wireless distributed multi-site fes prototype for selective stimulation and fatigue reduction: a case study. *Radioengineering*, 30(227), 2021.

Z. Wang, C. P. Pannier, K. Barton, and D. J. Hoelzle. Application of robust monotonically convergent spatial iterative learning control to microscale additive manufacturing. *Mechatronics*, 56:157–165, 2018.

T. Ward, N. Grabham, C. T. Freeman, and et.al. Multichannel biphasic muscle stimulation system for post stroke rehabilitation. *Electronics*, 9(7):1156, 2020.

A. J. Westerveld, A. C. Schouten, P. H. Veltink, and H. van der Kooij. Passive reach and grasp with functional electrical stimulation and robotic arm support. In *2014 36th Annual International Conference of the IEEE Engineering in Medicine and Biology Society*, pages 3085–3089, 2014.

S. S. Wiarta, A. Arifin, S. H. Baki, F. Arrofiqi, M. H. Fatoni, and T. Watanabe. Design of post-stroke upper limb rehabilitation game using functional electrical stimulation for hemiplegic patient. In *2020 International Conference on Computer Engineering, Network, and Intelligent Multimedia (CENIM)*, pages 6–11, 2020.

J. C. Willems. Deterministic least squares filtering. *Journal of Econometrics*, 118(1-2): 341–373, 2004.

D. N. Wolf and E. M. Schearer. Holding static arm configurations with functional electrical stimulation: A case study. *IEEE Transactions on Neural Systems and Rehabilitation Engineering*, 26(10):2044–2052, 2018.

D. N. Wolf and E. M. Schearer. Simple quasi-static control of functional electrical stimulation-driven reaching motions. In *2019 9th International IEEE/EMBS Conference on Neural Engineering (NER)*, pages 211–214, 2019.

D. N. Wolf and E. M. Schearer. Trajectory optimization and model predictive control for functional electrical stimulation-controlled reaching. *IEEE Robotics and Automation Letters*, 7(2):3093–3098, 2022.

D. N. Wolf, Z. A. Hall, and E. M. Schearer. Model learning for control of a paralyzed human arm with functional electrical stimulation. In *2020 IEEE International Conference on Robotics and Automation (ICRA)*, pages 10148–10154, 2020.

Q. Wu, X. Wang, F. Du, and et.al. Modeling and position control of a therapeutic exoskeleton targeting upper extremity rehabilitation. *Proceedings of the Institution of Mechanical Engineers, Part C: Journal of Mechanical Engineering Science*, 231(23):4360–4373, 2017.

R.-B. Wu, B. Chu, D. H. Owens, and H. Rabitz. Data-driven gradient algorithm for high-precision quantum control. *Physical Review A*, 97(4):042122, 2018.

T. B. Wyller, U. Sveen, K. M. Sødring, and et.al. Subjective well-being one year after stroke. *Clinical Rehabilitation*, 11(2):139–145, 1997.

J. Xu and J.-X. Xu. Iterative learning control for output-constrained systems with both parametric and nonparametric uncertainties. *Automatica*, 49(8):2508–2516, 2013.

G. Zames and A. K. El-sakkary. Unstable systems and feedback: The gap metric. In *Proceeding of the Allerton Conference*, pages 380–385, 1980.

S. R. Zeiler and J. W. Krakauer. The interaction between training and plasticity in the poststroke brain. *Current opinion in neurology*, 26(6):609–616, 2013.

F. Zhang, D. Meng, and K. Cai. Safe iterative learning for attitude tracking of rigid bodies under nonconvex constraints. *IEEE Transactions on Automation Science and Engineering*, pages 1–13, 2023.

Z. Zhang, B. Chu, Y. Liu, and et.al. Fes based wrist tremor suppression using multi-periodic repetitive control. *IFAC-PapersOnLine*, 53(2):10135–10140, 2020.

J. Zhou, C. T. Freeman, and W. Holderbaum. Multiple-model iterative learning control with application to stroke rehabilitation. *Control Engineering Practice*, 154:106134, 2025.

Q. Zhu, J. Xu, D. Huang, and et.al. Iterative learning control design for linear discrete-time systems with multiple high-order internal models. *Automatica*, 62:65–76, 2015.